

Statistical Physics in Modeling Chromosome Movements During Nuclear Oscillation of Fission Yeast



Wenwen Huang

Max Planck Institute for the Physics of Complex Systems

This dissertation is submitted for the degree of
Doctor of Philosophy

February 2017

I would like to dedicate this thesis to my loving parents ...

Declaration

I hereby declare that except where specific reference is made to the work of others, the contents of this dissertation are original and have not been submitted in whole or in part for consideration for any other degree or qualification in this, or any other university. This dissertation is my own work and contains nothing which is the outcome of work done in collaboration with others, except as specified in the text and Acknowledgements. This dissertation contains fewer than 65,000 words including appendices, bibliography, footnotes, tables and equations and has fewer than 150 figures.

Wenwen Huang
February 2017

Acknowledgements

And I would like to acknowledge ...

Abstract

This is where you write your abstract ...

Table of contents

List of figures	xv
List of tables	xix
1 Introduction	1
1.1 Nuclear oscillation in fission yeast	1
1.1.1 Fission yeast	2
1.1.2 Basis of meiosis	3
1.1.3 Nuclear oscillation	5
1.1.4 The role of nuclear oscillation	6
1.2 Chromosomes modeled as the polymer	7
1.2.1 The ring polymer model	7
1.2.2 Pulled polymer model	10
1.3 Outline	11
1.3.1 Research goals	12
1.3.2 Overview of the thesis	12
2 Model and Simulation Methods	13
2.1 Pulled polymer loop model	13
2.1.1 Coordinate transformation	14
2.1.2 Bead-rod model	15
2.1.3 Bead-spring model	18
2.2 Brownian Dynamics simulation method	20
2.2.1 BD simulation of the bead-rod model	20
2.2.2 BD simulation of the bead-spring model	24
2.3 Monte-Carlo simulation of the bead-rod model	25
2.4 Summary	27

3 Equilibrium Statistics Applied to Chromosome Alignment	29
3.1 Pinned polymer loop in a constant force field	29
3.2 Pinned Polymer Loop in 1D	31
3.2.1 Mapping to particles on 1D lattice	32
3.2.2 The grand canonical ensemble solution	34
3.2.3 Canonical ensemble solution	38
3.3 Equilibrium statistics in 3D	42
3.3.1 Partition function	43
3.3.2 Mean and variance of the bead position	43
3.4 Modeling the chromosome alignment	46
3.4.1 Chromosome paring and alignment	46
3.4.2 Theory fits to the biology	47
3.4.3 Two intersecting Loops	49
3.5 Summary	50
4 Dynamical Properties of Pulled Polymer Loops	53
4.1 Rouse theory of the pinned bead-spring loop	54
4.1.1 Dynamical equations	54
4.1.2 The normal modes	55
4.1.3 Relaxation time	58
4.1.4 Compare to the bead-rod model	58
4.2 1D Pinned Bead-rod Loop Maps to ASEP	60
4.2.1 The mapping to ASEP	60
4.2.2 Brief introduction of ASEP	63
4.2.3 Numerical results of the dynamics	64
4.3 The Bethe-ansatz Solution of ASEP	67
4.3.1 Solution of single particle	68
4.3.2 Solution of two particles	71
4.3.3 Solution of General N particles	78
4.3.4 Relaxation time	83
4.4 Dynamics of 3D bead-rod polymer loop	84
4.4.1 Relaxation time of 3D pinned Bead-rod Loop	85
4.4.2 Comparison to the blob theory	86
4.5 Summary	86

5 Characterize the Nuclear Oscillation	87
5.1 Oscillation of the Pinned Polymer Loop	87
5.1.1 The Rouse Theory	87
5.1.2 Simulation Results	87
5.2 Characterize the Shape of Chromosomes	87
5.2.1 The Gyration Tensor	87
5.2.2 Asphericity and the Nature of Asphericity	87
5.3 Extract Shape Information From Experimental Data	87
5.3.1 Shape from Experimental Data	87
5.3.2 Compare to Theory and Simulation Results	87
5.4 Summary	87
6 Conclusions and Outlook	89
6.1 Conclusions	89
6.2 Outlook	89
Appendix A An efficient algorithm to compute <i>pseudo</i> force of bead-rod loop	91
Appendix B Monte-Carlo simulation of 1D particle-lattice model	93
Appendix C The Bethe-ansatz Solution of Periodic ASEP	95
Appendix D The Toeplitz Matrix	97
Appendix E Derivation of the Exclusion Condition	99
Appendix F Single-file Diffusion with Reflecting Boundaries	101
References	103

List of figures

1.1	Microscopic view of a fission yeast culture. The scalar bar indicates 10 μm . Image reprinted from [1] with permission.	2
1.2	Overview of meiosis and an illustration of recombination between homologous chromosomes resulting in four unique daughter cells. Image reprinted from [] with permission.	3
1.3	The meiotic prophase I of fission yeast. Telomeres are clustered to form a bouquet structure. Image modified and reprinted from [2].	4
1.4	Time-lapse experiments of nuclear oscillation in fission yeast, DNA marker in green (Rec8-GFP) and SPB marker in magenta (Sid4-mCherry) also indicated by asterisk. Reprinted from [3] with permission.	5
1.5	The sketch of our pulled polymer loops model for chromosomes in meiotic fission yeast. Three pairs of chromosomes with all ends bound to SPB (shown in magenta) in the nucleus are indicated by different colors. The SPB is pulled by multiple dynein motors (not shown) walking along microtubules (dark green). The SPB is anchored to the nuclear envelope (light green) and entrains the whole nucleus.	7
1.6	Illustration of “stem-flower” picture for pulled polymer chain. (a) Trumpet picture at moderate pulling force; (b) Stem-flower picture at strong pulling force. Image reprinted from [4].	11
2.1	Illustration of coordinate transformation. (a) a pulled polymer loop before transformation; (b) pinned polymer loop in an external field after transformation.	14
2.2	Sketch of the bead-rod loop model. The magenta bead represents the SPB and other cyan beads represent the chromosome segments.	15
2.3	The distribution of included angle of a bead-rod trimer. (a) without <i>pseudo</i> force; (b) with <i>pseudo</i> force. The blue bins are from Brownian Dynamics simulation results. Inset of (a) is a sketch for the trimer.	17

2.4	Sketch of the bead-spring loop model. The magenta bead represents the SPB and other cyan beads represent the chromosome segments.	19
2.5	Illustration of the Monte-Carlo configuration flip.	26
3.1	Experimental trajectory and velocity of the SPB measured by florescence microscopy. The upper panel shows the trajectory of the SPB along the cell main axis. Green line is the boundary of the cell. The lower panel shows the corresponding velocity of the SPB. Image reprinted and modified from [5].	30
3.2	Sketch for the pinned bead-rod loop and notations.	31
3.3	Illustration for the mapping from 1D pinned polymer loop to Fermionic particles on 1D lattice sites.	32
3.4	Fermi-Dirac distribution compared with the exact solution from the number partition theory. Solid lines are the exact solution while the dots are Fermi-Dirac approximations. Different dimensionless temperature is indicated by different colors as shown in the legend. (a) $L = 10$, (b) $L = 100$	35
3.5	Mean and variance of the 1D pinned polymer bead positions. MC simulation results (dots) are compared with theoretical results (solid lines) Eq. 3.15. The length of the polymer loop $L = 10$. The black dash line indicates the case $\tilde{T} \rightarrow \infty$, i.e. no external force field.	36
3.6	Mean and variance of the 1D pinned polymer bead positions. MC simulation results (dots) are compared with theoretical results (solid lines) Eq. 3.18. The length of the polymer loop $L = 10$. The black dash line indicates the case $\tilde{T} \rightarrow \infty$, i.e. no external force field.	37
3.7	Some examples of the Young diagram.	39
3.8	Mean and variance of the bead position in the direction along the force field. Solid lines are theory and dots are Monte-Carlo simulation results. The black dash line indicates the case $\tilde{T} \rightarrow \infty$, i.e. no external force field.	44
3.9	Comparison of fluctuations in x , y and z directions. Symbols denote the Monte-Carlo simulations. Circles show the fluctuations along the z axis, whereas stars and triangles along x and y axis respectively. Colors correspond to different dimensionless temperatures. Solid and dashed lines are theoretical predictions for fluctuations along and orthogonal to the force field, respectively.	45
3.10	A Pair of homologous chromosomes bound to the SPB. The distance of a pair of loci is illustrated as \mathbf{d}_i	46

3.11 The distance between corresponding loci of homologous pair varies with the dimensionless temperature. Different curve indicates different location along the chromosome. The shaded region denotes the separation below which the chromosomes are considered to be paired. Dots are BD simulation data and solid lines are results from our theory. Inset is an sketch of the observing loci along the chromosome. Parameters are shown in the context.	47
3.12 The sketch of two intersecting loops 1 and $1'$ which are connected at one additional bead with index c . Shaded regions indicate the redefined loops A and B. The distance \mathbf{d} between two homologous beads h and $2c - h$ is illustrated.	49
3.13 Variance of the distance between homologous beads with additional constraint. The constraint is located at the bead with index $c = 100$. Circles denote the simulation results while the solid lines represent the theory. The dashed lines show the variance of the unconstrained case with different color indicates different dimensionless temperature. The black dashed line shows the limit of unconstrained force-free Brownian bridge.	51
4.1 The sketch of pinned bead-spring loop with notations.	54
4.2 The equilibrium mean and variance of bead position for the bead-spring model, compared with the bead-rod model. (a) Mean bead position of z component. (b) The variance of bead position. Dots are BD simulation results, solid lines are the Rouse theory for the bead-spring polymer loop, dash lines are the theory of the bead-rod model. Different color denotes different dimensionless temperature \tilde{T} which is indicated in the legend. The black dash line in both (a) and (b) shows the force free limit.	58
4.3 The schematic of ASEP and the mapping of dynamics. (a) Illustration of ASEP, orange beads represent particle and reflecting boundary is indicated. (b) Illustration of one step particle hopping process maps to the flipping of two neighboring rods in the polymer picture.	60
4.4 Schematics of ASEP model. (a) ASEP with periodic condition. (b) ASEP with open boundary condition.	63
4.5 The relaxation time of 1D reflecting ASEP system obtained from the Kinetic Monte Carlo simulation. Total number of lattice site is $L = 100$, different makers denote different total number of particles on the lattice. See more explanation in the main context.	65

4.6	Eigenvalues of a small 1D reflecting ASEP system with different number of particles on the lattice. $L = 10$ and the number of particle $N \in \{1, 2, \dots, 9\}$. (a) All eigenvalues, the eigenvalue is marked by bars. (b) Zoom in view for the shaded regime in (a), eigenvalues is marked by asters, the back line denotes the zero line and the red line shows that the largest non-zero eigenvalues are all the same. Parameters are set as $\alpha = 1, \beta = 2$	66
4.7	The interpretation for the Bethe Equations of the reflecting ASEP as if it is a periodic ASEP system.	77
4.8	The left panel: the embedding structure of eigenvalues illustrated by a system of $L = 10$ with one, two and three particles. $\alpha = 2, \beta = 1$. The right panel: eigenvalue obtained from brute force digitalization of Markovian matrix and from the Bethe equations. $\alpha = 2, \beta = 1, L = 10, N = 2$	82
4.9	Relaxation time of 1D model varies with the dimensionless temperature $\tilde{T} := k_B T / \Delta E$. The y axis is normalized with the Rouse relaxation time. The ACF curves for several typical cases are shown in the inset. The corresponding relaxation time is fitted and show with dashed black lines, which are also marked with the same color in the simulation dots.	83

List of tables

1.1 Parameters of fission yeast during meiosis	6
--	---

Chapter 1

Introduction

Many biological processes can be transferred to well-studied models in statistical physics. Examples are ranging from the random walk model of mRNA during the transcription [6–8] to the evolution of ecological systems [9–12]. Analysis of these extracted models could help us to get useful insights into the corresponding biological problems. In this thesis, we are interested in modeling a molecular level biological problem, i.e. the motion of chromosomes in fission yeast during meiotic cell division [13, 5, 14].

Interestingly, during Prophase I of meiotic fission yeast, the nucleus containing three pairs of chromosomes move from one pole of the rod-like cell to the other, forming an oscillation behavior last for about two hours. The period of the oscillation is about 10 minutes. Cells are divided into two after the oscillation is done [15–17].

We are going to model this oscillation processes quantitatively with the chromosomes represented by polymer models [18, 19]. The results we obtained from the modeling are used to explain relevant biological functionalities like chromosome alignment and gene recombinations [20].

In this chapter, we will introduce the biological backgrounds and some previous related studies about modeling chromosomes with polymers. We will propose our research goals and give an overview of the thesis in the last section.

1.1 Nuclear oscillation in fission yeast

In this section, we will introduce the biological basis of nuclear oscillation in fission yeast. We will firstly introduce our model organism, fission yeast. And then we show some basis of meiosis cell division. Next, we go into the nuclear structure of fission yeast and the movements of chromosomes, specifically during meiosis. The biological processes like

chromosome alignment and recombination are discussed. In the last subsection, we discuss some understandings for the biological role of the nuclear oscillation.

1.1.1 Fission yeast

Fission yeast, also named *Schizosaccharomyces pombe*, is a model organism that widely used in the study of molecular and cell biology. It is a unicellular eukaryote and has a rod-like shape. Typical size of fission yeast is 3-4 micrometres in diameter and 7-14 micrometres in length [21, 22]. See in Fig. 1.1 for a illustration of fission yeast.

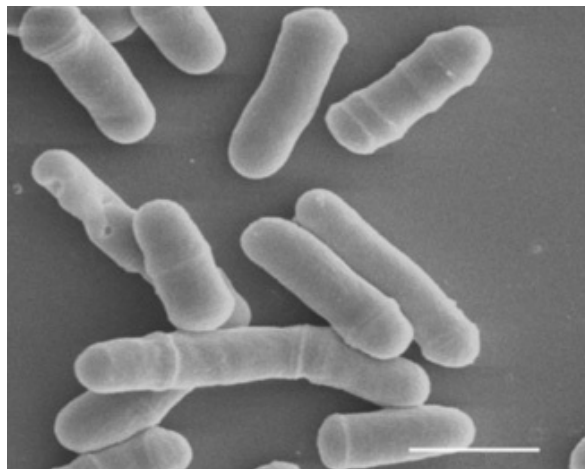


Fig. 1.1 Microscopic view of a fission yeast culture. The scalar bar indicates $10 \mu\text{m}$. Image reprinted from [1] with permission.

Fission Yeast is widely used in traditional brewing and baking. It was first discovered in 1893 in the sediment of millet beer [22, 23]. As a single-celled fungus, fission yeast has a simple genome with three different chromosomes. The genome of fission yeast is fully sequenced and the three chromosomes contain about 14Mb of DNA [24]. It has a rapid growth rate and easily manipulated to make mutants, which make it a perfect modeling organism for genetic studies. The growth of the fission yeast is simply by the elongation at the ends. After mitosis, division occurs by the formation a cell plate that cleaves the cell at its midpoint [21].

Fission yeast is normally a haploid cell. However, when put under stressful conditions, such as nitrogen deficiency, two cells will conjugate to form a diploid and then form four spores via meiosis [25]. This is easy to observe experimentally and this stage is exactly when the interesting nuclear oscillation happens [13]. In the next subsection, we will explain the basis of the meiosis in fission yeast.

1.1.2 Basis of meiosis

Meiosis is a kind of cell division that reduces the number of chromosomes in the parent cell by half and produces four genetically distinct gamete cells. This process occurs in all the sexually reproducing organisms, including human [26].

Meiosis begins with a parent cell with two copies of each chromosome, and is followed by two rounds of cell divisions which produce four potential daughter cells, each has half number of chromosomes as their parent cell. The two rounds of cell division are called *Meiosis I* and *Meiosis II*, respectively. It is during Meiosis I that the pair of chromosomes, one from the father and the other from the mother, separates into two offspring cells. Meiosis II is very similar to the mitosis where two sister chromatins separate [26, 27]. See an overview of meiosis in Fig. 1.2.

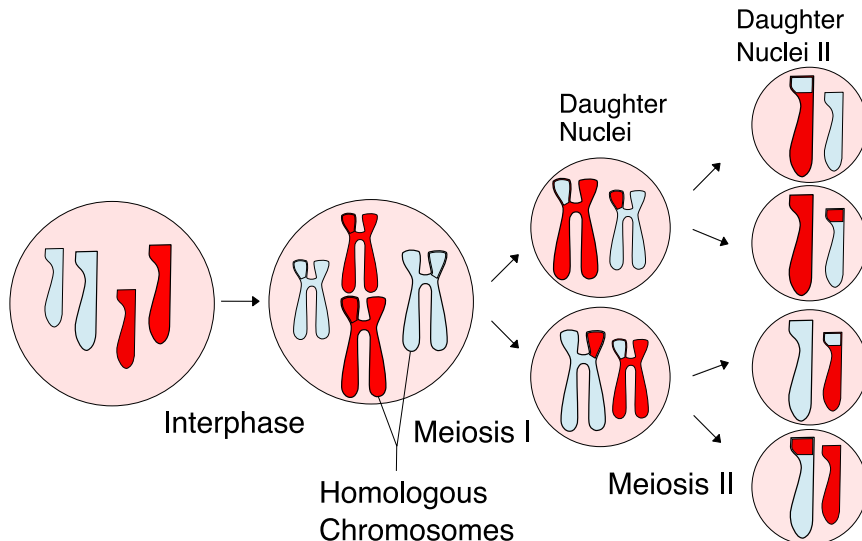


Fig. 1.2 Overview of meiosis and an illustration of recombination between homologous chromosomes resulting in four unique daughter cells. Image reprinted from [] with permission.

As in mitosis, each round of cell division can be divided in prophase, metaphase, anaphase, and telophase. We will elaborate Meiosis I in details, especially the Prophase I when the nuclear oscillation happens.

- *Prophase I*: prophase I is an important stage that many processes happened. Two of the examples are bouquet formation [28] and homologous recombination [29, 17], both occurring in generic organisms. In the early state of Prophase, chromosomes are reorganized spatially, usually, the telomeres are clustered and attached to a small region of the nuclear membrane, forming a bouquet structure. This is called bouquet formation or telomere clustering in biology [13, 28, 30], see in Fig 1.3 for an example in fission yeast. In the process of recombination, the homologous chromosomes, which are paternal and maternal

pairs, align and exchange some parts of their DNA and usually results in the chromosomal crossover. Homologous recombination is critical for pairing and accurate segregation of the chromosomes in the later stage of Meiosis I. More interestingly, this stage is exact the period when the nuclear oscillation happens in fission yeast [31, 32]. We will devote this part to next subsection.

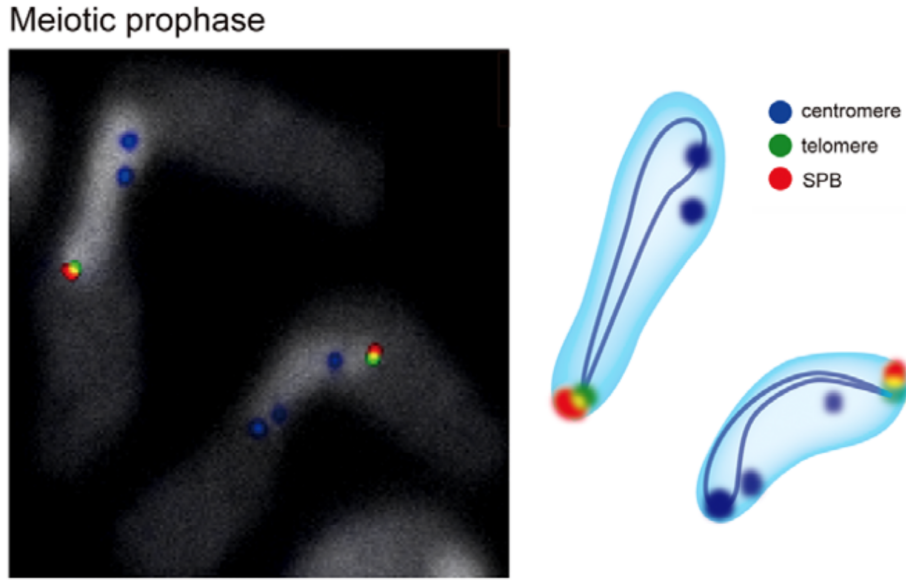


Fig. 1.3 The meiotic prophase I of fission yeast. Telomeres are clustered to form a bouquet structure. Image modified and reprinted from [2].

- *Metaphase I*: in this stage, homologous pairs move together along the middle plate, the microtubules from centrosomes attach to their respective chromosomes, the paired homologous chromosomes align along an equatorial plane that bisects the spindle. However, in Fission Yeast, the centromere is replaced by a functional equivalent organelle called spindle pole body (SPB) [26].
- *Anaphase I*: in this stage, the microtubules shorten, pulling homologous chromosomes to opposite poles. Notice here, chromosomes still consist of a pair of sister chromatids. The cell body elongates, preparing for cell division [26].
- *Telophase I*: in the last stage of Meiosis I, chromosomes arrive at the poles. The microtubules network of spindle disappears. New nuclear membrane appears. The two daughter cells now only have half the number of chromosomes [26].

After Meiosis I, Meiosis II occurs without DNA replication in between. The process is similar to Meiosis I except the sister chromatids segregate instead of homologous chromosomes [26]. Four unique daughter cells are formed after the completion of Meiosis. The homologous recombination process takes an important role for this uniqueness.

1.1.3 Nuclear oscillation

As mentioned in the previous subsection, nuclear oscillation happens during prophase I of meiosis in fission yeast, and so as the important processes of chromosomes homologous alignment and recombination [31]. Because the impressive shape of nucleus during this stage, nuclear oscillation also often mentioned as *horse-tail* movements in biology[33, 32, 29], see in Fig. 1.4 for a time-lapse illustration. We believe the chromosome movements play an important role in this process and decide to model it quantitatively. In this subsection, we are going to elaborate the details of nuclear oscillation. We will answer the questions like what is the internal structure of nucleus during oscillation, what is the driven force of the oscillation, how long the oscillation lasts and what is the time period of the oscillation, etc.

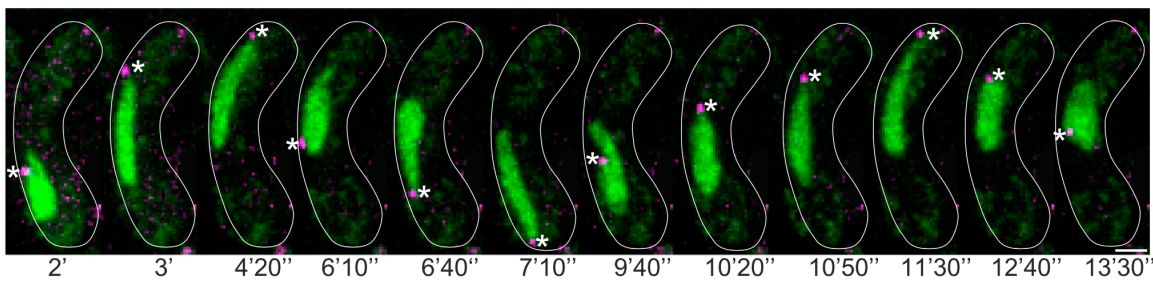


Fig. 1.4 Time-lapse experiments of nuclear oscillation in fission yeast, DNA marker in green (Rec8-GFP) and SPB marker in magenta (Sid4-mCherry) also indicated by asterisk. Reprinted from [3] with permission.

The looping structure of chromosomes

Before the nuclear oscillation, chromosomes are reorganized and the bouquet formation happens. In fission yeast, the SPB is anchored in the nuclear envelope, telomeres of chromosomes are clustered to the SPB region of the inner nuclear membrane. The chromosomes are condensed to be the rod-like chain. Notice that there are still two sister chromatins contained in one chromosome. With all the telomeres bond to the SPB, chromosomes form the looping structure, as we can see in Fig. 1.3.

Redistribution of dynein motors drives the nuclear oscillation

While the inner side of SPB bonds the chromosome telomeres, the outer side is attached to the microtubules in the cytoplasm. During the oscillation, dynein motors are the energy supplier. Interestingly, as one motor is not enough for the oscillation, the collective behavior of motors is observed to drive the nucleus motion. The spatial distribution of motor molecular

varies during the oscillation. Motors accumulates in the side of fission yeast that the nucleus moves toward to. It is found that the pulling force is the main contribution that drives the oscillation [5].

Related biological parameters of nuclear oscillation

To study the dynamics during oscillation, several parameters are estimated experimentally and input into our model later. These parameters are summarized in table 1.1.

Table 1.1 Parameters of fission yeast during meiosis

Parameter	Value
Typical size of nucleus	$3\mu\text{m}$
Chromosome number	Three pairs
Compaction ratio of chromatin	10^2bp/nm
Kuhn length of chromatin	$100 \sim 300\text{nm}$
Duration of nuclear oscillation	2 hours
Period of nuclear oscillation	10 min
Moving speed of nucleus	$2.5\mu\text{m/min}$
Viscosity of nucleoplasm	$1000 \times \mu_{\text{water}}$
Length of Chromosome I	5.58 Mb
Length of Chromosome II	4.54 Mb
Length of Chromosome III	2.45 Mb

1.1.4 The role of nuclear oscillation

Although we can clearly observe the nuclear oscillation in fission yeast, the biological role of it is not thoroughly understood. One intuitive hypothesize is that the movement facilitates the paring of homologous [16]. However, Koszul et al. proposed that the chromosome movement might play other roles than paring, such as resolve homologous entanglements or non-homologous connections [33]. Also, Mariola et al. stated a dual role for the nuclear oscillation, promoting initial paring and restricting the time of chromosome associations to ensure proper segregation [3].

We believe nuclear oscillation plays an important role for the chromosome alignment. However, it is hard to image the exact mechanism of the alignment without going deeper of the process. That is why we propose a quantitative model in this thesis and study the statistical and dynamical details of the model, trying to understand to the machinery of paring quantitatively.

1.2 Chromosomes modeled as the polymer

To quantitatively describe the chromosome, it is natural to model it as a polymer. In fact, there are already a lot of excellent examples in this direction [34–37]. However, depending on the situations under considering, different polymer models may applied.

In physics, a polymer model is usually described by beads connected by massless springs or rods. The interactions, usually characterized as different types of potentials, specify the setting of the model [19]. As we want to model the chromosome during nuclear oscillation in fission yeast, there are two major factors we need to take into account besides some other minor details. First, the topology of the chromosome is a ring structure as shown in Fig 1.3. Second, all chromosomes are bound to the SPB and pulled by an external force. According to these biological factors and the experimental measurements like Fig. 1.3, we propose a pulled polymer loop model for the chromosomes in this specific situation. See in Fig. 1.5 for a sketch of our model. We will leave the discussion of the model details in afterward chapters.

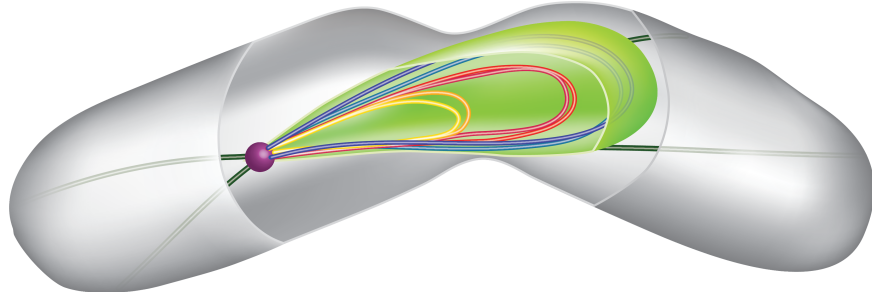


Fig. 1.5 The sketch of our pulled polymer loops model for chromosomes in meiotic fission yeast. Three pairs of chromosomes with all ends bound to SPB (shown in magenta) in the nucleus are indicated by different colors. The SPB is pulled by multiple dynein motors (not shown) walking along microtubules (dark green). The SPB is anchored to the nuclear envelope (light green) and entrains the whole nucleus.

To the best of our knowledge, there are not many works which are discussing on not only the polymer loops but also the polymer is pulled by an external force. In the following subsections, we will introduce two related aspects of previous works, i.e. works about the polymer loops and works related to pulled polymer.

1.2.1 The ring polymer model

Polymers forming a ring structure are ubiquitous in chemistry and biology [36, 38]. The study of ring polymer can go back to the years when polymer physics was built up [39, 40].

Kramers developed an equilibrium theory that possesses branch points and rings of the dilute polymer solution in 1946 [39]. Zimm calculated the statistics of mean square radii of molecules containing branches and rings in 1949 [40]. However, comparing to the simplest polymer chain model, research focus on polymer ring are far less than the former. We will review here some interesting and most related ones. Of course, it is not possible to exhaust all related works here, we pay our attention particularly to those that are related to the chromosome modeling.

Since Kramers and Zimm, there are a number of works trying to study the static and dynamical properties of the ring polymer from the theoretical point of view. In 1965, Casassa derived some statistical properties of flexible ring polymers, including mean square radius, the second Virial coefficient and angular distribution of scattering [41]. 1980, Burchard and Schmidt calculated the static and dynamical structure factors of flexible ring polymers [42]. Baumgärtner considered the self-avoiding effect of ring polymers in 1984 and found the asymptotic scaling exponents are the same as linear polymers [43]. In 1986, Cates et al. studied the nor-concatenated ring polymer melt and found the size of polymer R scales with the polymerization index N as $R \sim N^{2/5}$ and the diffusion constant D scales as $D \sim N^{-2}$ [44]. In 1994, Obukhov et al. considered the dynamics of a ring polymer in a gel and obtained the diffusion coefficient scales with the molecular weight as $D \sim M^{-2}$ and the longest relaxation time T scales as $T \sim M^{5/2}$ [45]. Carl investigated the configurational and rheological properties of multiple-twisted ring polymers using a long cyclic finitely extensible bead-spring model in 1995 [46]. He also presented a study on bead-spring chains in steady flows, various properties such like the power spectrum, the autocorrelation functions of configurational quantities were discussed in 1996 [47]. In 2001, Panyukov and Rabin studied the effects of thermal fluctuations on elastic rings. Analytical expressions are derived for some static and dynamical quantities [48]. Mukherji et al. studied a polymer ring or chain diffused around attractive surfaces. They found the diffusion constant scales as $D \sim N^{-3/2}$ linear chain and solid strong adsorbed surfaces, and $D \sim N^{-1}$ for ring polymer and soft surfaces in 2008 [49]. Sakaue proposed a simple mean-field theory for the structure of ring polymer melts which takes into account the many-body effects [50, 51]. In 2012, Kim et al. presented a self-consistent field theory formalism of topologically unconstrained ring polymers [52]. In 2013, Reigh performed lattice Monte-Carlo simulations to investigate the dependence of ring polymer conformation to the concentration, where the scaling of gyration radius with the concentration $R_g \sim \phi^{-0.59}$ was found [53]. In 2014, Lang et al. studied the tumbling dynamics of semiflexible ring polymers as a model of the cytoskeletal filament in a shear flow. They found the tumbling frequency scales f_c scales with the Weissenberg number as $f_c \sim Wi^{3/4}$ rather than the prediction of classical theory that $f_c \sim Wi^{2/3}$ [54].

Ring polymer with high concentration, like polymer melts, are often used in modeling interphase chromosomes. Interestingly, it is found that during interphase, the spatial organization for the multiple chromosomes in the nucleus is not homogeneous and well mixed. Instead, each chromosome forms its own “territories” [36]. Many interesting works can be found respecting to this problem. For example, in 2008, Rosa and Everaers used the simulation results of polymers to explain the existence and stability of territories of interphase chromosomes in genetic eukaryotes [55]. Because usually, the computation power required to simulate the whole genome is huge, they also developed an efficient multiscale numerical approach to study the conformational statistics of ring polymers melts in [56]. Dorier employed a very simple non-permeable freely jointed polymer model and recovered the chromosomal territories in a crowded nuclei [57]. This part of work is well reviewed in [36], the interested reader can refer to the references therein.

On the other hand, it is also possible that ring polymer structures are formed temporarily in chromosomes. This could be caused by the DNA replication process or binding proteins connecting two loci of chromosomes. Many great works were done also in this direction. In 1995, Sachs use a looping random walk model to study to the interphase chromosomes, fluorescence labeled data is compared to the theoretical prediction [58]. Marko considered a model of two polymer rings tethered one another and its application to chromosome segregation in 2009 [59]. The looping probabilities of interphase chromosomes were also discussed in [60]. In 2011, Zhang et al. modeled the meiotic chromosomes as a polymer that could form internal loops by binding proteins. They found the loops play an important role in the mechanical properties of the polymer [61]. Wong set up a polymer model and use it to predict the whole nuclear architecture of fission yeast [62]. Dekker and Giorgetti employed the computational polymer model to explain the 3C/HiC data [63, 64]. In 2014, Youngren employed ring polymer model to study the duplication and segregation of *E. coli* chromosomes [65]. These are just a few examples, more can be found if one is interested.

The confinement such as the nuclear membrane or cell shape could also take an important role in chromosome dynamics. One of the examples of this kind of work is Fritsche’s work in 2011, they studied the influence of confinement geometry to the spatial organization of semiflexible ring polymers [66]. The studies of the polymers (including chains and rings) under confinements were reviewed by Ha el al. in [67].

There are also a lot of great experimental work related to ring polymers. In 1992, Tead et al. employed polystyrene molecules to perform experiments and compared the diffusion of linear and ring polymers [68]. Kapnistos et al. found the stress relaxation of entangled ring polymer was power-law rather than exponential in [69]. Structure and dynamics of polymer rings by neutron scattering were studied by Brás et al. in 2011. Witz et al. employed the

atomic force microscopy to studied 2D circular DNA in [70, 71]. Gooßen et al. studied dynamics of polymer rings using neutron spin echo spectroscopy which space-time evolution of segmental motion could be observed [72, 73].

Due to its importance, the study of ring polymers is much intensive and causes much more attention nowadays. Besides what we have mentioned above, the shape of ring polymers is studied in [74–77]. Also, there are a series of works considering the ring polymer with entanglements and topological knots [78–86]. We are only able to list a few of those great works. Interested readers can refer to the references therein.

1.2.2 Pulled polymer model

As we mentioned above, in order to model the nuclear oscillation of fission yeast, we have to consider the pulling dynamics. If we transfer the coordinate and sit on the pulled monomer, a pulled polymer is also equivalent to a pinned polymer in an external flow or force field. In this section, we would like to review some previous works in this direction. Most of them are about pulled polymer chain. Whatsoever, we think it is still helpful to know what have been done about pulled polymers or tethered polymer in an external field.

A polymer chain with one end free and the other end pulled by an external force was first discussed by de Gennes [87, 18]. After that, another important progress was made by Pincus, he developed what is now called Pincus theory [88, 89], which consider the pulled polymer as a sequence of independent “blobs”. Brochard-Wyart further developed the “trumpet” and the “stem-flower” pictures of pulled polymer chain [90, 91, 4, 92]. When the pulling force is not too strong, the polymer presents as a series of independent blobs with increasing size, i.e. the portion of polymer near to the free end fluctuates more. As the pulling force increased to a strong regime, the polymer portion near to fixed end is totally stretched, forming a “stem-flower” like picture, see in Fig. 1.6. Using fluorescence microscope and optical tweezers, Perkins et al. performed the pulling experiments on single DNA molecule and found the results consistent with the Brochard-Wyart’s theory [93, 94]. They also measured the relaxation time of this pulled polymer and obtained the scaling $\tau \sim L^{1.66}$ [95]. Wirtz also confirmed the theory by measuring transport properties of a single DNA molecule in [96].

Rezehak et al. considered pinned polymer in a uniform flow with hydrodynamic interaction and proposed a so-called f-shell blob model [97]. Larson et al. performed Brownian Dynamics simulation for a DNA in an external flow field [98]. In 2000, Doyle measured the cyclic and stretching dynamics of a tethered DNA molecule in the shear flow [99, 100]. Sebastian studied the dynamics of pulling a polymer out of a potential well [101]. Cui performed the stretching and releasing experiment by pulling a single chicken erythrocyte

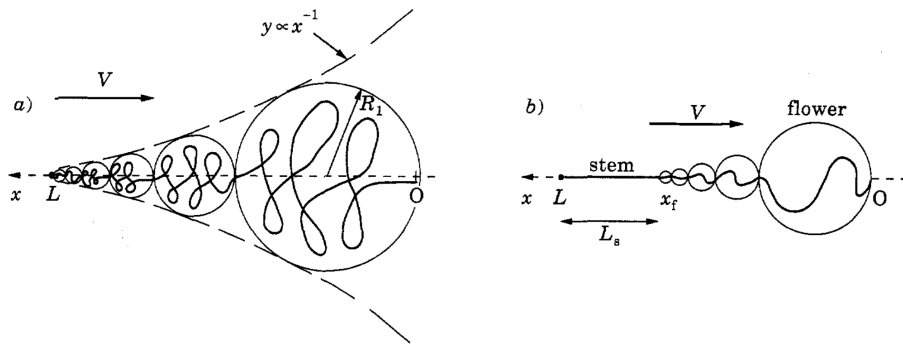


Fig. 1.6 Illustration of “stem-flower” picture for pulled polymer chain. (a) Trumpet picture at moderate pulling force; (b) Stem-flower picture at strong pulling force. Image reprinted from [4].

chromatin fiber with the optical tweezers [102]. Rzehak discussed the conformation fluctuation and relaxation of a tethered polymer in uniform flow [103]. In 2007, Mohan et al. employed Rouse theory to study the unraveling dynamics of tethered semiflexible polymer in uniform solvent flow [104]. Sing et al. studied flexible and semiflexible tethered polymers in the limit of high shear flows and consequently near-full extension of the chains in [105]. Sakaue et al. studied the conformation and dynamics of a single flexible polymer chain that is pulled by a constant force applied at its one end, finite extensibility, the excluded volume, and the hydrodynamic interactions are discussed [106]. Varghese et al. investigated the force fluctuations in stretching a tethered polymer [107]. In 2013, Dai and Doyle found in [108] that the scenario of a pulled polymer is very similar to a polymer confined in a cylinder with proper radius.

To the best of our knowledge, the discussion of pulled ring polymer is missing except our own work [20]. So we reviewed here the works about ring polymer on one side and the works of pulled polymer on the other side. Of course, the details are not shown here, interested readers can go into the references.

1.3 Outline

With the introduction of the biological problem and the background of polymer modeling in previous two sections, we are ready to go into the details of our study. There are several specific models and techniques used in this thesis, such as the ASEP model. In order not to break the logic of the thesis, we will leave the brief background introduction of those right before the using. In this section, we will propose our research goals for this thesis and give an overview for the organisation of the thesis.

1.3.1 Research goals

The research goals of this thesis is listed as following:

- Propose a polymer model to describe the chromosomes in fission yeast during nuclear oscillation. This is actually already mentioned in the previous section, i.e. the pulled polymer loop model. However, the details of the model will be discussed in the following chapters.
- Develop the quantitative theory for our pulled looping polymer model. As far as we know, there is no previous work on this issue. On the other hand, it is shown by the experimental facts that this model is the best one for our problem.
- Perform realistic numerical simulations of the nuclear oscillation of fission yeast using the polymer model. The theory is always simplified and has a lot of assumptions in order to analytically tractable. It is necessary to do a realistic simulation that can verify our theory on one hand, and comparable to the experimental data on the other hand.
- Using the physical insights to understand to biological processes such as chromosome alignment. Understand the biology is our ultimate goal. The chromosome movements during cell division are so important that many diseases are related to that, such as Down syndrome [109]. Our understanding from physical layer helps to fight with these diseases.

In one sentence, we want to quantitatively model the chromosome dynamics during the nuclear oscillation and use it to understand the biology.

1.3.2 Overview of the thesis

Add afterward.

Chapter 2

Model and Simulation Methods

To model the chromosome movements during nuclear oscillation in fission yeast, let us start from a single chromosome modeled by a single polymer loop. In this chapter, we will introduce the details of the polymer model for the chromosomes and the simulation methods that resolving the dynamics and statistics of the polymer.

2.1 Pulled polymer loop model

As mentioned in the previous chapter, there are three pairs of chromosomes in fission yeast. During nuclear oscillation, these three pairs of chromosomes bound to one point, i.e. the Spindle Pole Body (SPB). Now let us start with the simplest case and neglect the interactions between chromosomes, think about a single chromosome. It is a polymer with the ring structure, and an external force is exerted on the SPB. We have two choices to model this chromosome, i.e. the bead-rod model or the bead-spring model. We will use both models in this thesis but more discussions are focused on the bead-rod. Both models have their own benefits and shortcomings. Computationally, it is easier to manipulate the bead-spring model than the bead-rod. However, the bead-rod has the intrinsic property of finite extensible without resorting to some complex nonlinear spring potentials. This benefit we think is important because the chromosomes are highly condensed and are definitely finite extensible. In fact, we will show that the finite extensibility takes an important role for the polymer dynamics, see in the later chapters. And the simplicity of bead-rod model offers us the possibility to find analytical solutions.

In this section, we will introduce both the bead-rod and bead-spring model for modeling the chromosomes. However, before that, let us first do a coordinate transformation that makes our analysis much easier.

2.1.1 Coordinate transformation

Let us consider a single chromosome pulled at the SPB. The pulling force drives the chromosome moves with a velocity \mathbf{v} . In our model, the SPB is modeled as one monomer in the polymer loop. Other monomers representing the chromosome move together with the SPB because of the bonds. This scenario of pulled polymer loop is shown in Fig. 2.1 (a).

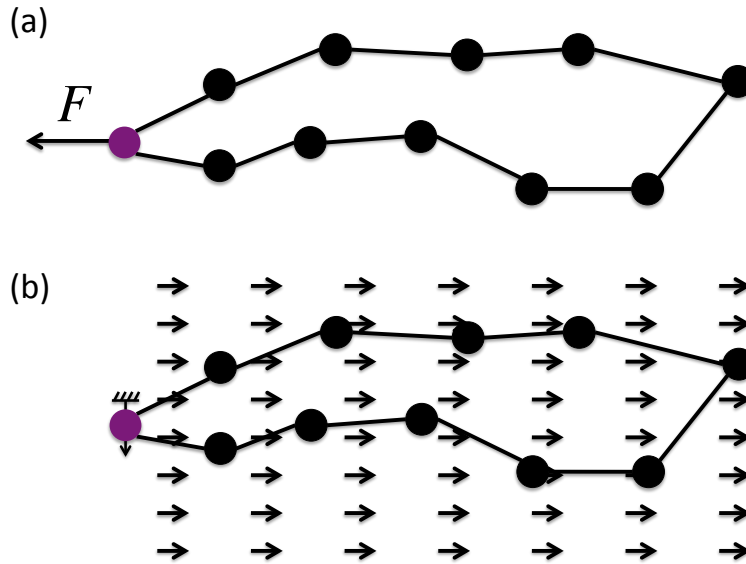


Fig. 2.1 Illustration of coordinate transformation. (a) a pulled polymer loop before transformation; (b) pinned polymer loop in an external field after transformation.

Now let us imagine we are sitting on the SPB. Then effectively, the SPB is pinned, and the polymer loop is immersed in a flow with velocity $-\mathbf{v}$, see in Fig. 2.1 (b). Let us assume the Stoke's law is valid and according to that, there is a force $\mathbf{F}^e = -\xi \mathbf{v}$ exerting on every bead. ξ is the friction coefficient for the bead in the solution.

In conclusion, the pulled polymer loop model is equivalent to the pinned polymer loop in an external force field. In our analysis, we will use the pinned polymer loop picture, because it is more easily to deal with both numerically and analytically. In the simulation, an extreme large pulling force is required if we use the first picture. The unusual force can easily become the bottleneck for the choosing of the integration time step. In theory, the force field picture offers a very clean energy landscape. Thus the pinned picture is preferred in our study.

2.1.2 Bead-rod model

Now let us come to a concrete polymer model for modeling the chromosomes, i.e. the bead-rod model. For this model, the beads representing chromosome segments are connected by the massless rigid rod. For simplicity, we assume the length of every rod is identical, denote by a . The rigidity of the rod means the distance between two neighboring beads is fixed.

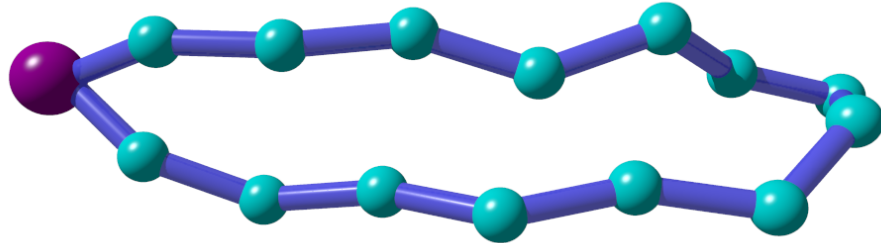


Fig. 2.2 Sketch of the bead-rod loop model. The magenta bead represents the SPB and other cyan beads represent the chromosome segments.

The dynamics of the polymer is specified by the motion of the beads. We shall first give out the dynamical equation and then explain how does it come from. Let us say the contour length of the polymer loop is L , i.e. there are L beads (including the SPB) and L rods in the polymer. Denote the beads by the index $i = 0, 1, 2, \dots, L-1, L$. Notice that the periodic index is used due to the looping structure, i.e. for any indexing quantities $x_0 = x_L$. Then the dynamical equation of i^{th} bead can be written as

$$\xi \frac{d\mathbf{r}_i}{dt} = \mathbf{F}_i^u + \mathbf{F}_i^c + \mathbf{F}_i^{pseudo} + \mathbf{F}_i^e + \mathbf{F}_i^b \quad (2.1)$$

where ξ is the friction coefficient of the bead in the solution, \mathbf{F}_i^u is the interaction force specified by some kind of potentials, \mathbf{F}_i^c is the constraint force that keeps the rod length fixed, \mathbf{F}_i^e is the external force and \mathbf{F}_i^b is the Brownian force caused by thermal fluctuations. And what is left in the right hand of Eq. (2.1) is \mathbf{F}_i^{pseudo} , which is a special type of force introduced in the bead-rod model in order to get the correct statistics. We will discuss more about it later.

Now let us come back to explain how does Eq. (2.1) come from. Firstly, notice that \mathbf{F}_i^b in the equation is a stochastic variable, so Eq. (2.1) is actually a stochastic differential equation. Secondly, the left-hand side of Eq. (2.1) is actually rearranged from the friction force of the bead in the solution $-\xi \mathbf{v}_i$. And we have assumed the solution is homogeneous so that the friction coefficient is independent of the space and time. Third, the inertial of the bead

is neglected due to millions of collisions per second from the water molecules. In another word, Eq. (2.1) essentially can be written as $\mathbf{F}_i^{total} = \mathbf{0}$. This is simply the Newton's law with inertial neglected. This kind of dynamics is commonly used in polymer physics and called Brownian Dynamics [110, 111].

Let us now discuss each term of the right-hand side of Eq. (2.1) one by one.

- Brownian force \mathbf{F}_i^b

The Brownian force can be caused by the enormous instantaneous collisions of the solvent molecules or by other sort of interactions between chromosomes and proteins in the nucleus. The level of fluctuation can be characterized by an effective temperature T . Mathematically, the Brownian force is described by a Gaussian process with the zero mean in space and time and the non-zero second moment, which can be written as:

$$\langle \mathbf{F}_i^b \rangle = \mathbf{0}, \quad (2.2a)$$

$$\langle \mathbf{F}_i^b(t) \mathbf{F}_j^b(t') \rangle = 2k_B T \xi \delta_{ij} \delta(t - t'), \quad (2.2b)$$

here, ξ is the friction coefficient. k_B is the Boltzmann constant. δ_{ij} is the Kronecker delta means there is no correlation for the Brownian force exerting on different beads. The second δ is the Dirac delta function.

- External force \mathbf{F}_i^e

The external force in our pinned polymer loop model is simply the equivalent flow field after coordinate transformation. So we have $\mathbf{F}_i^e = \xi \mathbf{v}_{SPB}$. In general, $\mathbf{v}_{SPB} = \mathbf{v}_{SPB}(t)$ is a function of time. However, when we consider the simplest case that the chromosome is pulled to move steadily in one direction, \mathbf{v}_{SPB} is a constant.

- Constraint force \mathbf{F}_i^c

The constraint force is the tension force on the rod to keep the length fixed. So the direction of the force is along the rod orientation. The rigid rod constraint can be written as

$$|\mathbf{r}_i - \mathbf{r}_{i-1}| - a = 0, \quad (2.3)$$

and $\mathbf{r}_0 = \mathbf{r}_L$ for the periodic indexing. The constraint force is an implicit force that depends on the other force exerting on the beads. We will discuss how to calculate this force in next section.

- *Pseudo* force \mathbf{F}_i^{pseudo}

The *Pseudo* force is a special virtual force that added in order to obtain the statistics we want. If we neglect the bending energy, excluded volume effect and other complex interactions in the model, we are essentially talking about the simplest freely joint polymer

model. For such a simple model, we expect the random walk statistics, i.e. the orientation of two consecutive rods is independent. So the distribution of the included angle of two rods should be uniform. However, we cannot obtain this statistics as we want without the *pseudo* force.

Let us take a simple example, the distribution of included angle of a trimer in 3D. Denote the angle as θ . The 3D spherical uniform distribution can be written as

$$p(\theta) = \text{const.} \sin \theta. \quad (2.4)$$

On the other hand, the distribution of rigid bead-rod trimer without *pseudo* force can be derived using the generalized coordinate

$$p(\theta) = \text{const.} (1 - \frac{1}{4} \cos^2 \theta)^{1/2} \sin \theta. \quad (2.5)$$

So they are not the same as we see here. The reason for this discrepancy is the rigidity of constraints reduce the phase space of the trimer from 6 dimensional gully to 4 dimension manifold. The simple Brownian force ensures the probability is uniform among the manifold but not θ .

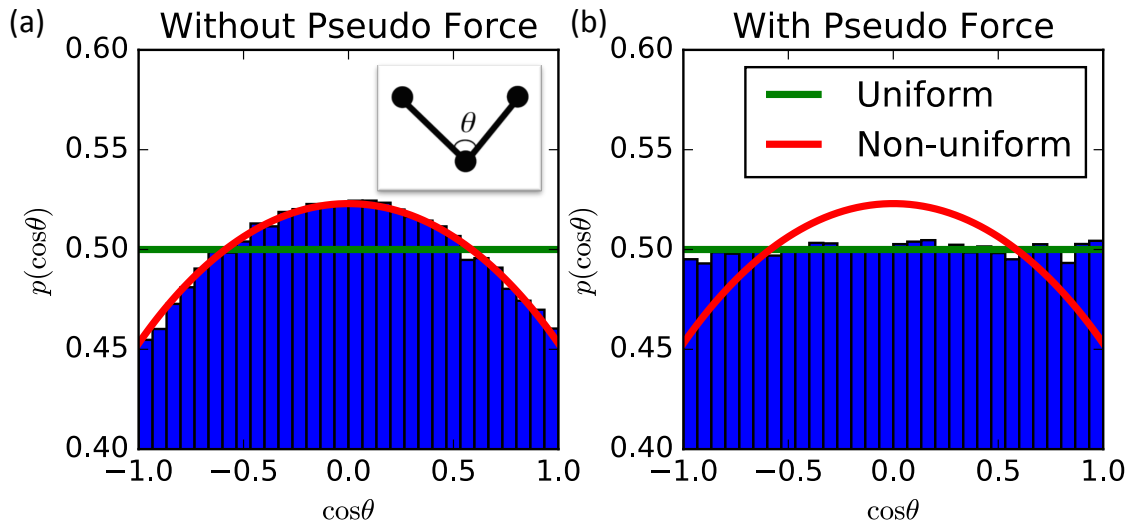


Fig. 2.3 The distribution of included angle of a bead-rod trimer. (a) without *pseudo* force; (b) with *pseudo* force. The blue bins are from Brownian Dynamics simulation results. Inset of (a) is a sketch for the trimer.

To solve the problem and obtain the statistics we want, Fixman introduced an effective *pseudo* potential depends on the polymer configuration [112], and hence we have a *pseudo*

force in Eq. (2.1). The explicit form of the *pseudo* force can be written as

$$\mathbf{F}_i^{pseudo} = -\frac{\partial U_{met}}{\partial \mathbf{r}_i}, \quad (2.6a)$$

$$U_{met} = \frac{1}{2} k_B T \ln(\det \mathbf{G}), \quad (2.6b)$$

where \mathbf{G} is the metric matrix of the bead-rod system [113]. We will show the details for the calculation of *pseudo* force in next section.

- Other potential forces \mathbf{F}_i^u

Other potential forces count the forces derived from bending energy, excluded volume effect, hydrodynamical interaction and other interaction potentials. The general form of this force can be written as

$$\mathbf{F}_i^u = -\sum_U \frac{\partial U}{\partial \mathbf{r}_i}, \quad (2.7)$$

here U can be different potentials. For instance, the bending potential can be calculated as

$$U_{bend} = -\frac{\kappa}{a} \sum_{i=1}^L \mathbf{u}_i \cdot \mathbf{u}_{i-1} \quad (2.8)$$

where $\mathbf{u}_i = (\mathbf{r}_i - \mathbf{r}_{i-1})/a$ is the unit vector of rod orientation, κ is the bending stiffness and a is the rod length.

For excluded volume effect, we usually model this interactive as pure repulsive Lennard-Jones potential

$$U_{LJ} = \begin{cases} 4\epsilon \left[\left(\frac{\sigma}{r} \right)^{12} - \left(\frac{\sigma}{r} \right)^6 \right], & \text{if } r \leq r_c; \\ 0, & \text{if } r > r_c; \end{cases} \quad (2.9)$$

where r is the distance between two beads and $r_c = 2^{1/6}\sigma$, ϵ and σ are two parameters.

One can add more interaction potentials into the model. However, adding more potentials could easily lead to a complex model with many parameters. For the sake of simplicity, we will actually ignore these forces in most of our analysis. See in our later chapters.

2.1.3 Bead-spring model

Bead-spring model is another commonly used polymer model. There are several reasons that we use the bead-spring model complementary with the bead-rod model. First, the bead-spring model can work as a benchmark model of the bead-rod model. Unlike the bead-rod model, a *pseudo* force have to be added to obtain the correct random walk statistics, the model of beads connected by Hookean springs is intrinsically a system satisfied the random walk statistics.

Second, the role of finite extensibility can be understood by comparing the bead-rod and bead-spring model. Third, the computation power needed for the bead-spring model is much less than the bead-rod because we avoid calculating the *pseudo* force and implicit constraint force. Let us now look at the details of our bead-spring model.

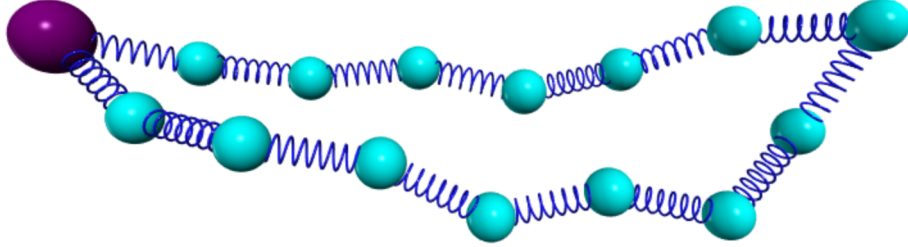


Fig. 2.4 Sketch of the bead-spring loop model. The magenta bead represents the SPB and other cyan beads represent the chromosome segments.

To model the chromosome in fission yeast during nuclear oscillation, we also need a looping structure like the bead-rod model above. The first bead represents the SPB, shown in Fig. 2.4. The dynamical equation is similar to the bead-rod model, can be written as following

$$\xi \frac{d\mathbf{r}_i}{dt} = \mathbf{F}_i^u + \mathbf{F}_i^{spring} + \mathbf{F}_i^e + \mathbf{F}_i^b. \quad (2.10)$$

The notations here are the same as the bead-rod model. In addition, the Brownian force, external force and the potential force are the same as in the bead-rod model. What is different is that the *pseudo* force is not needed and the constraint force is replaced by the spring force \mathbf{F}_i^{spring} . Notice that for a bead in the loop, there are two springs connecting to it. Thus

$$\mathbf{F}_i^{spring} = F_{i+1}^s(Q_{i+1})\mathbf{u}_{i+1} - F_i^s(Q_i)\mathbf{u}_i, \quad (2.11)$$

here, $F_i^s(Q_i)$ is the tension of the i^{th} spring and Q_i is the length of the spring. \mathbf{u}_i is the unit vector for the orientation of the i^{th} spring.

There are different types of springs one can use for the model. Here, we will introduce two most commonly used ones and both are used somewhere in the later chapters.

- Hookean spring

Hookean spring is a linear spring, where the tension of spring depends linearly on the length.

$$F^{Hookean} = H(Q - Q_0), \quad (2.12)$$

where H is the Hookean spring constant and Q_0 is the natural length of the spring. In practical Q_0 is set to a , which equals to the length of the bead-rod model. However, sometimes the zero length springs are used. We will point out when needed.

- Finite Extensible Nonlinear Elastic (FENE) spring

FENE spring is another commonly used spring. The force law of the spring is

$$F^{FENE} = \frac{HQ}{1 - (Q/R_0)^2}, \quad (2.13)$$

here R_0 is the maximal length of the spring. As we can see in Eq. (2.13), $F^{FENE} \rightarrow \infty$ when $Q \rightarrow R_0$.

In this section, we specify the dynamics and interaction details of our model for the meiotic chromosomes. The governing equations for the monomers are given. However, we have not talked about the special bead representing the SPB. We will discuss how to pin the SPB in next section.

2.2 Brownian Dynamics simulation method

After introducing the model, in this section, we will illustrate how to simulate the model numerically. Since we plan to do most of the theoretical analysis in the later chapters where the simulation results are used for the benchmark, it is convenient that we show the methods of simulation before that.

Brownian Dynamics (BD) simulation is a kind of Molecule Dynamics (MD) simulation technique. The governing equation of each monomer or particle is integrated to get the trajectories. And physical quantities are measured by ensemble average over trajectories of thousands of monomers. In our situation, the governing equations are Eq. (2.1) or Eq. (2.10). Our interested quantities are something like the average space distance between two beads, the typical size of the polymer and the characteristic time scale of the system dynamics. These are all tractable by BD simulations.

In the following subsections, we will introduce the algorithms used to do the bead-rod and bead-spring simulation separately. The simulation code is implemented in C++2011. Most the simulation are computed in our clusters with X86 architecture.

2.2.1 BD simulation of the bead-rod model

Essentially, the goal of the simulation is to solve the first order ordinary stochastic differential equation Eq. (2.1) numerically. However, the simple integration algorithm such as the Euler

algorithm would not work here. This is because of the implicit constraint force \mathbf{F}_i^c . Here we employ the predictor-corrector algorithm introduced by Liu [114].

To simplify the illustration of the algorithm, we will ignore all complex potential forces and the external force in Eq. (2.1), i.e. $\mathbf{F}_i^u = \mathbf{F}_i^e = \mathbf{0}$. It is easy to add them back after knowing the algorithm. The dynamical equation after simplification looks

$$\frac{d\mathbf{r}_i}{dt} = \frac{1}{\xi} \left(\mathbf{F}_i^c + \mathbf{F}_i^{pseudo} + \mathbf{F}_i^b \right). \quad (2.14)$$

The predictor-corrector algorithm is a two-step algorithm and can be divided into the prediction step and correction step. Let us discuss in details.

Prediction step

In the prediction step, the estimation of next time step bead position is evaluated without considering the constraints

$$\mathbf{r}_i^*(t + \Delta t) = \mathbf{r}_i(t) + \frac{1}{\xi} (\mathbf{F}_i^{pseudo} + \mathbf{F}_i^b) \Delta t. \quad (2.15)$$

In order to do the calculation, we need to evaluate the Brownian force and the *pseudo* force first. Here we will show how to do that one by one.

- Evaluation of the Brownian force \mathbf{F}_i^b

The Brownian force is mathematically generated by a Wiener process. Numerically, it is evaluated by a Gaussian distributed *pseudo* random number generated by the computer. Eq. (2.15) can be written more practically as

$$\begin{aligned} \mathbf{r}_i^*(t + \Delta t) &= \mathbf{r}_i(t) + \frac{1}{\xi} \mathbf{F}_i^{pseudo} \Delta t + \sqrt{\frac{2k_B T}{\xi}} d\mathbf{W}_i \\ &= \mathbf{r}_i(t) + \frac{1}{\xi} \mathbf{F}_i^{pseudo} \Delta t + \sqrt{\frac{2k_B T}{\xi} \Delta t} \mathbf{N}_i(0, 1), \end{aligned} \quad (2.16)$$

where $d\mathbf{W}_i$ is a Wiener process and $\mathbf{N}_i(0, 1)$ is a multi-dimensional Gaussian random number of mean 0 and variance 1.

- Evaluation of the *pseudo* force \mathbf{F}_i^{pseudo}

The expression for *pseudo* force is listed as Eq. (2.6). However, the evaluation is not easy and also expensive. To do that, let us first discuss the metric tensor \mathbf{G} .

$$G_{\alpha\beta} = \sum_i \frac{\partial g^\alpha}{\partial \mathbf{r}_i} \cdot \frac{\partial g^\beta}{\partial \mathbf{r}_i}, \quad (2.17)$$

where g^α is the rigid constraint that

$$g^\alpha(\mathbf{r}_1, \mathbf{r}_2, \dots, \mathbf{r}_L) = 0. \quad (2.18)$$

In the case of a bead-rod loop, Eq. (2.3) is the constraint. And the $L \times L$ metric tensor looks like

$$\mathbf{G} = \begin{bmatrix} d_1 & c_1 & 0 & \cdots & c_L \\ c_1 & d_2 & c_2 & \cdots & 0 \\ \vdots & \ddots & \ddots & \ddots & \vdots \\ 0 & \cdots & c_{L-2} & d_{L-1} & c_{L-1} \\ c_L & \cdots & 0 & c_{L-1} & d_L \end{bmatrix}, \quad (2.19)$$

where diagonal elements $d_i = 2$, and the off-diagonal elements

$$c_i = -\mathbf{u}_i \cdot \mathbf{u}_{i-1} \quad (2.20)$$

Again here, the periodic index is applied, i.e. $\mathbf{u}_0 = \mathbf{u}_L$. Now, the *pseudo* force can be calculated as

$$\begin{aligned} \mathbf{F}_i^{pseudo} &= -\frac{1}{2}k_B T \frac{\partial \ln(\det \mathbf{G})}{\partial \mathbf{r}_i} \\ &= -\frac{1}{2}k_B T \sum_{\alpha,\beta} \frac{1}{\det \mathbf{G}} \frac{\partial \det \mathbf{G}}{\partial G_{\alpha\beta}} \frac{\partial G_{\alpha\beta}}{\partial \mathbf{r}_i} \\ &= -\frac{1}{2}k_B T \sum_{\alpha,\beta} G_{\beta\alpha}^{-1} \frac{\partial G_{\alpha\beta}}{\partial \mathbf{r}_i}. \end{aligned} \quad (2.21)$$

In order to calculate the *pseudo* force, we need to inverse the matrix \mathbf{G} . This operation is very expensive. Fortunately, the symmetric shape of \mathbf{G} in Eq. (2.19) makes it possible to find an efficient algorithm to do the computation. We employ the algorithm developed by Pasquali and Morse in [113]. They developed this algorithm for BD simulation of a bead-rod chain. We modified it and successfully applied it to our bead-rod ring model. See Appendix X for details.

Now the prediction of next time step bead position can be calculated straight forward using Eq. (2.16). The evaluation of other types of forces is quite simple if needed. And we are ready to discuss the correction step.

Correction step

The correction step utilizes the result of the prediction, and correct it with the constraint force to obtain the real next time step bead position.

$$\mathbf{r}_i(t + \Delta t) = \mathbf{r}_i^*(t + \Delta t) + \frac{1}{\xi} \mathbf{F}_i^c \Delta t. \quad (2.22)$$

And we known that the rigid rod constraints must be satisfied after the correction. Substitute Eq. (2.22) into Eq. (2.3) and also notice that

$$\mathbf{F}_i^c = \lambda_{i+1} \mathbf{u}_{i+1} - \lambda_i \mathbf{u}_i \quad (2.23)$$

where λ_i is the magnitude of tension on the i^{th} rod. Thus we obtain

$$\begin{aligned} & 2\Delta t \mathbf{b}_i \cdot (\lambda_{i-1} \mathbf{u}_{i-1} - 2\lambda_i \mathbf{u}_i + \lambda_{i+1} \mathbf{u}_{i+1}) \\ &= \xi (a^2 - \mathbf{b}_i \cdot \mathbf{b}_i) - \frac{(\Delta t)^2}{\xi} (\lambda_{i-1} \mathbf{u}_{i-1} - 2\lambda_i \mathbf{u}_i + \lambda_{i+1} \mathbf{u}_{i+1})^2. \end{aligned} \quad (2.24)$$

And $\mathbf{b}_i = \mathbf{r}_i^*(t + \Delta t) - \mathbf{r}_{i-1}^*(t + \Delta t)$. This is a set of nonlinear algebra equations. The second term at the right hand side is the nonlinear term. We can see from here, the nonlinear term is small when the time step Δt is small enough. Numerically, it is suitable to use the iteration methods such like the Picard's method to solve this set of equations. High order methods like the Newton's method are also applicable but require the calculation of Jacobian matrix every time step. In practical, a small time step is necessary for the convergence of root searching. We use a time step between $10^{-5} - 10^{-3}$ depends on different situations.

Once we solve the tension λ_i , plug in to Eq. (2.23) and then Eq. (2.22), the next time step bead position can be calculated straight forward.

Finally, We want to discuss a little bit about how to pin the first bead of the bead-rod model. One has several possible ways to do this. The first one is to use a very stiff zero-length spring attached it to the first bead and certain point. This method is very easy to implement. However, the use of the pinning spring will introduce a high-frequency factor into the polymer dynamics. This is not good when we analysis of the polymer dynamics. And the spring length is not perfectly zero when the polymer is subjected to a strong force field. So we use another method, i.e. pin the first bead use the zero-length rigid rods. In fact, we will need

three this kind of “ghost” rods in 3D, the orientation of the rods along three axes respectively. This method requires solving the additional constraint forces. And the calculation is more or less the same as we stated here. With this method, the bead can be pinned perfectly and no disturbing factor will be introduced.

2.2.2 BD simulation of the bead-spring model

The BD simulation of the bead-spring model is much simpler than the bead-rod model. There is neither implicit force nor complex forces need to evaluate during every time step. Of course, one can also use an implicit algorithm which allowed the using of a larger time step. However, we will simply use the explicit algorithms since they work pretty well.

We will introduce here two simple algorithms to simulate the bead-spring ring polymer, i.e. the Euler method and the stochastic Runge-Kutta method.

Euler method

Euler method, also called Euler-Maruyama method, is a 1/2 order integration scheme. In principle, the convergence is only guaranteed when $\Delta t \rightarrow 0$. However, it is still widely used because of its simplicity, especially when the variation of the drift and diffusive term in the stochastic differential equation is not too large. The beads connected by Hookean spring is a good example fits this method.

Using this method, the next time step bead position in our simple example can be calculated as

$$\mathbf{r}_i(t + \Delta t) = \mathbf{r}_i(t) + \frac{1}{\xi} \mathbf{F}_i^{det} \Delta t + \sqrt{\frac{2k_B T}{\xi} \Delta t} \mathbf{N}_i(0, 1), \quad (2.25)$$

where $\mathbf{F}_i^{det} = \mathbf{F}_i^u + \mathbf{F}_i^{spring} + \mathbf{F}_i^e$ is the total deterministic force. Also notice that, the \mathbf{F}_i^{spring} is evaluated by Eq. (2.11) and the spring force law Eq. (2.12) or Eq. (2.13).

Stochastic Runge-Kutta method

Stochastic Runge-Kutta method is a higher order integration scheme than the Euler method. It was proposed by Honeycutt in [115]. In this method, the next time step bead position can be calculated as

$$\mathbf{r}_i(t + \Delta t) = \mathbf{r}_i(t) + \frac{1}{\xi} (\mathbf{F}_i^{det} + \tilde{\mathbf{F}}_i^{det}) \frac{\Delta t}{2} + \sqrt{\frac{2k_B T}{\xi} \Delta t} \mathbf{N}_i(0, 1), \quad (2.26)$$

where \mathbf{F}_i^{det} and $\tilde{\mathbf{F}}_i^{det}$ are the total deterministic force evaluated using different bead position.

$$\begin{aligned}\mathbf{F}_i^{det} &= \mathbf{F}_i^{det}(\mathbf{r}_0(t), \mathbf{r}_1(t), \dots, \mathbf{r}_{L-1}(t)), \\ \tilde{\mathbf{F}}_i^{det} &= \tilde{\mathbf{F}}_i^{det}(\mathbf{r}_0^*, \mathbf{r}_1^*, \dots, \mathbf{r}_{L-1}^*),\end{aligned}\quad (2.27)$$

and \mathbf{r}_i^* is the mid-step bead position

$$\mathbf{r}_i^* = \mathbf{r}_i(t) + \frac{1}{\xi} \mathbf{F}_i^{det} \Delta t + \sqrt{\frac{2k_B T}{\xi} \Delta t} \mathbf{N}_i(0, 1). \quad (2.28)$$

Last but not least, in the simulations, the dynamical equation is nondimensionalized by rescaling the variable in the following way:

$$\mathbf{r}' \rightarrow \mathbf{r}/a; t' \rightarrow t/(\xi a^2/k_B T); \mathbf{F}' \rightarrow \mathbf{F}/(k_B T/a). \quad (2.29)$$

After the rescaling, the length unit is set to the size of the rod. The rescaling is helpful to avoid doing calculations with very small or big numbers, which might introduce larger numerical errors.

2.3 Monte-Carlo simulation of the bead-rod model

In the previous section, we present the BD simulation technique of the bead-rod and bead-spring polymer loop. As we can see there, the algorithm used to simulate the bead-rod model is actually quite complex and also time-consuming. Sometimes we do not need to do that if we only want to sample the equilibrium properties of the bead-rod system. In this section, we will introduce a Monte-Carlo algorithm that is much faster and efficient to obtain the equilibrium statistics of the bead-rod loop model.

Monte-Carlo technique has been used to simulate the polymer system for a long time [116]. However, there are some special factors one needs to take into account for our pinned polymer loop model. Basically, one has to preserve the loop structure and keep the rod length fixed when trying to do a Monte-Carlo flip. According to this, we propose the following main steps of our Monte-Carlo algorithm.

- Step I: prepare an initial configuration and compute the energy of this configuration. The way of calculating system energy depends on the setting of the model, whether the excluded volume effect or other interactions are taken into account or not. For example, the

energy of a pinned bead-rod loop in a constant external force field can be written as

$$E = U - \sum_{i=1}^L \mathbf{F}^e \cdot \mathbf{r}_i \quad (2.30)$$

where U is other kind of interaction energy. In the simplest case, we will assume U is independent of the configurations. To compare with the later evaluation, we denote the energy calculated here E_{old} .

- Step II: randomly choice two beads in the polymer loop, use the connecting line between the two beads as a rotation axis.

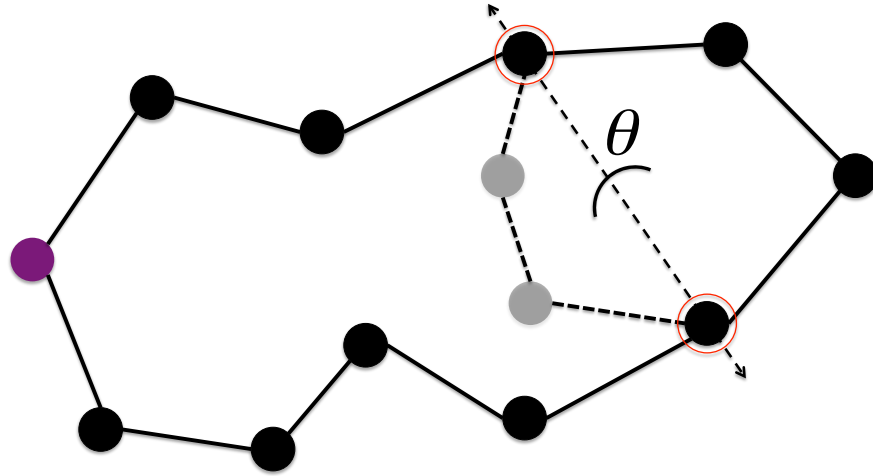


Fig. 2.5 Illustration of the Monte-Carlo configuration flip.

- Step III: choose the unpinned side of the polymer, and rotate this part of the polymer by a random angle $\theta \in [-\phi, \phi]$. ϕ is a parameter between $[0, \pi]$ and can be tuned to improve the efficiency of the algorithm. See in Fig. 2.5. If the pinned bead is selected, then randomly choose a side of the polymer to do the rotation.
- Step IV: calculated the energy of the configuration after rotation in the same way of E_{old} . Let us denote the new energy as E_{new} .
- Step V: the new configuration is accepted with probability

$$p = \min \left\{ 1, \exp \left(-\frac{\Delta E}{k_B T} \right) \right\}, \quad (2.31)$$

where $\Delta E = E_{new} - E_{old}$. If not accepted, then the polymer returns to the old configuration, and try again with new random number. An efficient sampling algorithm can be tuned by parameter ϕ so that the accept probability is around 0.5.

- Step VI: go back to step I and loop again and again to get enough independent samples. Physical quantities such like the statistical distance between two beads can be calculated by averaging over these samples.

The Monte-Carlo method introduced in this section is efficient and fast, we will use it to calculate most of the equilibrium quantities in next chapter. On the other hand, the Monte-Carlo results also work as a benchmark of the BD simulation and vice-versa.

2.4 Summary

In this chapter, we elaborated the details of our pulled polymer model for the chromosomes in meiotic fission yeast. We have shown that the pulled polymer loop is equivalent to the pinned polymer loop in external force field after a coordinate transform. The concrete bead-rod and bead-spring polymer loop models are discussed. And the BD simulation technique is discussed in details. A Monte-Carlo algorithm is introduced to calculate the equilibrium statistics of the bead-rod system and overcomes the disadvantages of heavy computation for the BD simulation.

The content of this chapter will be very useful in our later chapters. And we try to keep it concise, many related interesting models or methods are not mentioned here. Only those that will use in this thesis are discussed. Interested readers can refer to the cited references.

In next chapter, we will start to discuss the theory of equilibrium statistics of our polymer model and use the theory to explain the chromosome alignment in fission yeast.

Chapter 3

Equilibrium Statistics Applied to Chromosome Alignment

In previous chapter, we introduced the details of our polymer loop model for chromosomes and the simulation techniques. In this chapter, we will investigate the equilibrium statistics of the model and use the results to understand the chromosome alignment in fission yeast.

In order to tract the model analytically, we will neglect the complex interactions such as bending energy, excluded volume effect and hydrodynamical perturbations. In another word, our model is the simplest freely-jointed polymer loop model. The transferred coordinate is utilized so that the first bead representing SPB is pinned. And an external force field will be applied. The impact of those complex interactions will be studied numerically in the chapter 5.

We will start by introducing the setting of the model in the first section. The equilibrium statistics of 1D and 3D are discussed separately in section two and three. In the last two section, we will go back to the circumstance of fission yeast and discuss about some applications.

3.1 Pinned polymer loop in a constant force field

As we know, the nuclear oscillation in fission yeast is an oscillating dynamics. So in principle, the system is out of equilibrium by definition. However, notice that the time period of the nuclear oscillation is about 10 mins. The oscillation can be divided into two parts. The chromosomes move towards to the opposite direction in each part. If the relaxation time of the system is much smaller than half of the oscillation period, then it is proper to think the system as a equilibrium system. Actually, we will show in next chapter that this is indeed

true. The relaxation time of the chromosome system is calculated. It turns out the relaxation time scale is ~ 10 s. So the equilibrium assumption is justified.

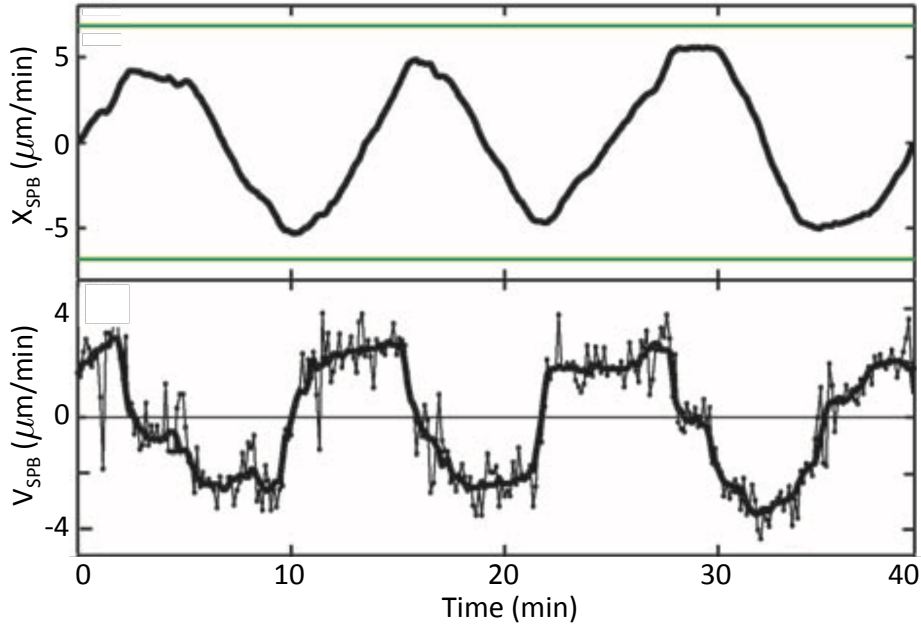


Fig. 3.1 Experimental trajectory and velocity of the SPB measured by fluorescence microscopy. The upper panel shows the trajectory of the SPB along the cell main axis. Green line is the boundary of the cell. The lower panel shows the corresponding velocity of the SPB. Image reprinted and modified from [5].

On the other hand, experimental evidence shows that the velocity of the SPB is almost constant when moving towards one direction. See in Fig. 3.1. So the corresponding setting of our model is pinned polymer loops in an constant external force field $\mathbf{F} = \xi v_{SPB}$. It is interesting to know what is the equilibrium statistics of this setting from theoretical point of view. In this chapter, we will use the bead-rod model to study this problem.

Let us first clarify some notations here. There are L beads (including the SPB) in the loop and the SPB is denoted by \mathbf{r}_0 or \mathbf{r}_L in periodic indexing. Without loss of generality, we assume it is pinned to the origin point, i.e. $\mathbf{r}_0 = \mathbf{r}_L = \mathbf{0}$. The length of each rod is a . And the constant external force field denotes by \mathbf{F} is in the z direction. The potential energy of the pinned polymer loop can be written as:

$$E = E_0 - a \sum_{i=1}^L \mathbf{F} \cdot \mathbf{r}_i \quad (3.1)$$

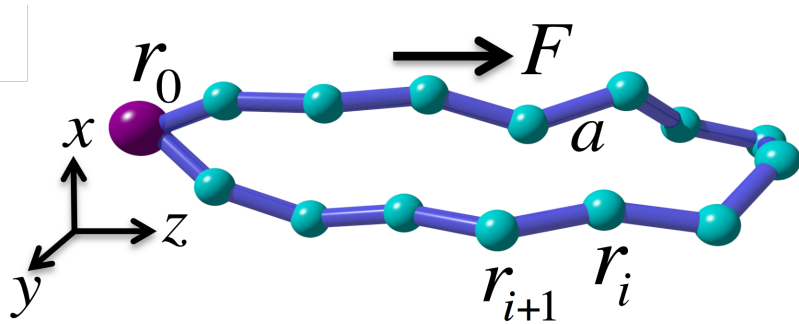


Fig. 3.2 Sketch for the pinned bead-rod loop and notations.

where E_0 is assumed to be a constant that denotes configuration independent energy. It is not important for the study of equilibrium statistics, we keep it here just for completeness. The orientation of the j^{th} rod is denoted by $\mathbf{u}_j = (\mathbf{r}_j - \mathbf{r}_{j-1})/a$. So the i^{th} bead position can be written as:

$$\mathbf{r}_i = a \sum_{j=1}^i \mathbf{u}_j. \quad (3.2)$$

Plug it into Eq. (3.1), we arrive at

$$E = E_0 - a \sum_{i=1}^L \sum_{j=1}^i \mathbf{F} \cdot \mathbf{u}_j. \quad (3.3)$$

Notice that the looping condition indicates

$$\sum_{j=1}^L \mathbf{u}_j = 0. \quad (3.4)$$

In the following two sections, we will solve the equilibrium statistics in 1D first and extend the theory to 3D.

3.2 Pinned Polymer Loop in 1D

As the same strategy to study many problems in physics, let us start to solve the equilibrium statistics from the simplest 1D case. The one dimensional polymer is possible because we neglect the exclusion volume effect so that the beads and rods are free to overlap. It is a simple idealized model. We will show in the following that an elegant mapping for the one dimensional pinned polymer loop to a famous classical physical model can be found.

3.2.1 Mapping to particles on 1D lattice

The pinned polymer in 1D is very simple. The configuration of the polymer can be specified by the orientation of the rods. In 1D, there are only two possible orientations for all rods, i.e. along the axis or against the axis.

Let us denote the j^{th} rod orientation by $u_j \in \{-1, +1\}$, where $u_j = +1$ means the rod orientates along the axis and $u_j = -1$ means the rod orientates against the axis. Again the i^{th} bead position in 1D is $z_i = a \sum_{j=1}^i u_j$. Now let us introduce a shifted and rescaled variable

$$n_j = (u_j + 1)/2. \quad (3.5)$$

We can easily find that $n_j \in \{0, 1\}$. The configuration of the 1D polymer can be denoted by $\{n_1, n_2, \dots, n_L\}$. Since n_j is a binary variable, we can interpret $n_j = 1$ as a lattice site occupied by a particle, and $n_j = 0$ as an empty lattice site. In this way, we find a one-to-one mapping from the configuration of polymers to particles on lattice sites. See in Fig. 3.3. The number of rods equals to the number of lattice sites. Without loss of generality, we have shown in the figure the right-orientated rod corresponds to an occupied site, and the left-orientated rod corresponds to an empty site.

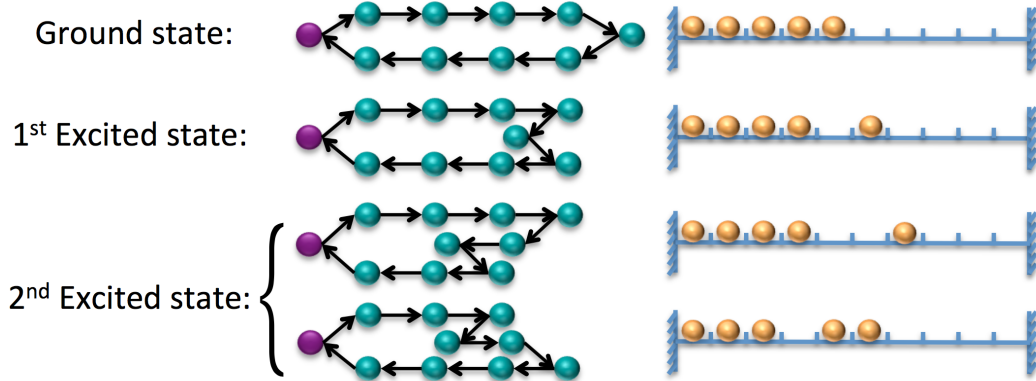


Fig. 3.3 Illustration for the mapping from 1D pinned polymer loop to Fermionic particles on 1D lattice sites.

Here are some remarks for the mapping:

- The mapped particles are exclusive to each other. It is not possible for one lattice site to be occupied by more than one particles. In another word, these particles are Fermions. This is because the system is a two state system, there is no correspondent polymer state for a site occupied by more than one particle.
- According to the looping condition Eq. (3.4), the total number of rods pointing to the right must be exact $L/2$. Correspondingly, the total number of particles also must be exact

$L/2$, i.e.

$$\sum_{j=1}^L n_j = \frac{L}{2}. \quad (3.6)$$

Furthermore, the number of particles must be conserved during the change of configurations.

- The dynamics of 1D polymer can be mapped to the particle hopping process on the 1D lattice. This part will be discussed in next chapter.
- The mapping is essentially from a two state system to a two state system. One can also interpret the two state as spin up and spin down or any other two state systems. We use the particle-lattice interpretation because it is familiar and intuitive to most people.

Now let us discuss the energy of the system. Rewrite Eq. (3.3) in 1D we get

$$E = E_0 - Fa \sum_{i=1}^L \sum_{j=1}^i u_j. \quad (3.7)$$

Exchange the summation order in Eq. (3.7) and utilizing the loop condition $\sum_{j=1}^L u_j = 0$ we obtain

$$E = E_0 + Fa \sum_{j=1}^L j u_j. \quad (3.8)$$

Let us look at the energy from the particle-lattice picture. Substitute Eq. (3.5) into Eq. (3.8), we arrive at

$$E = \tilde{E}_0 + \Delta E \sum_{j=1}^L j n_j \quad (3.9)$$

where $\Delta E = 2Fa$ and $\tilde{E}_0 = E_0 - L(L+1)\Delta E/4$ is the unimportant energy offset. Let us ignore the offset in our discussion. Eq. (3.9) can be reinterpret as the summation energy of L lattice sites. When $n_j = 1$ (occupied site), we gain a energy of $j\Delta E$ and zero otherwise. One can clearly see that Eq. (3.9) is the energy of a system of $L/2$ fermions distributed over L equidistant energy levels $\Delta E, 2\Delta E, \dots, L\Delta E$. The lowest energy (ground state) corresponds to the configuration that the left half of lattice sites are fully filled by particles. And the corresponding polymer picture is the fulled stretched configuration. The correspondence of the 1st and the 2nd excited states also can be imagined, which is shown in Fig. 3.3.

The mapping from the polymer to the particle-lattice picture is very useful for searching the solution of equilibrium statistics. In the following subsections, we will solve the 1D statistics using two different methods. The first one based on the grand canonical ensemble is an approximate solution with a simpler formulism, while the second one is the exact solution based on the canonical ensemble but a more complex formulism. We will calculate the mean

position of beads and their variance. Because these are what we interested, the biological interactions can only happen when two segments are closer enough.

3.2.2 The grand canonical ensemble solution

We have mentioned in the previous subsection that the particle number is conserved to $L/2$ in the mapped particle-lattice picture. So in principle, the system is a canonical ensemble system. However, let us first release this constraint by allowing the particles exchange with the reservoir at both sides of the lattice. Thus the grand canonical ensemble can be applied. After that, we can reimpose the constraint using the Brownian bridge technique. We can obtain very accurate mean bead position and its variance use this method. Given that the formulation of this method is simple, we are quite satisfied with the results. Let us now illustrate the method in details.

The Fermi-Dirac statistics

As we have mentioned above, the particles on the lattice are Fermions. One wonderful thing of the grand canonical ensemble is the particles can be assumed to be mutually independent. So that we can directly use the famous *Fermi-Dirac* distribution. That is to say the probability of a lattice site is occupied can be written as

$$\mathbb{P}\{n_j = 1\} = \frac{1}{1 + \exp\left[\frac{\Delta E(j-\mu)}{k_B T}\right]}, \quad (3.10)$$

where μ is the chemical potential $\mu = (L+1)/2$ obtained from the requirement that on average there are $L/2$ particles in the system. And accordingly, the probability that a lattice site is empty writes

$$\mathbb{P}\{n_j = 0\} = 1 - \mathbb{P}\{n_j = 1\}. \quad (3.11)$$

Let us define a dimensionless quantity which we call it *dimensionless temperature*:

$$\tilde{T} = \frac{k_B T}{\Delta E} = \frac{k_B T}{2Fa} \quad (3.12)$$

Now we can see in Fig. 3.4 for an illustration of the *Fermi-Dirac* distribution of different \tilde{T} . When \tilde{T} is small, namely the external force is large, the distribution shows a strong bias. The left half sites are more likely to be occupied and the right half sites are more likely to be empty. In the polymer picture, this means the orientation of the first half rods is biased in the direction of force, whereas the second half of rods are more probable to point against the

force field. Physically, it is easy to understand because the pinned polymer in strong force field is almost stretched.

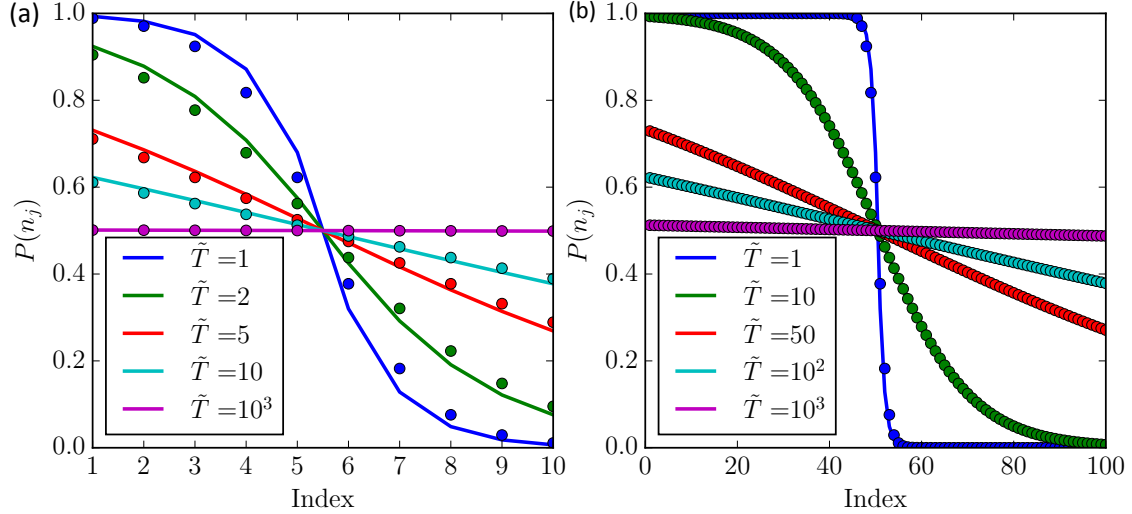


Fig. 3.4 Fermi-Dirac distribution compared with the exact solution from the number partition theory. Solid lines are the exact solution while the dots are Fermi-Dirac approximations. Different dimensionless temperature is indicated by different colors as shown in the legend. (a) $L = 10$, (b) $L = 100$.

With Eq. (3.10), the mean and variance of random variable n_j can be calculated straightforwardly:

$$\langle n_j \rangle = \mathbb{P}\{n_j = 1\}, \quad (3.13a)$$

$$\text{var}[n_j] = \mathbb{P}\{n_j = 1\} \cdot \mathbb{P}\{n_j = 0\} - \langle n_j \rangle^2. \quad (3.13b)$$

On the other hand, from Eq. (3.2) and Eq. (3.5) we can calculate the position of bead as

$$z_i = a \left(2 \sum_{j=1}^i n_j - i \right). \quad (3.14)$$

If we assume n_1, n_2, \dots, n_L are all mutually independent, then the mean and variance of bead position can simply calculated as

$$\langle z_j \rangle = a \left(2 \sum_{j=1}^i \langle n_j \rangle - i \right), \quad (3.15a)$$

$$\text{var}[z_j] = 4a^2 \sum_{j=1}^i \text{var}[n_j] \quad (3.15b)$$

The results of the above equations can be compared to the Monte-Carlo simulation (see Appendix B for details). We found that the formula for mean bead position works perfect. However, the formula for variance does not work so good. Notice that Eq. (3.15b) is monotonically increasing with the index i . We can take the simple symmetric argument that $\text{var}[z_i] = \text{var}[z_{L-i}]$. The result after that still can not match with the simulations. See in Fig. 3.5.

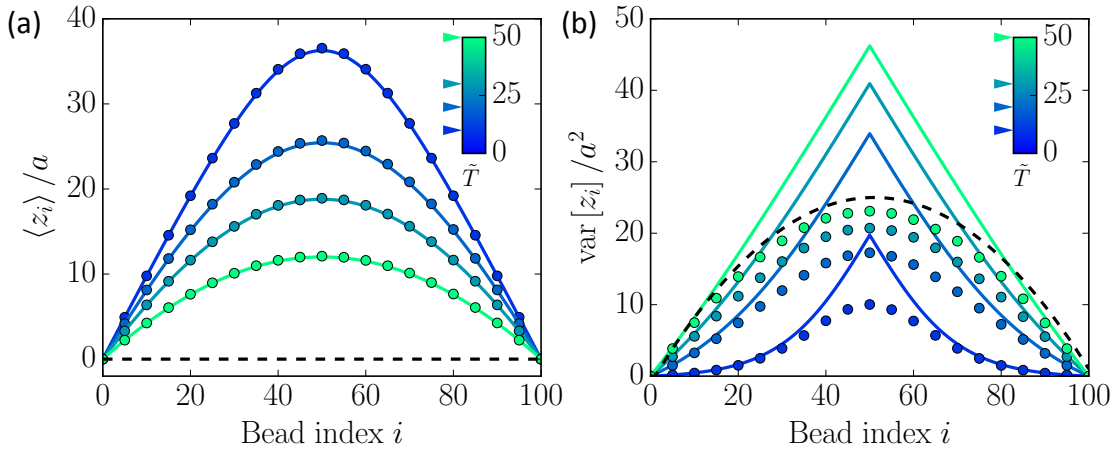


Fig. 3.5 Mean and variance of the 1D pinned polymer bead positions. MC simulation results (dots) are compared with theoretical results (solid lines) Eq. 3.15. The length of the polymer loop $L = 10$. The black dash line indicates the case $\tilde{T} \rightarrow \infty$, i.e. no external force field.

The reason for this mismatch is simple, the particles are not exactly independent and the loop condition is only fulfilled on average by choosing the chemical potential $\mu = (L + 1)/2$ in Eq. (3.10). In the following part, we will show how to solve this problem use the Brownian bridge technique.

The Brownian bridge condition

Let us consider the polymer loop as a random walk that returns to the origin point after L steps. This sort of random walk process is called the Brownian bridge [117, 118]. So each rod represents a random walk step. The segment connecting the k^{th} and the l^{th} bead corresponds to the propagator $\rho(z_l = z | z_k = 0)$. According to the Lindeberg-Feller central limit theorem [117], this propagator is Gaussian with the mean and variance equal to the sum of the mean and variance of all individual steps from k to l .

As we said above, the grand canonical ensemble only ensures the loop condition on average. To solve the problem, we now impose the Brownian bridge condition so that every single trajectory fulfills the loop condition. The Brownian bridge can be formulated as

following:

$$\rho^L(z_i = z) = \frac{\rho(z_i = z | z_0 = 0) \rho(z_{L-i} = z | z_L = 0)}{\rho(z_L = 0 | z_0 = 0)}, \quad (3.16)$$

where $\rho(z_i = z)$ is the probability density function of finding the i^{th} bead at position z , $\rho(z_k = z | z_j = 0)$ are the propagators. Eq. (2.2) means that the probability density equals two pieces of random walk trajectory of length i and $L - i$ meet at position z on the condition that they are belong to the same loop.

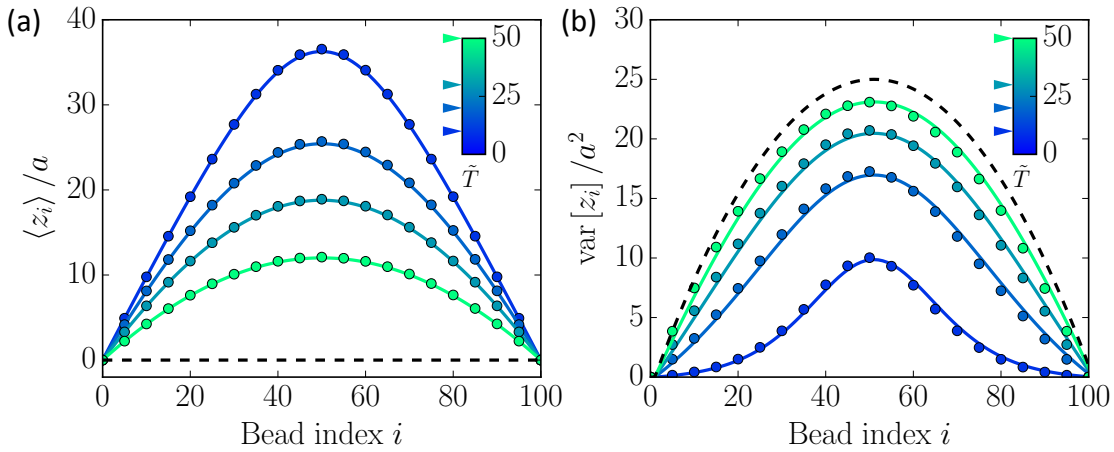


Fig. 3.6 Mean and variance of the 1D pinned polymer bead positions. MC simulation results (dots) are compared with theoretical results (solid lines) Eq. 3.18. The length of the polymer loop $L = 10$. The black dash line indicates the case $\tilde{T} \rightarrow \infty$, i.e. no external force field.

Notice that the propagators are Gaussian with the variance added up by the variance of individual steps, i.e Eq. (3.15b). So that $\rho^L(z_i = z)$ is also Gaussian. Its variance is given by

$$\text{var}[z_i] = 4a^2 \frac{\sum_{j=0}^i \text{var}[n_j] \sum_{j=L-i}^L \text{var}[n_j]}{\sum_{j=0}^L \text{var}[n_j]}. \quad (3.17)$$

Plug in Eq. (3.13b) and Eq. (3.15b) we can obtain the variance of bead position in the loop. For $\tilde{T} \gg 1$, we can obtain the close form expressions for mean and variance of bead position by converting the summation to integral

$$\langle z_i \rangle = 2a\tilde{T} \ln \left[\frac{1 + \exp\left(\frac{L}{2\tilde{T}}\right)}{\exp\left(\frac{i}{2\tilde{T}}\right) + \exp\left(\frac{L-i}{2\tilde{T}}\right)} \right] \quad (3.18a)$$

$$\text{var}[z_i] = 2a^2\tilde{T} \frac{\sinh\left(\frac{L-i}{2\tilde{T}}\right) \sinh\left(\frac{i}{2\tilde{T}}\right)}{\sinh\left(\frac{L}{2\tilde{T}}\right) \cosh^2\left(\frac{L-2i}{4\tilde{T}}\right)} \quad (3.18b)$$

We can see from the above formulas that the $z_i - z_{L-i}$ symmetry is satisfied. And a strong external force field leads to a stretched configuration and a small fluctuation of bead position. This result is compared with the Monte-Carlo simulations, see in Fig. 3.6.

In this subsection, we solved the mean and variance of bead position for 1D pinned polymer loop in an external force field. The strategy is using the *Fermi-Dirac* statistics and re-enforce the loop condition by the Brownian bridge technique. Excellent results verified by the Monte-Carlo simulation are obtained. However, we have to say, this is just an approximate method. In the next subsection, we will use the canonical ensemble to obtain the exact solution.

3.2.3 Canonical ensemble solution

In the particle-lattice picture, the system is actually a canonical ensemble system because of the conservation of particle number. In this section, we will calculate the exact partition function using this ensemble. More interestingly, we will show the calculation can be recoded to a number partition problem. Exact results are obtained and compared with the results from the approximate approach above.

The number partition theory

Before the calculation of exact partition function, let us discuss an interesting number partition problem that share a lot of similarities with the former.

Consider a non-negative integer number K , which can be expressed into the summation of N non-negative integers:

$$K = \sum_{j=1}^N k_j \quad (3.19)$$

However, there is a constraint on the summation components $0 \leq k_1 \leq k_2 \cdots \leq k_N \leq M$. This kind of problem can be best visualized by what called Young diagram [119], shown in Fig. 3.7. In the Young diagram, each row represents a integer number. The number of blue boxes means the value of the j^{th} integer. Starting from the bottom, because of the constraint, the diagram is non-decreasing.

The question is, given a certain integer K , how many different ways are there to partition it into N non-decreasing pieces $\{k_1, k_2, \dots, k_N\}$. For the simple cases, one can tell the answer immediately. For examples, in the first two examples of Fig. 3.7, we illustrate that there are only one way to partition integer 0 or 1 into 4 non-decreasing integers. However, this question in the general case is not intuitive. Fortunately, this problem is well studied by mathematicians. Let $g(M, N; K)$ denote the number of partitions of K with at most N parts,

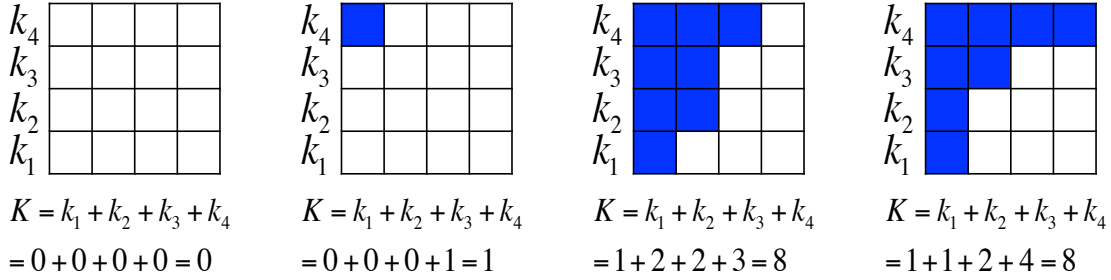


Fig. 3.7 Some examples of the Young diagram.

each of size at most M . Equivalently, these are the partitions whose Young diagram fits inside an $N \times M$ rectangle. Then we have the following generating function:

$$\Phi(q) := \sum_{K=0}^{MN} g(M, N; K) q^K = \binom{M+N}{N}_q \quad (3.20)$$

where q is an auxiliary number, and the notation at the right hand side of Eq. (3.20) is called q binomial coefficient or Gaussian binomial coefficient. It is defined as

$$\binom{L}{N}_q := \frac{[L]_q!}{[L-N]_q! [N]_q!}, \quad (3.21)$$

and $[N]_q := 1 + q + q^2 + \dots + q^{N-1}$ is called a q number [119].

Exact partition function

Now, let us start to calculate the partition function of our pinned polymer in the particle-lattice picture. The partition function of a canonical ensemble system with discrete energy can be written as:

$$\mathcal{Z}(T) = \sum_E g(E) \exp\left(-\frac{E}{k_B T}\right), \quad (3.22)$$

where $g(E)$ is the degeneracy of the microscopic states which have the same energy E . Once $g(E)$ is known, the partition function can be calculated straightforwardly.

Let us take a look at the energy of the system, i.e. Eq. (3.9). It is represented in the way of rod orientation u_j or occupation variable n_j . Here, we are going to use another way to represent the energy. In the particle-lattice picture, the system consists $N := L/2$ particles.

So the energy can be rewritten as:

$$E = \tilde{E}_0 + \sum_{j=1}^N E_j, \quad (3.23)$$

where E_j is the energy of the j^{th} particle in the external force field. Again, \tilde{E}_0 is an unimportant constant energy offset. Denote the position of the j^{th} particle as x_j , which is an integer $x_j \in [1, L]$. Then we can write $E_j = x_j \Delta E$. Also notice that, because of the exclusive condition, the sample space of the particle system is constrained in $\Omega = \{\mathbf{x} | 1 \leq x_1 < x_2 < \dots < x_N \leq L\}$.

Let us do a shift for the particle position by defining

$$k_j := x_j - j. \quad (3.24)$$

Notice now the constraint on x_j is transferred to $0 \leq k_1 \leq k_2 \dots \leq k_N \leq N$. And the energy of the system can be rewritten as:

$$E = \hat{E}_0 + \Delta E \sum_{j=1}^N k_j = \hat{E}_0 + K \Delta E, \quad (3.25)$$

Again \hat{E}_0 here is an unimportant constant energy offset, $\hat{E}_0 = \tilde{E}_0 + N(N+1)/2$. It is not difficult to find the range of the energy is $\hat{E}_0, \hat{E}_0 + \Delta E, \dots, \hat{E}_0 + N^2 \Delta E$.

Now we are closer to the number partition problem. Notice that $K = \sum_{j=1}^N k_j$ and we have the same type of constraint as in the number partition problem. In addition, because the mapping from integer K to energy E is one-to-one. So the degeneracy function $g(E)$ is exactly the number of ways to partition the integer K . Furthermore, let us denote $q := \exp(-\Delta E/k_B T)$. Then we have

$$\begin{aligned} \mathcal{Z}(T) &= \sum_E g(E) \exp\left(-\frac{E}{k_B T}\right) \\ &= \exp\left(-\frac{\hat{E}_0}{k_B T}\right) \sum_{K=0}^{N \times N} g(N, N; K) q^K \\ &= \exp\left(-\frac{\hat{E}_0}{k_B T}\right) \binom{L}{N}_q. \end{aligned} \quad (3.26)$$

With the exact partition function Eq. (3.26), the equilibrium distribution can be calculated straightforwardly:

$$P^e = \frac{1}{\mathcal{Z}(T)} \exp\left(-\frac{E}{k_B T}\right) = \frac{q^K}{\binom{L}{N}_q}. \quad (3.27)$$

We can see here the offset energy is not in the distribution function. That is why we always say it is not important. In principle, Eq. (3.27) is not an exact relation. It might still have a constant pre-factor which can be fixed by the normalization condition $\sum_{K=0}^{N^2} P^e = 1$. However, the constant is not important for our discussions, so we will just keep it in the form of Eq. (3.27).

With Eq. (3.26) and Eq. (3.27), in principle, one can calculate whatever equilibrium quantities. Here, we will calculate the probability distribution of rod orientation in order to compare with our previous approach based on grand canonical ensemble.

Exact probability distribution of the rod orientation

The probability distribution of rod orientation is equivalent to the probability distribution of the lattice site occupation. Previously, we have employed the *Fermi-Dirac* distribution. In this subsection, we will calculate the exact distribution of $\mathbb{P}\{n_j = 1\}$ to show how accurate the *Fermi-Dirac* distribution is.

In order to do that, let us first rewrite the equilibrium distribution Eq. (3.27) in the coordinate of particle position:

$$P^e(x_1, x_2, \dots, x_N) = q^{-\frac{N(N+1)}{2}} \binom{L}{N}_q^{-1} \prod_{i=1}^N q^{x_i}. \quad (3.28)$$

Now let us denote $P_i(x)$ the probability that the i^{th} particle is at position x . Then $P_i(x)$ can be calculated as

$$\begin{aligned} P_i(x) &= \sum_{1 \leq x_1 < \dots < x_{i-1} \leq x-1} P^e(x_1, x_2, \dots, x_N) \\ &\times \sum_{x < x_{i+1} < \dots < x_N \leq L} P^e(x_1, x_2, \dots, x_N) \\ &= q^{(N+1-i)(x-i)} \binom{x-1}{i-1}_q \binom{L-x}{N-i}_q \Bigg/ \binom{L}{N}_q. \end{aligned} \quad (3.29)$$

Finally, the probability that the j^{th} sites is occupied can be calculated as

$$\mathbb{P}\{n_j = 1\} = \sum_{i=1}^N P_i(x = j) \quad (3.30)$$

Eq. (3.30) simply means the probability of one site is occupied is the sum of the probability that it is occupied by any particles. Plug in Eq. (3.29), one can obtain the exact occupation probability distribution. This is compared with the *Fermi-Dirac* distribution in Fig. 3.4. As we can see in the figure, the discrepancy is quite small. It is only noticeable for a small lattice size at very strong external force field, see in Fig. 3.4 (a). So the Fermi-Dirac distribution is actually a very accurate approximation.

In this section, we solve the equilibrium statistics of the pinned polymer loop model in 1D. Utilizing the mapping from the polymer to a particle-lattice system, we solve the statistics by two different approaches. The first one employs the famous *Fermi-Dirac* distribution and the Brownian bridge technique. However, it is an approximate method. The second method based canonical ensemble and number partition theory is an exact solution. The exact results are compared with the first methods as well as the Monte-Carlo simulations. Our theory matches very well to the simulation results. In next section, we will extend our theory to the 3D system.

3.3 Equilibrium statistics in 3D

In 3D, the equilibrium statistics of the pinned polymer loop model can still be calculated using the similar strategy. The orientation of rods have two more degree of freedom in 3D. As shown in section 3.1, the external force is assume in the z direction. Let us use the spherical coordinates to describe the polymer system. Denote θ_j the angle between the j^{th} rod and the z -axis, and ϕ_j the rotational angle along z -axis. Then the loop condition along the force direction can be written as

$$\sum_{j=1}^L \cos \theta_j = 0. \quad (3.31)$$

Using the above condition, the energy of the 3D polymer Eq. (3.3) can be rewritten as

$$E = E_0 + Fa \sum_{j=1}^L j \cos \theta_j. \quad (3.32)$$

In the following subsections, we will first derive the partition function, and then calculate the mean and variance of the three dimensional beads position.

3.3.1 Partition function

To calculate the equilibrium statistics of 3D bead-rod system, we will use the approach of grand canonical ensemble combined with the Brownian bridge condition. The grand canonical ensemble partition function can be written as:

$$\mathcal{Z} = \prod_{j=1}^L \mathcal{Z}_j = \prod_{j=1}^L \int_0^{2\pi} d\phi \int_0^\pi \exp\left(-\frac{(j-\mu) \cos \theta \Delta E}{k_B T}\right). \quad (3.33)$$

Here, $\mu = (L+1)/2$ is the chemical potential the same as in 1D. However, $\Delta E = Fa$ is different from the 1D case. Again, let us define the *dimensionless temperature*:

$$\tilde{T} = \frac{k_B T}{\Delta E} = \frac{k_B T}{Fa}. \quad (3.34)$$

There is a factor of two compare to the dimensionless temperature in 1D.

The integration can be calculated in Eq. (3.33), which turns out

$$\mathcal{Z}_j = \frac{\tilde{T} \sinh \frac{j-\mu}{\tilde{T}}}{j-\mu}. \quad (3.35)$$

So the mean and variance of the j^{th} rod orientation $u_{j,z} = \cos \theta_j$ can be calculated as

$$\begin{aligned} \langle \cos \theta_j \rangle &= \tilde{T} \partial_\mu \ln \mathcal{Z}_j = \coth \frac{\mu-j}{\tilde{T}} - \frac{\tilde{T}}{\mu-j}, \\ \text{var} [\cos \theta_j] &= \tilde{T}^2 \partial_\mu^2 \ln \mathcal{Z}_j = \frac{\tilde{T}^2}{(j-\mu)^2} - \operatorname{csch}^2 \frac{j-\mu}{\tilde{T}}. \end{aligned} \quad (3.36)$$

Notice that, for symmetry reasons, the average projection for x and y directions are zero: $\langle u_{j,x} \rangle = \langle u_{j,y} \rangle = 0$. The second moment of these component can be calculated as

$$\langle u_{j,x}^2 \rangle = \langle u_{j,y}^2 \rangle = (1 - \langle \cos^2 \theta_j \rangle)/2 \quad (3.37)$$

The above equations give the statistical properties of individual rod orientation. In next subsection, we will use the Brownian bridge technique to calculate the mean and variance of beads position.

3.3.2 Mean and variance of the bead position

In the case of 3D pinned polymer, according to Lindeberg-Feller central limit theorem [117, 118], the corresponding random walk is a multi-variate Gaussian process. It can be

factorized into the product of three Gaussian processes, each corresponding to a coordinate axis. Let us first discuss it in the z direction, i.e. the direction along the force field. The propagator in the z direction $\rho(z_k = z|z_0 = 0)$ is Gaussian with the following mean and variance:

$$\begin{aligned}\langle z_k \rangle &= a \sum_{j=1}^k \langle \cos \theta_j \rangle, \\ \sigma_{0 \rightarrow k, z}^2 &= a^2 \sum_{j=1}^k \text{var} [\cos \theta_j].\end{aligned}\quad (3.38)$$

Finally, by imposing the Brownian bridge condition, the variance of bead position can be written as

$$\text{var}[z_k] = a^2 \frac{\sum_{j=0}^k \text{var} [\cos \theta_j] \sum_{j=L-k}^L \text{var} [\cos \theta_j]}{\sum_{j=0}^L \text{var} [\cos \theta_j]}. \quad (3.39)$$

The analytical results above are compared with the 3D Monte-Carlo simulations (see section 2.3). We can see in Fig. 3.8 that again an excellent agreement is obtained.

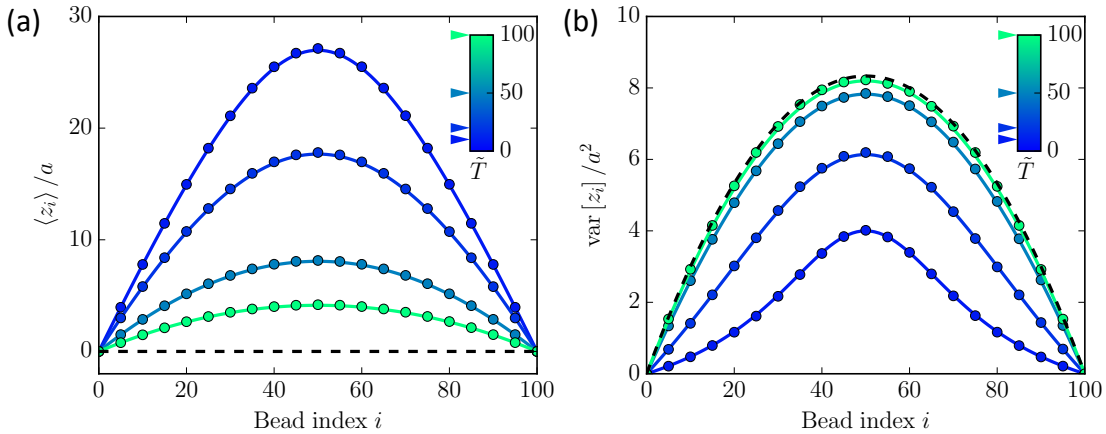


Fig. 3.8 Mean and variance of the bead position in the direction along the force field. Solid lines are theory and dots are Monte-Carlo simulation results. The black dash line indicates the case $\tilde{T} \rightarrow \infty$, i.e. no external force field.

Now let us discuss the directions perpendicular to the force direction. By symmetric reasons, we can immediately conclude that the statistics in x and y directions are identical. In addition, the mean position in both direction should be vanished because there is no bias. We can write as

$$\langle x_k \rangle = \langle y_k \rangle = 0. \quad (3.40)$$

On the other hand, using Eq. (3.37), the variance of x and y components of the j^{th} rod orientation can be written as

$$\text{var}[u_{j,x}] = \text{var}[u_{j,y}] = \langle u_{j,x}^2 \rangle - \langle u_{j,x} \rangle^2 = (1 - \langle \cos^2 \theta_j \rangle)/2 \quad (3.41)$$

Again, impose the Brownian bridge condition similar to Eq. (3.39), the variance of x and y components of the bead position can be obtained. Notice the variance in x and y directions are different from the variance in z direction. This is shown in Fig 3.9 together with the benchmark of our theory and the Monte-Carlo simulations.

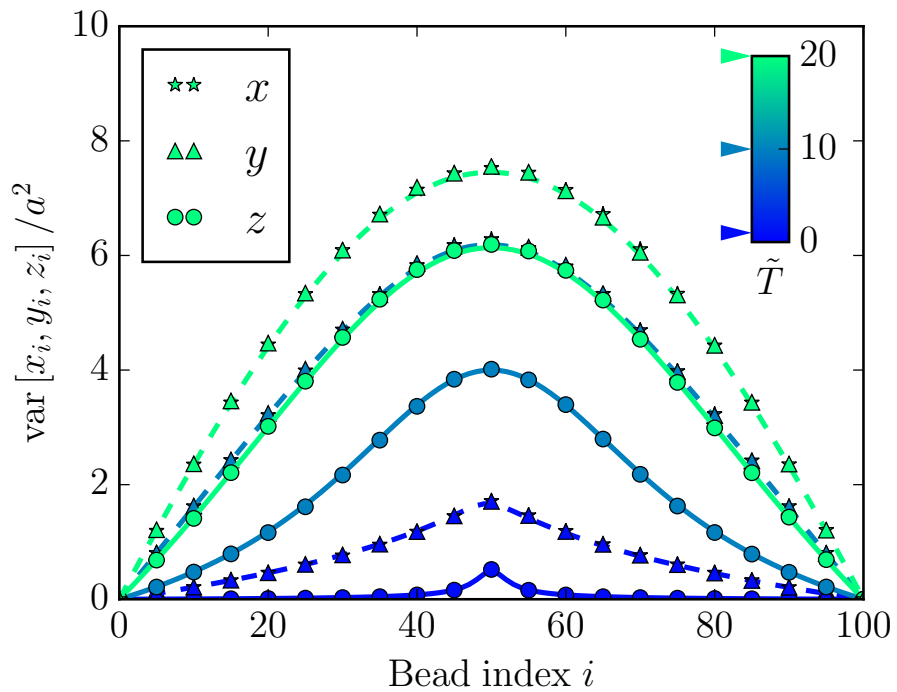


Fig. 3.9 Comparison of fluctuations in x , y and z directions. Symbols denote the Monte-Carlo simulations. Circles show the fluctuations along the z axis, whereas stars and triangles along x and y axis respectively. Colors correspond to different dimensionless temperatures. Solid and dashed lines are theoretical predictions for fluctuations along and orthogonal to the force field, respectively.

In this section, we discussed the three dimensional pinned polymer loop model and its equilibrium statistics. The mean and variance of each bead position are calculated using the grand canonical ensemble combined with Brownian bridge technique. After so many discussions about the model for chromosomes, in next section, we will come back to the biological problem. Using the insight from model analysis, we will discuss the paring problem of homologous.

3.4 Modeling the chromosome alignment

In fission yeast, the chromosomes are appearing in pairs during nuclear oscillation, which means there are two mechanically identical chromosomes. In total, there are three chromosome pairs in fission yeast. In this section, we will use the theory from the pinned polymer loop model to discuss the chromosome alignment problem in fission yeast. We will first discuss about the chromosome paring and alignment, and then fit our model to the biology.

3.4.1 Chromosome paring and alignment

In the prophase I of fission yeast, the dramatic chromosome movements are observed before the pair of chromosomes separate into two daughter cells. However, before the separation, the pair of chromosomes are supposed to align together in space. This process is called chromosome paring, which is the necessary condition for the correct segregation later.

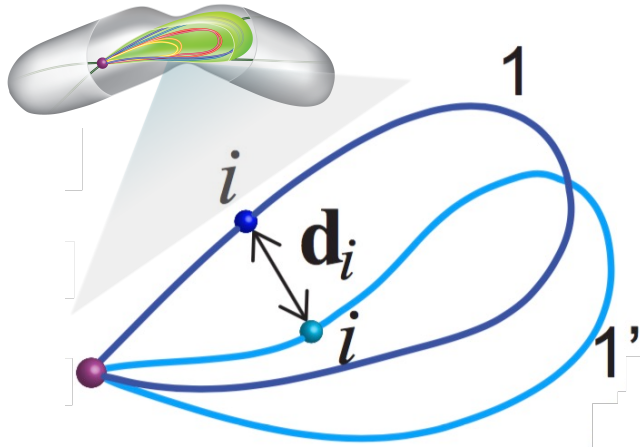


Fig. 3.10 A Pair of homologous chromosomes bound to the SPB. The distance of a pair of loci is illustrated as \mathbf{d}_i .

In the mean time of chromosome pairing, the nucleus of fission yeast is oscillating. As we discussed in Chapter 2, the oscillation can be divided into two pieces of steady motion, which can be further transferred to the scenario of pinned polymer loop in an external force field. One can intuitively imagine that the chromosomes will be more stretched when subjecting to an stronger external force field. So the statistical distance between two corresponding loci will be shorten. Biologically, if the statistical distance is smaller than 400 nm, then it is said been paired. It is interesting to ask how does the pulling facilitate the paring of homologous.

In next subsection, we will discuss how to apply our theory to get insights of the paring problem of chromosomes.

3.4.2 Theory fits to the biology

In order to fit our theory to the real biological problem, let us first discuss some related parameters which are listed in table 1.1 (Chapter 1). During cell division, chromosomes are highly condensed. As a consequence, the Kuhn length is large to be ~ 200 nm. With the length of chromosomes in base pair and the compact ratio listed in the same table, we can estimate that the total number of monomers in the longest chromosome is about 300. We will discuss the paring problem of the longest pair of chromosomes because the paring of shorter ones is easier comparing to the former.

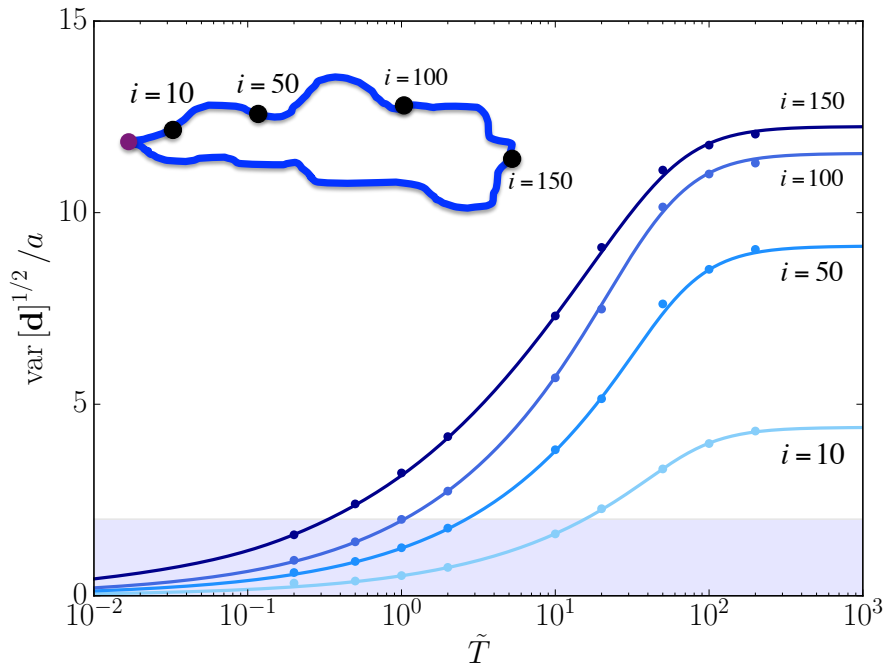


Fig. 3.11 The distance between corresponding loci of homologous pair varies with the dimensionless temperature. Different curve indicates different location along the chromosome. The shaded region denotes the separation below which the chromosomes are considered to be paired. Dots are BD simulation data and solid lines are results from our theory. Inset is a sketch of the observing loci along the chromosome. Parameters are shown in the context.

In the model, we measure the distance between two corresponding beads of the polymer pair, see in Fig. 3.10. These two beads correspond to the same loci of homologous. The paring process is supposed to bring them together with a statistical distance less than 400

nm. Then we ask the question that is the pulled movement offers an sufficient force for the pairing.

To answer this question, we measure how the statistical distance \mathbf{d} varies with the dimensionless temperature \tilde{T} . Notice that for a fixed thermal temperature T , a smaller dimensionless temperature means large external force F . Furthermore, this distance is measured at different location along the chromosome, see in the inset of Fig. 3.11. Given that the excluded volume effect is ignored, the three dimensional mean distance between two corresponding beads is zero. The statistical distance is defined as the square root of its variance and the variance is calculated as:

$$\text{var}[\mathbf{d}_i] = \text{var}[\mathbf{r}_i - \mathbf{r}'_i] = 2\text{var}[\mathbf{r}_i] = 2(\text{var}[x] + \text{var}[y] + \text{var}[z]) \quad (3.42)$$

We shown in Fig. 3.11 the results from our model. Now let us estimate the value of dimensionless temperature from the experimental facts. Using the Stokes relation $F = 6\pi\eta Rv$, the strength of external force field can be evaluated. η is the viscosity of nucleoplasm which is estimated by the experimentalist as 1000 times of water. R is the bead radius can be estimated as half of the Kuhn length $R \approx 100$ nm. The moving velocity $v \approx 2.5\mu\text{m}/\text{min}$ is measured from the experiment. As a result, we can obtain $F \approx 7 \times 10^{-14}$ N. Using the temperature $T = 300$ K and Kuhn length $a = 200$ nm, we can finally obtain $\tilde{T} \approx 0.3$. This is a parameter locates at the lower left strong force regime in Fig. 3.11. As we can see from the figure, the distance between corresponding beads is smaller and mostly below the paring threshold. So the conclusion is the pulling motion aligns chromosomes and supplies an sufficient force for the paring.

As mentioned in the first chapter, redistribution of dynein motors is the mechanism drives the nuclear oscillation. We now ask the question whether the number of involving motor molecules sufficient for the motion.

To answer this question, let us first estimate the total force needed for the pulling motion. According the genomic length of each chromosome together with a compaction ratio of 100 bp/nm and a Kuhn length of 200 nm, the total number of monomers in fission yeast is ~ 1260 . So the total pulling force is $F_{total} \approx 100$ pN. The stall force of dynein motors has been reported within the range of 1 – 7 pN [120, 121]. This corresponds to 14 – 100 dynein motors pulling together. Previous measurements shows that there are 50 – 100 dynein motors engaged in pulling of the SPB [122]. Thus the experimentally observed number of dynein motors is sufficient to generate a force for the alignment of the chromosomes.

3.4.3 Two intersecting Loops

In this subsection, let us consider an application of our theory, which is also possible to happen in the biological circumstance. In biology, the pairing process of homologous is often said to be analogy to the zipping process of a zipper [123]. Namely, segments near to the SPB are paired in prior. However, it is still possible that a pair of beads in the middle part of chromosome bond before those in between. This could be caused by the recombination process which involving several types of enzymes and double strand breaks. On the other hand, there is a hypothesis that the centromeres of homologous are still bond together during nuclear oscillation.

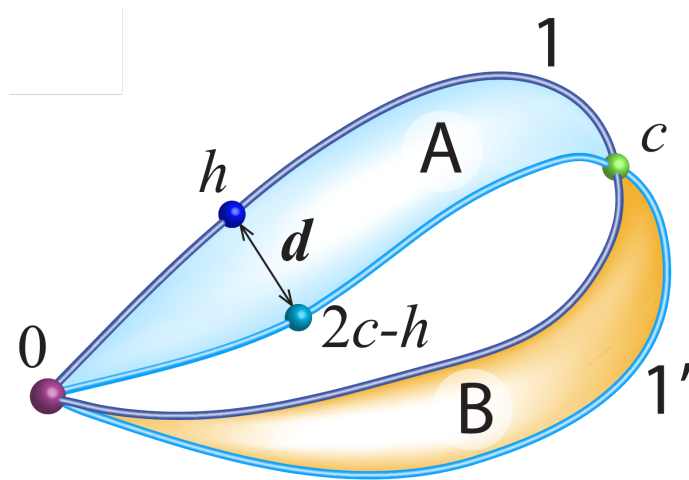


Fig. 3.12 The sketch of two intersecting loops 1 and $1'$ which are connected at one additional bead with index c . Shaded regions indicate the redefined loops A and B . The distance \mathbf{d} between two homologous beads h and $2c - h$ is illustrated.

To discuss this problem, we propose a scenario shown in Fig. 3.12. A pair of chromosomes (denoted by 1 and $1'$) is pinned at the SPB with an additional constraint at some intermediate bead position (indexed by c , where $0 < c < L$). However, bead c is not pinned so that it can still move around.

In order to solve this problem, we redefine the loops as shown in Fig. 3.12. The loop A starts at the pinned point, continues along the loop 1 , to the constraint point c and then returns to the origin along the loop $1'$ by the path of the same length. It is shown in Fig. 3.12 shaded with cyan color in between. The loop B is shown in Fig. 3.12 shaded with orange color in between. We are interested in the distance \mathbf{d} between two homologous beads as shown in the figure. Denote the first bead position with index h , then the other one can be denoted by $2c - h$ considering the loop A .

To calculate the PDF of $\mathbf{d} := \mathbf{r}_h - \mathbf{r}_{2c-h}$, which denote as $\rho(\mathbf{d})$, let us first calculate the joint positional PDF $\rho_{h,2c-h}(\mathbf{r}_1, \mathbf{r}_2)$. Denote the propagator as $\rho_{k \rightarrow j}(\mathbf{r}_1 | \mathbf{r}_2) = \rho(\mathbf{r}_k = \mathbf{r}_1 | \mathbf{r}_j = \mathbf{r}_2)$. Notice that the propagator is a (multi-variate) Gaussian function with a mean and variance summing up by path steps. Then we can apply the similar Brownian bridge condition, obtaining

$$\rho_{h,2c-h}(\mathbf{r}_1, \mathbf{r}_2) = \frac{\rho_{0 \rightarrow h}(\mathbf{r}_1 | 0) \rho_{h \rightarrow 2c-h}(\mathbf{r}_1 | \mathbf{r}_2) \rho_{0 \rightarrow 2c-h}(\mathbf{r}_2 | 0)}{\rho_{0 \rightarrow 2c}(0 | 0)}. \quad (3.43)$$

And then the PDF $\rho(\mathbf{d})$ can be calculated as

$$\rho(\mathbf{d}) = \int \int d\mathbf{r}_1 d\mathbf{r}_2 \delta(\mathbf{d} - (\mathbf{r}_1 - \mathbf{r}_2)) \rho_{h,2c-h}(\mathbf{r}_1, \mathbf{r}_2), \quad (3.44)$$

Without evaluate the integrals in Eq. (3.44), one can conclude $\rho(\mathbf{d})$ is Gaussian because $\rho_{h,2c-h}(\mathbf{r}_1, \mathbf{r}_2)$ is Gaussian. It is not difficult to obtain the mean distance is $\langle \mathbf{d} \rangle = \mathbf{0}$ because of no excluded volume effect. And the variance can calculate the same way as our previous procedure. For example, the z -component variance is

$$\text{var}[d_z] = 2 \frac{\sigma_{0 \rightarrow h,z}^2 \sigma_{h \rightarrow c,z}^2}{\sigma_{0 \rightarrow c,z}^2}, \quad (3.45)$$

where each variance is calculated according to Eq. (3.36). The result compare with simulations is shown in Fig. 3.13. We see that fluctuations of the distance is reduced with the additional constraint point compared with the unconstrained case.

In this section, we apply the theory of our model to the alignment problem of homologous in meiotic fission yeast. Despite the simplicity of our model, we still obtain quantitatively consistent results respecting to the biological facts. On the other hand, because of the simple model, we are able to tract it analytically. Fluctuations of distance between homologous beads are calculated analytically to quantify the paring process. The theoretical results are all verified by simulations. In addition, by discussing the case of two intersecting polymer loops, we find the additional constraint helps to reduce the fluctuations, thus facilitate the pairing process.

3.5 Summary

In this chapter, we discuss the equilibrium statistics of pined polymer loops in an external force field, which is our model for chromosomes in meiotic fission yeast.

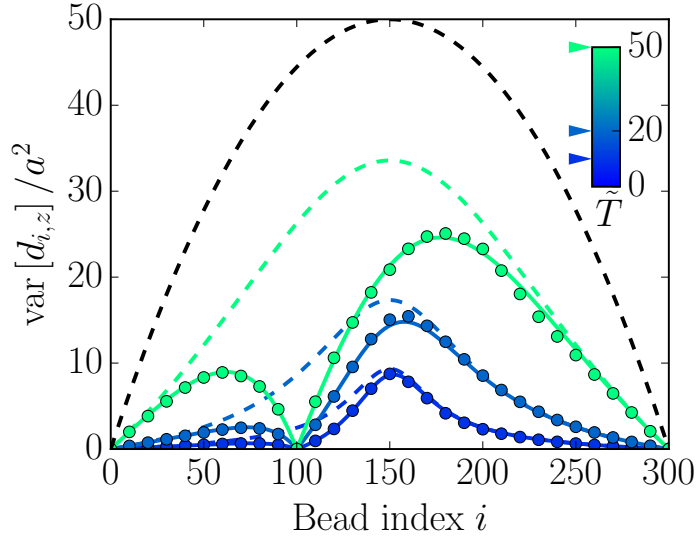


Fig. 3.13 Variance of the distance between homologous beads with additional constraint. The constraint is located at the bead with index $c = 100$. Circles denote the simulation results while the solid lines represent the theory. The dashed lines show the variance of the unconstrained case with different color indicates different dimensionless temperature. The black dashed line shows the limit of unconstrained force-free Brownian bridge.

We first solve the statistics in a idealized 1D model. We introduce a technique which combines the *Fermi-Dirac* statistics and Brownian Bridge condition to solve the problem in *grand canonical ensemble*. The solution found is compared to the exact solution, which can be obtain after utilize the analogy to a number partition problem. However, we found that the results from our technique are quite accurate and the exact solution is quite cumbersome for later calculations. Thus the first approach is preferred. Using the result, we are able to calculate the mean and variance of bead position.

And then we extend our theory to the three dimensional system. The same method of Brownian Bridge is used to solve the statistics. Also the three dimensional mean and variance of bead position is calculated.

In the last section, we use our theoretical results to discuss the real biological problem. The alignment of homologous chromosomes is discussed. Furthermore, we discussed the chromosome with possible additional intermediate constraint by applying our theory to the two intersecting loops case. We found both the pulling movement of chromosomes and the additional bonding between homologous facilitate the pairing and alignment of chromosomes.

Last but not least, we would like to mention that the work of this chapter was done by closing cooperation Dr. Yen-Ting Lin. Many of the credits is belong to him. We would like to give our special thank to him here.

In next chapter, we will delve deeper to study the non-equilibrium properties of the pinned polymer loop polymer in an external force field.

Chapter 4

Dynamical Properties of Pulled Polymer Loops

In previous chapter, the equilibrium statistics of pinned polymer loops in an external force field are discussed in details. However, we known that the nuclear oscillation in fission yeast is of course a non-equilibrium process. So we have to assume the relaxation time of the system is much smaller than the oscillation period to make our discussion reasonable. The assumption need to be justified. On the other hand, it is interesting to know the dynamical properties of pinned polymers in an external field from theoretical point of view. To the best of our knowledge, the way to calculate the relaxation time of a pinned bead-rod model is still missing.

In this chapter, we will study the dynamical properties of pinned polymer loop model representing the chromosomes in fission yeast. We will verify our assumption of short relaxation time used in previous chapter. Using the Rouse theory, we first study the pinned bead-spring polymer loop in an external force field. Then using the mapping from bead-rod polymer to the particle-lattice picture, we calculate the full dynamics of the 1D system. The Bethe-ansatz method is utilized to solve the dynamics. Excellent results is obtained and compared to the projection of 3D polymer results from BD simulations.

In the first section, we illustrate how to apply the Rouse theory on our pinned polymer loop model in an external filed. In the second section, we introduce the mapping from 1D polymer dynamics to the ASEP (Asymmetric Simple Exclusion Process). An brief background knowledge of ASEP is introduced. In the third section, we use the Bethe-ansatz method to solve the ASEP problem exactly and calculate the relaxation time analytically. In the force section, we try to apply our calculation to the 3D bead-rod model. Finally, a summary is given in the last section.

4.1 Rouse theory of the pinned bead-spring loop

Rouse theory is a theoretical framework to calculate the dynamics of a polymer. Comparing to other theory like the Zimm theory, it is simple and gives the full information of dynamics. In most cases, Rouse theory can apply only to the bead-spring model. This is one of the reason that the bead-spring model is more popular than the bead-rod model.

In the case of modeling chromosomes in fission yeast, we intend to use the bead-rod model instead of the bead-spring. This is mainly because the finite extensibility, which is important for condensed meiotic chromosomes, can be described easily by the bead-rod model. However, the study of Rouse theory is still useful because of several reasons. On one hand, we will see later that Rouse theory can correctly represent the zero external force limit of the bead-rod model. On the other hand, in realistic simulation that take into account many complex factors, it is not so important whether the bead-rod or bead-spring model is utilized. In this case, the simple rouse theory offers an theoretical calibration line for us to analyze the polymer system.

Despite the simplicity of the Rouse theory, we have not seen a calculation of the Rouse theory on the pinned polymer loop model. So what we present here is new. Let us start by writing down the dynamical equations of the model.

4.1.1 Dynamical equations

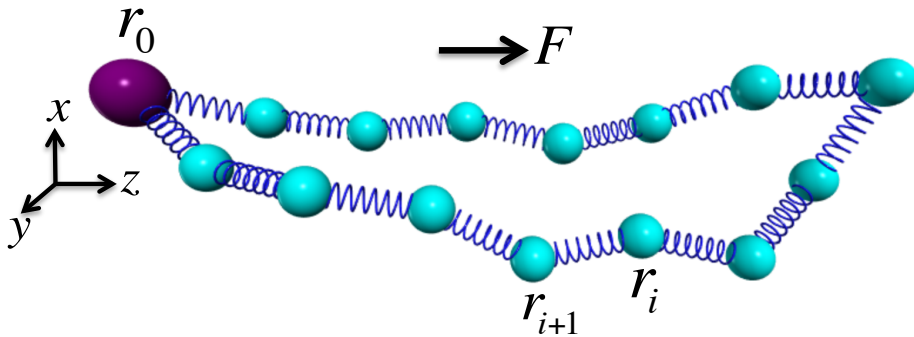


Fig. 4.1 The sketch of pinned bead-spring loop with notations.

Consider a pinned polymer loop modeled by beads and connecting springs, see in the sketch Fig. 4.1. As in our previous discussion of the bead-rod model, the bead labeled by 0 is assumed be pinned at the origin and there are L beads in total in the loop. Again the periodic indexing is used. We can write the pinned condition as $\mathbf{r}_0 = \mathbf{r}_L = \mathbf{0}$.

The dynamical equation for a single bead in the loop is Eq. (2.10). However, we rewrite it as following after considering the connecting structure:

$$\xi \frac{d\mathbf{r}_i}{dt} = -k_H \sum_k A_{ik} \mathbf{r}_k + \mathbf{f}_i^e + \mathbf{f}_i^b, \quad (4.1)$$

where ξ is the friction coefficient of bead in solution, \mathbf{r}_i is the bead position of the i th bead, k_H is the spring constant with a linear Hookean spring assumed. \mathbf{f}_i^e is the external force exerted on beads, \mathbf{f}_i^b is typical Brownian force satisfying Eq. (2.2). \mathbf{A} is the connecting matrix. It is not difficult to find that in the case of the setting above, i.e. pinned loop, \mathbf{A} is a $(L-1) \times (L-1)$ matrix and has the following form

$$\mathbf{A} = \begin{bmatrix} 2 & -1 & 0 & \cdots \\ -1 & 2 & -1 & \cdots \\ \vdots & \ddots & \ddots & \vdots \\ \cdots & -1 & 2 & -1 \\ \cdots & 0 & -1 & 2 \end{bmatrix}. \quad (4.2)$$

Notice that we do not take into account any complex terms of interaction such as bending stiffness and exclusive effect in this simple model. This is because analytical results are tractable in such a simple Rouse setting. The impact of these complex interaction terms will be studied numerically by BD simulation in next chapter.

4.1.2 The normal modes

For convenience, we use the vector notation and rewrite Eq. (4.1) as:

$$\xi \frac{d}{dt} \mathbf{R} = -k_H \mathbf{A} \mathbf{R} + \mathbf{F}^e + \mathbf{F}^b, \quad (4.3)$$

where $\mathbf{R} = [\mathbf{r}_1, \mathbf{r}_2, \dots, \mathbf{r}_{L-1}]^T$, and similar vector notation is also applied for $\mathbf{F}^e, \mathbf{F}^b$. In order to solve this set of dynamical equations, we first notice that the connecting matrix \mathbf{A} is a very special type of matrix called tridiagonal Toeplitz matrix [124]. Fortunately, it can be diagonalized exactly. To do this, let us introduce a similarity transfer that

$$[\Omega^{-1} \mathbf{A} \Omega]_{jk} = \mathbf{D}_{jk} = \lambda_k \delta_{jk}, \quad (4.4)$$

here Ω is normalized to be a unitary matrix, and λ_k is the eigenvalue of matrix \mathbf{A} . We skip the calculation details here and just give out the results as following

$$\lambda_k = 4 \sin^2 \left(\frac{k\pi}{2L} \right), k = 1, 2, \dots, L-1; \quad (4.5a)$$

$$\Omega_{jk} = \Omega_{kj} = [\Omega^{-1}]_{jk} = [\Omega^{-1}]_{kj} = \sqrt{\frac{2}{L}} \sin \left(\frac{jk\pi}{L} \right). \quad (4.5b)$$

Then we can multiply both sides of Eq. (4.3) by Ω^{-1} arrive at

$$\xi \frac{d(\Omega^{-1} \mathbf{R})}{dt} = -k_H \Omega^{-1} \mathbf{A} \Omega \Omega^{-1} \mathbf{R} + \Omega^{-1} \mathbf{F}^e + \Omega^{-1} \mathbf{F}^b. \quad (4.6)$$

Notice that $\Omega^{-1} \mathbf{A} \Omega = \mathbf{D}$ and use the notation such that $\tilde{\mathbf{R}} = \Omega^{-1} \mathbf{R}$, we get the set of decoupled dynamical equations

$$\xi \frac{d\tilde{\mathbf{r}}_j}{dt} = -k_H \lambda_j \tilde{\mathbf{r}}_j + \tilde{\mathbf{f}}_j^e + \tilde{\mathbf{f}}_j^b. \quad (4.7)$$

Eq. (4.7) can be solved easily by standard methods. The general solution can be written as following

$$\tilde{\mathbf{r}}_j(t) = \tilde{\mathbf{r}}_j(0) e^{-\frac{k_H \lambda_j}{\xi} t} + \frac{1}{\xi} \left(\int_0^t \tilde{\mathbf{f}}_j^e e^{-\frac{k_H \lambda_j}{\xi}(t-t')} dt' + \int_0^t \tilde{\mathbf{f}}_j^b e^{-\frac{k_H \lambda_j}{\xi}(t-t')} dt' \right). \quad (4.8)$$

Here the transformed Brownian force also fulfills

$$\langle \tilde{\mathbf{f}}_j^b \rangle = \mathbf{0}; \quad (4.9a)$$

$$\langle \tilde{f}_{i\alpha}^b(t) \tilde{f}_{j\beta}^b(t') \rangle = 2\xi k_B T \delta_{ij} \delta_{\alpha\beta} \delta(t-t'). \quad (4.9b)$$

Given the solution of Eq. (4.8), the position of each bead can be obtain by the inverse transformation $\mathbf{R} = \Omega \tilde{\mathbf{R}}$. In the simple case of constant external force field, $\mathbf{f}_j^e = f^e \mathbf{e}_z$, Eq. (4.8) can be rewritten as

$$\tilde{\mathbf{r}}_j(t) = \tilde{\mathbf{r}}_j(0) e^{-\frac{k_H \lambda_j}{\xi} t} + \frac{\tilde{f}^e \mathbf{e}_z}{k_H \lambda_j} \left(1 - e^{-\frac{k_H \lambda_j}{\xi} t} \right) + \frac{1}{\xi} \int_0^t \tilde{\mathbf{f}}_j^b e^{-\frac{k_H \lambda_j}{\xi}(t-t')} dt' \quad (4.10)$$

Finally, the bead position can be obtained by the inverse transformation:

$$\mathbf{r}_i(t) = \sum_j \Omega_{ij} \tilde{\mathbf{r}}_j(t) \quad (4.11)$$

Now the equilibrium statistics of the polymer, such as the mean and variance of the each bead position can be calculated easily. Plug Eq. (4.10) in Eq. (4.11) and let $t \rightarrow \infty$, we get

$$\langle \mathbf{r}_i^\infty \rangle = \sum_j \Omega_{ij} \frac{\tilde{f}^e \mathbf{e}_z}{k_H \lambda_j} = \frac{f^e \mathbf{e}_z}{2Lk_H} \sum_{k,j} \frac{\sin\left(\frac{ij\pi}{L}\right) \sin\left(\frac{jk\pi}{L}\right)}{\sin^2\left(\frac{j\pi}{2L}\right)}. \quad (4.12)$$

If $L \gg 1$, the summation of j can be approximated by the integral so we get

$$\langle \mathbf{r}_i^\infty \rangle = \frac{f^e \mathbf{e}_z}{k_H} \sum_{k=1}^{\frac{L+1}{2}} \frac{\sin\left(\frac{i(2k-1)\pi}{L}\right)}{(2k-1)\pi \sin^2\left(\frac{(2k-1)\pi}{2L}\right)}. \quad (4.13)$$

One can clearly see from Eq. (4.13) that $\langle \mathbf{r}_i \rangle = \langle \mathbf{r}_{L-i} \rangle$ as we expected. And the components of mean position perpendicular to the force field direction are vanished.

In order to calculate the variance of bead position, it is nontrivial to firstly calculate the two time correlation of normal coordinate position, as following

$$\begin{aligned} \langle \tilde{\mathbf{r}}_m(t) \tilde{\mathbf{r}}_n(t') \rangle &= \langle \tilde{\mathbf{r}}_m(0) \tilde{\mathbf{r}}_n(0) \rangle e^{-\frac{k_H \lambda_m}{\xi} t - \frac{k_H \lambda_m}{\xi} t'} \\ &\quad + \frac{(\tilde{f}^e)^2}{k_H^2 \lambda_m \lambda_n} \left(1 - e^{-\frac{k_H \lambda_m}{\xi} t} \right) \left(1 - e^{-\frac{k_H \lambda_n}{\xi} t'} \right) \\ &\quad + \frac{3k_B T}{k_H \lambda_m} e^{-\frac{k_H \lambda_m}{\xi} t} \delta_{mn}. \end{aligned} \quad (4.14)$$

Then the second moment of bead position can be calculated as:

$$\langle \mathbf{r}_i^2(t) \rangle = \sum_{m,n} \Omega_{im} \Omega_{in} \langle \tilde{\mathbf{r}}_m(t) \tilde{\mathbf{r}}_n(t) \rangle. \quad (4.15)$$

Finally, let $t \rightarrow \infty$, we get the equilibrium variance of bead position

$$\text{var}[\mathbf{r}_i^\infty] = \langle (\mathbf{r}_i^\infty)^2 \rangle - \langle (\mathbf{r}_i^\infty) \rangle^2 = \frac{3k_B T}{2Lk_H} \sum_{k=1}^{L-1} \left[\frac{\sin\left(\frac{ik\pi}{L}\right)}{\sin\left(\frac{k\pi}{2L}\right)} \right]^2 = \frac{3k_B T}{k_H L} i(L-i). \quad (4.16)$$

Notice that we also have the symmetry that $\text{var}[\mathbf{r}_i^\infty] = \text{var}[\mathbf{r}_{L-i}^\infty]$. Moreover, it is important to point out the variance does not depend on the external force. So the statistical distance between two beads will not change no matter the external force filed is strong or weak. This is essentially because infinite extensible Hookean springs are employed in this simple model.

4.1.3 Relaxation time

Besides the equilibrium statistics, dynamical properties are also tractable. Our my interested quantity is the relaxation time of the pinned polymer. In order to do that, let us calculate the autocorrelation function of diameter vector, defined as $\mathbf{r}_d = \mathbf{r}_{\frac{L}{2}} - \mathbf{r}_0 = \mathbf{r}_{\frac{L}{2}}$. We can obtain

$$\langle \mathbf{r}_d(t) \mathbf{r}_d(0) \rangle = \sum_{m,n} \Omega_{\frac{L}{2}m} \Omega_{\frac{L}{2}n} \langle \tilde{\mathbf{r}}_m(t) \tilde{\mathbf{r}}_n(0) \rangle. \quad (4.17)$$

From Eq. (4.14) we can readily get the relaxation time

$$\tau = \frac{\xi}{k_H \lambda_1} = \frac{\xi}{4k_H \sin(\pi/2L)}, \quad (4.18)$$

when L is large we can expand the sin term arriving at $\tau = \frac{\xi L^2}{k_H \pi^2}$, which coincides as the unpinned polymer chain. Like the variance of bead position, the relaxation time does not depend on the external force too.

4.1.4 Compare to the bead-rod model

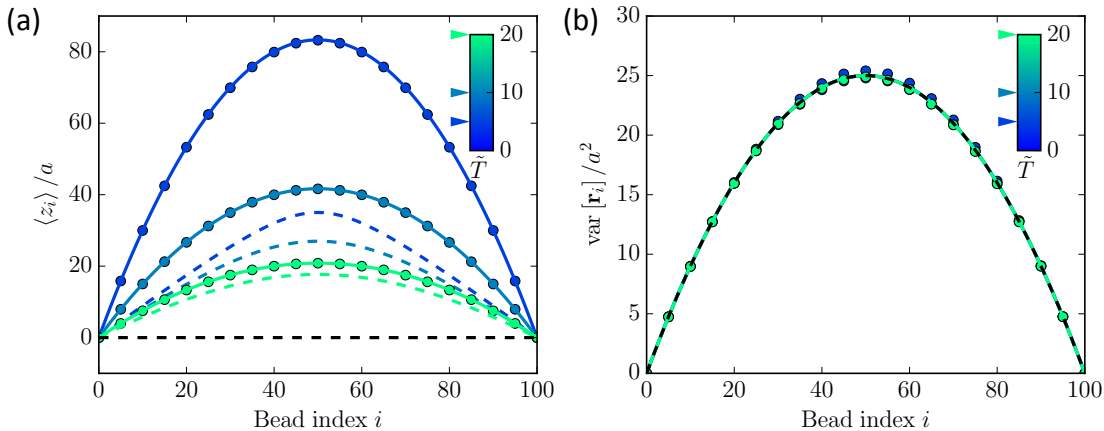


Fig. 4.2 The equilibrium mean and variance of bead position for the bead-spring model, compared with the bead-rod model. (a) Mean bead position of z component. (b) The variance of bead position. Dots are BD simulation results, solid lines are the Rouse theory for the bead-spring polymer loop, dash lines are the theory of the bead-rod model. Different color denotes different dimensionless temperature \tilde{T} which is indicated in the legend. The black dash line in both (a) and (b) shows the force free limit.

We would like to fit the Rouse theory to the bead-rod model if possible. To do this, we take the spring in the bead-spring model as entropic spring and then relate the spring constant

to the length of the rod. If the spring in the polymer is the three dimensional entropic spring, then the spring constant can be evaluated by the equipartition theorem as

$$\frac{1}{2}k_H a^2 = \frac{3}{2}k_B T, \quad (4.19)$$

where a can be interpreted as the equilibrium length of the spring and is set to the length of rod for the comparison. k_B is the Boltzmann constant. So we obtain $k_H = \frac{3k_B T}{a^2}$. Now we can plug it into Eq. (4.13) and Eq. (4.16) we arrive at

$$\langle \mathbf{r}_i^\infty \rangle = \frac{1}{3\tilde{T}} a \mathbf{e}_z \sum_{k=1}^{\frac{L+1}{2}} \frac{\sin\left(\frac{i(2k-1)\pi}{L}\right)}{(2k-1)\pi \sin^2\left(\frac{(2k-1)\pi}{2L}\right)}; \quad (4.20a)$$

$$\text{var}[\mathbf{r}_i^\infty] = a^2 \frac{i(L-i)}{L}. \quad (4.20b)$$

Recalled that $\tilde{T} = k_B T / \Delta E = k_B T / f^e a$. We can now compare the results with the equilibrium results obtained in previous chapter. See in Fig. 4.2. Notice that unlike the bead-rod model, the variance of bead position does not depend on the external force field. This is a fundamental difference between the bead-rod and bead-spring model.

For the relaxation time, plug Eq. (4.19) into the Eq. (4.18) and let $L \gg 1$, we obtain

$$\tau = \frac{\xi a^2 L^2}{3\pi^2 k_B T}. \quad (4.21)$$

Interestingly, it is coincide with the relaxation time of a free bead-spring polymer chain with L monomers. And again, it does not depend on the external force field.

In this section, we discussed the Rouse theory for pinned polymer loop in an external force field. Use the theory we calculate the equilibrium mean and variance of bead position and the relaxation time. The equilibrium results are compared to the results from the bead-rod model. We found the relaxation time of the bead-spring model does not depend on the external force field. Physically, it is caused by the infinite extensibility of the springs and not realistic. To explore to role of finite extensibility, in following sections, we will try to solve the relaxation time of the rigid bead-rod model. In next section, we will first introduce the mapping from the dynamics of pinned polymer loop to ASEP in 1D.

4.2 1D Pinned Bead-rod Loop Maps to ASEP

Like the same strategy used when we study the equilibrium statistics, we also begin with the simplest 1D model for the discussion of dynamics for the pinned bead-rod model. We have illustrated the mapping from one dimensional polymer loop to particles on lattice sites in previous chapter. Here, we will show that the same mapping can also be used to study the polymer dynamics. The dynamics of the bead-rod polymer can be mapped to the hopping process of the exclusive particles, which is called ASEP (Asymmetric Simple Exclusion Process). After the illustration of the mapping, we will go back to introduce some of the background knowledge about the ASEP. And then, some simulation results are shown to guide us to the solution of reflecting ASEP.

4.2.1 The mapping to ASEP

Recall that in the mapping from 1D bead-rod polymer to particle-lattice system, right oriented rods are interpreted as sites occupied by one particle, left oriented rods are interpreted as empty sites. L rods map to exactly L lattice sites, and reflecting boundaries are pertained. The number of particles must be exactly $L/2$ because of the looping condition.

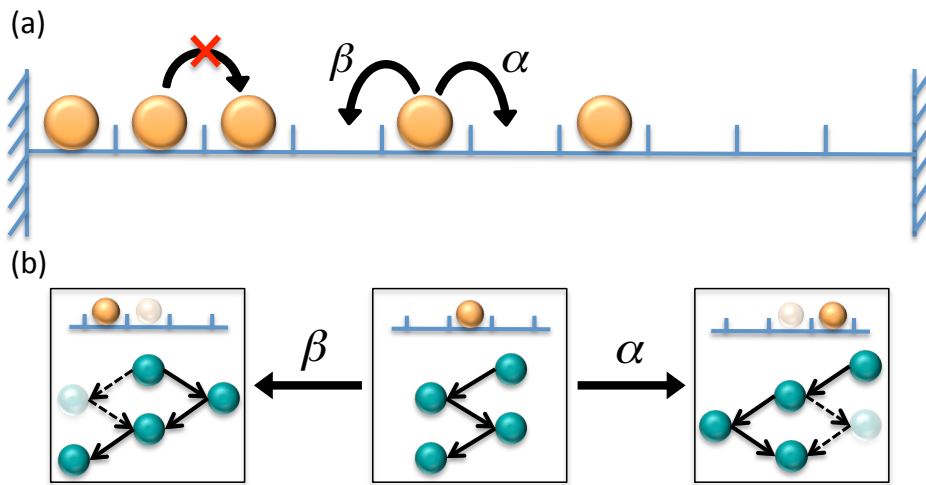


Fig. 4.3 The schematic of ASEP and the mapping of dynamics. (a) Illustration of ASEP, orange beads represent particle and reflecting boundary is indicated. (b) Illustration of one step particle hopping process maps to the flipping of two neighboring rods in the polymer picture.

Now, let us consider dynamics problem in the picture of particle-lattice. It is intuitive to imagine the particle can hop to the empty neighboring sites. Multiple occupation is forbidden

because the phase space is restricted to be binary. This kind of one dimensional particle hopping process is called Asymmetric Simple Exclusion Process (ASEP). Asymmetric means the hopping rate to left and right is not equal. And the reflecting boundaries can be imposed representing ASEP with reflecting boundary conditions. See in Fig. 4.3 (a) for a schematic of the ASEP. Now the question is what is the corresponding process in the polymer picture.

To answer this question, let us consider just one particle with its neighboring sites and take the example of the particle hops to the left site. The particle hops to the left affects the states of two neighboring sites and thus the states of two neighboring rods in the polymer picture. Correspondingly, the two rods orientation change from left-right to right-left. So one step of particle hopping corresponds to a flip of two neighboring rods in the polymer picture. The same analyse can be applied to the case of particle hops to right. See in the schematic Fig. 4.3 (b). And then our next question is how to determine the hopping rate to left and right.

Let us denote the rate of particle hopping to the right and to the left with α and β respectively. Then the detailed balance condition shows

$$\frac{\alpha}{\beta} = \frac{P_{l+1}}{P_l} = \exp\left(-\frac{\Delta E}{k_B T}\right), \quad (4.22)$$

where P_l, P_{l+1} is the probability of the configurations before and after the hopping, which also represents the probability of corresponding polymer configuration before and after change of rod orientation. ΔE is the energy required for the change of the rod orientation.

Here, we want to argue that $\Delta E = 2Fa$ for a one dimensional discrete model while $\Delta E = Fa$ for a continuous model. By continuous model we mean the 1D bead-spring model or the 3D polymer model where projected bead position can vary smoothly along the force direction. In this case, the change of orientation of the connectors only requires an average displacement of a along the force field direction. However, in the 1D discrete model, there is no such “displacement” except a discrete hopping of states, and the energy required for this hopping is calculated by the energy difference between the initial and final states.

On the other hand, the external force field only affects the bias of the hopping rate. The total hopping rate of a particle is determined by the effective temperature of the system, which is a constant independent of the external force. So let us discuss the total hopping rate in the case of no external force field.

To match the time scale of the particle hopping model to the polymer model, we identify that the average time for a particle to do a hopping should be the same as the average time for the changing of orientation of corresponding connectors. Since it is hard to estimate this time scale in the 1D discrete model, we assume it is the same as the continuous polymer model.

This is implied the facts that the time scale of 2D or 3D bead-rod model is correctly described by the Rouse theory in the case of no external force. For the continuous polymer model without external force field, changing orientation of two neighboring connectors requires the diffusion of the shared bead of an average distance a . We have

$$\alpha + \beta = r_{\text{total}} = \frac{1}{\tau_0}, \quad (4.23)$$

and τ_0 can be calculated as

$$\tau_0 = \frac{a^2}{2D} = \frac{\xi a^2}{2k_B T}, \quad (4.24)$$

where the diffusion constant $D = k_B T / \xi$ is used according to the Einstein relation. ξ is the friction coefficient of the bead monomer.

Combining Eq. (4.22) and Eq. (4.23) we can obtain

$$\alpha = \frac{r_{\text{total}} \exp(-\Delta E / k_B T)}{1 + \exp(-\Delta E / k_B T)}, \quad (4.25a)$$

$$\beta = \frac{r_{\text{total}}}{1 + \exp(-\Delta E / k_B T)}. \quad (4.25b)$$

With Eq. (4.25) and Eq. (4.24), we know have a well defined ASEP model with reflecting boundary conditions. And we are ready to delve deeper to solve the dynamics. But before that, let us first explain why do we solve the problem in this way.

Our goal is to solve the dynamics of the bead-rod polymer in an external force field. However, it is a difficult task as we have shown in previous section that the commonly used Rouse theory does not work. So we use the map from polymer to particle-lattice and define a corresponding ASEP model. The thing is ASEP is one of the fundamental models of non-equilibrium statistical physics with a wealth of tools to analyze it. For example, the Bethe-ansatz method is widely used to solve the model exactly. So our strategy is again to map our essential problem to a well known model and then solve the model and map it back to our original problem.

Although ASEP is a well studied non-equilibrium model, there are not so many works dealing with the particular case of reflecting boundary conditions. To the best of our knowledge, the exact solution of the full dynamics is still missing. In the next section, we will solve the problem use the Bethe-ansatz method. However, we would like to introduce a little bit the background of ASEP before doing that.

4.2.2 Brief introduction of ASEP

ASEP model is said to be a minimal non-equilibrium model similar to the Ising model in equilibrium statistical physics [125, 126]. Interestingly, it is first proposed for the study of a biological problem. In 1968, MacDonald et al. proposed a mathematical model for the kinetics of protein synthesis by ribosomes, which is essentially the ASEP model [6]. However, the name of ASEP is introduced later in 1970 by Spitzer with the aim of rigorously derive macroscopic hydrodynamic behavior from a microscopic model [127]. The task is done by Varadhan et al. on this specific simple model [128]. ASEP model has a lot of applications besides those mentioned above. Other examples ranging from the motion of motor molecules along the micro-tubes to the traffic systems [7, 129].

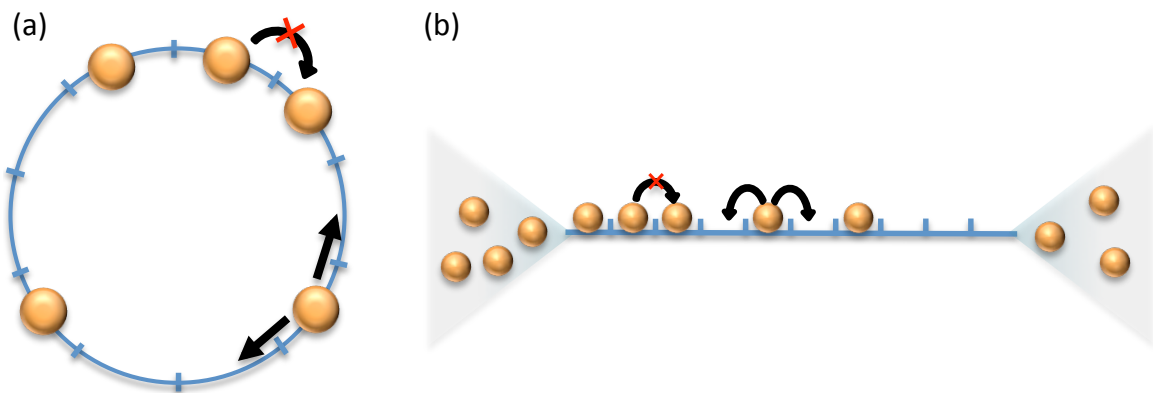


Fig. 4.4 Schematics of ASEP model. (a) ASEP with periodic condition. (b) ASEP with open boundary condition.

The simplest ASEP model is ASEP with periodic boundaries [126]. See a schematic in Fig. 4.4 (a). The stationary measure is simply a uniform distribution no matter the hopping rates have a bias or not. If there is a bias on the hopping rate, then a steady current will be induced in the stationary measure. This is one of the simplest example that detailed balance is not satisfied in the stationary state. The full dynamics of this case can be solved by the Bethe-ansatz method [130], we will discuss more about it later.

People are also interested in the case of ASEP on a infinite line from theoretical point of view [131, 132, 8]. For example, one can derive rigorously the diffusion of a tagged particle for the special case of equal hopping rate to both side.

$$\langle x^2 \rangle = 2 \frac{1-\rho}{\rho} \sqrt{\frac{t}{\pi}}, \quad (4.26)$$

where ρ is the density of particles. So we can see it is a sub-diffusion process as long as $\rho \neq 0$. This phenomenon is observed in the experiments [8].

ASEP with open boundaries is considered as the minimal microscopic model of transport [133, 126]. See in Fig. 4.4 (b). In this model, the two ends of the lattice is connected to two different reservoirs. So the rate of insertion and removal are different at the two ends. For instance, in the simplest case, particles can only be inserted at one end and removed at the other end. So a current can be induced by the bias hopping rates. In 1991, Krug et al. studied the ASEP with open boundaries and discovered the phase transitions in the model. Depending on the insertion or removal rates at the ends, the stationary state of the system can be in high density, low density or maximum current phase. And the phase transition can occur by adjusting those boundary conditions [134].

In order to solve the stationary state of the open ASEP, Derrida et al. proposed an approach which is now called Matrix Product Ansatz. It is a brilliant method far more useful than it though to be at the beginning. Interested readers can refer to the excellent review paper for more details [125]. There is a booming of researches on the topic of ASEP after the work of Derrida and his co-workers. A lot of people make significant contributions to the field. For example, in 1994, Schütz et al. investigate the reflecting ASEP use the $U_q(SU(2))$ quantum group [135]. The exact stationary solution was found but not the dynamics. De Gier found the exact solution of open ASEP with certain special constraints in 2005 [136]. Spohn et al. constructed an exact solution of the KPZ equation using the ASEP in 2010 [137].

Despite the simplicity of the ASEP model, the way to find the solution of general open ASEP system is still an open question [133, 126]. There are a lot of efforts working in this direction. Although the Matrix Product Ansatz is widely used in the study of the stationary state ASEP. The Bethe-ansatz method is more powerful when it comes to the dynamics. We will discuss more about it because we are going to use a generated version of this method to solve the reflecting ASEP in our problem. However, before go into the detailed calculations, let us first discuss some interesting numerical results, which also works as the hints for the searching of the exact solution.

4.2.3 Numerical results of the dynamics

We have already solved the equilibrium statistics of the 1D particle-lattice model in previous chapter. Thus the equilibrium statistics of the ASEP model is known. To solve the dynamics, we first use several numerical techniques to get some hints about what are the features of the non-stationary dynamics. Since the 1D reflecting ASEP is a well defined model, we can forget about the mapping to polymer system, do any kind of simulation as we want. We will discuss some of the details here.

For the dynamics of the system, our main interest is the relaxation time. Relaxation time characterizes how long the system returns to the stationary state when subjected to a perturbation. In the reflecting ASEP system, we measure the trajectory of a tagged particle, then calculate the auto-correlation function. Usually, we choose the particle in the middle. Denote the position of this particle as $x_{\frac{N}{2}}$, N is total number of particles in the system, the autocorrelation function can be written as

$$\left\langle x_{\frac{N}{2}}(t)x_{\frac{N}{2}}(0) \right\rangle \sim \sum_k \exp\left(-\frac{t}{\tau_k}\right). \quad (4.27)$$

In the long time regime, the largest τ_k dominates the relaxation. So the relaxation time is actually a short name of the longest relaxation time. By fitting the autocorrelation function in the long time regime, we can obtain the relaxation time numerically.

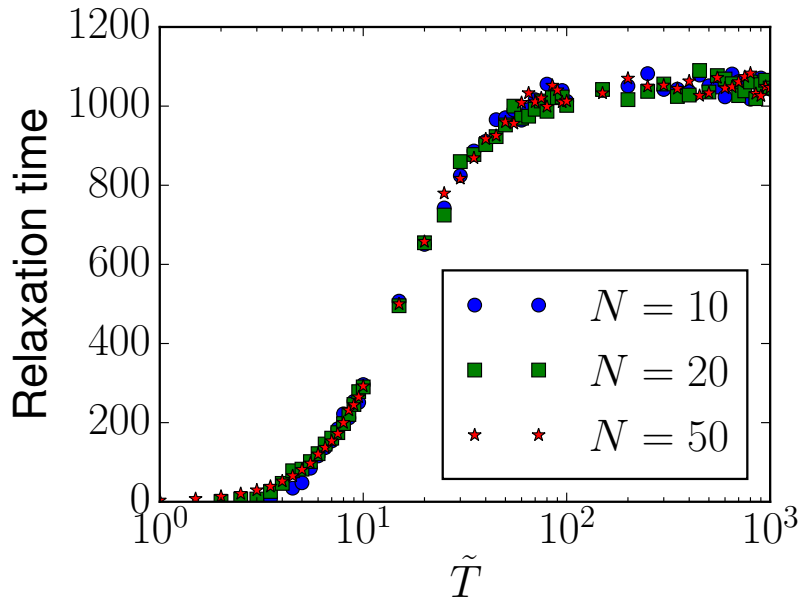


Fig. 4.5 The relaxation time of 1D reflecting ASEP system obtained from the Kinetic Monte Carlo simulation. Total number of lattice site is $L = 100$, different makers denote different total number of particles on the lattice. See more explanation in the main context.

In our simulation of 1D reflecting ASEP, we use the Kinetic Monte Carlo algorithm to simulate the particle hopping process. Details of this algorithm is shown in appendix ???. Then the autocorrelation function Eq. (4.27) is measured and fitted to extract the longest relaxation time. In Fig. 4.5, we show the relaxation time of a 1D reflecting ASEP model varies with the dimensionless temperature. Since the total hopping rate $\alpha + \beta$ is fixed and

dimensionless temperature is defined as

$$\tilde{T} = \frac{k_B T}{\Delta E} = -\frac{1}{\ln \frac{\alpha}{\beta}}. \quad (4.28)$$

Eq. (4.22) is utilized in the above equation. So the dimensionless temperature \tilde{T} can be interpreted as the degree of bias in the hopping model. Basically, a small \tilde{T} (which can be caused by a large external force or a low temperature) means a strong hopping bias and vice versa.

We show in Fig. 4.5 the simulation results of a system with total lattice sites $L = 100$ but different number of particles N on the lattice. A crucial point is hinted by the simulation results. That is the relaxation time of the system seems to be irrelevant with the number of total particles on the lattice (as long as it is neither all empty nor all occupied). This is something one would not expect. We can imagine the relaxation time of a system with N particles and $L - N$ particles should be the same because of the particle-hole symmetry. However, our simulation results suggest it is more than that. This observation will be explained later.

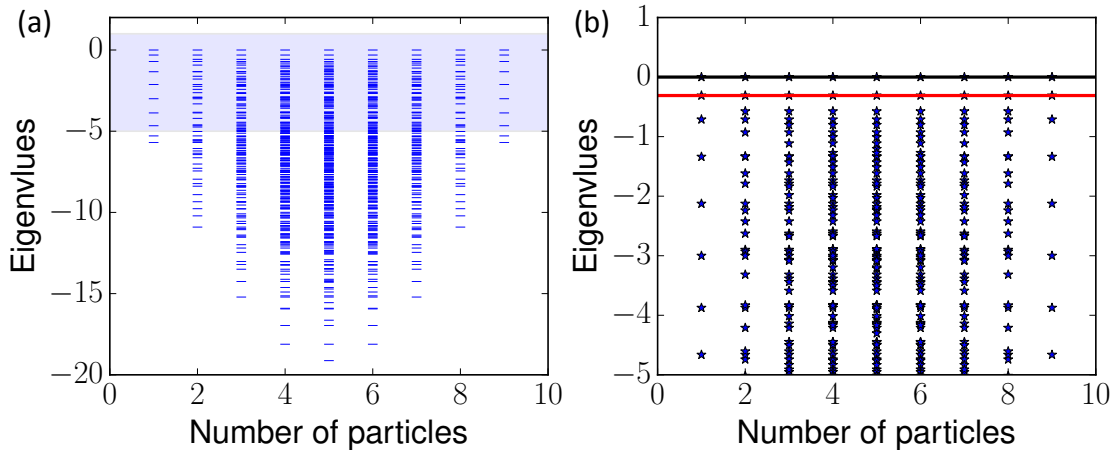


Fig. 4.6 Eigenvalues of a small 1D reflecting ASEP system with different number of particles on the lattice. $L = 10$ and the number of particle $N \in \{1, 2, \dots, 9\}$. (a) All eigenvalues, the eigenvalue is marked by bars. (b) Zoom in view for the shaded regime in (a), eigenvalues is marked by asters, the back line denotes the zero line and the red line shows that the largest non-zero eigenvalues are all the same. Parameters are set as $\alpha = 1$, $\beta = 2$.

For a discrete model such as ASEP, the dynamical information is encoded in the Markovian matrix of the master equation. By diagonalizing the matrix, we can obtain the full dynamical information in terms of eigenvalues and eigenvectors. For example, the stationary state corresponds to the eigenvector with eigenvalue equals to zero. And the longest

relaxation time of the system is related to the largest non-zero eigenvalue. Because for a stochastic system with stationary state, the eigenvalues of the Markovian matrix are always non-positive. And the longest relaxation time can be calculated as

$$\tau = -\frac{1}{\Lambda_1}, \quad (4.29)$$

where Λ_1 is the largest non-zero eigenvalue.

In Fig. 4.6, we use the brute force algorithm to diagonalize a small size system with $L = 10$ lattice sites and different number of total particles. There are several key remarks on these results.

- All eigenvalues are non-positive as expected.
- The eigenvalues satisfy the particle-hole symmetry, i.e. the eigenvalues for case of N particle and $L - N$ particles are exactly the same. This is well illustrated in Fig. 4.6 (a).
- By carefully examining Fig. 4.6 (a), we can find that the set of eigenvalue for case of $N = 1$ is a subset of the case $N = 2$. And in general, the set of eigenvalue for case N is contained in the set of eigenvalue of case $N +$ as long as $N < L/2$. This is also another interesting key feature of the reflecting ASEP system.
- As indicated by the red line in the zoom in Fig. 4.6 (b), we can see that the largest non-zero eigenvalue for all the cases are the same. This explains the observation shown in Fig. 4.5 in this special case. For the general case, we will explain after finding the exact solution in next section.

In this section, we introduce the mapping from polymer dynamics to the ASEP model with reflecting boundaries. Moreover, the history of ASEP model is introduced briefly. Furthermore, we discuss some interesting simulation results of the reflecting ASEP model. However, we just list some key inspiring simulation results here, and more will be discussed later together with the theoretical results. In next section, we will use the generalized Bethe-ansatz method to solve the reflecting ASEP model. With the exact solution, we map it back to understand the polymer dynamics. To the best of knowledge, the exact solution we will present is new and the way of generalization the Bethe-ansatz is novel. We will show it in details.

4.3 The Bethe-ansatz Solution of ASEP

In this section, we will use the generalized Bethe-ansatz method to solve the dynamics of the ASEP model with reflecting boundaries.

Bethe-ansatz is a method proposed by Hans Bethe in 1931 in order to solve the Heisenberg spin chain model with periodic condition [138]. At that time, he did not realize his great work opened a new branch of physics which is now called the integrability theory [130]. In 1963, Lieb-Liniger use the Bethe-ansatz method solved the Bose gas with δ interaction potential [139, 140]. Another important application of Bethe-ansatz is the six vertex model which is also solved by Lieb. The next big step was the discovery of the Yang-Baxter equation, which is introduced independently by C.N. Yang and Rodney Baxter [141, 142]. The Yang-Baxter equation provides a criteria to find out whether a model is integrable model or not [130]. The investigation of the Yang-Baxter equation led to the introduction of quantum group theory and the theory of topological knot invariants etc. During 1970s and 1980s, advanced Bethe-ansatz methods like functional Bethe-ansatz and algebraic Bethe-ansatz were developed [126]. After the introduction of the ASEP model, these Bethe-ansatz methods were quickly adopted to solve it because of the intrinsic connection from ASEP to a spin chain system. For example, the solution of periodic ASEP is almost identical to the Heisenberg spin chain with periodic condition [126]. The study of ASEP and Bethe-ansatz is still a very active field. There are a lot of references one can refer to [125, 143–145, 126].

The traditional Bethe-ansatz utilize the superposition of plane wave function as the trial solution. In our generalised method, we will show that the solution can be constructed by the combination of single particle eigenfunctions. And the single particle eigenfunction, which takes into account the boundary condition, can be more complex than the simple plane wave functions. So in order to construct the solution, let us first discuss the single particle solution.

4.3.1 Solution of single particle

The master equation of a single particle on a closed lattice with L sites can be written as:

$$\frac{d}{dt}P(x,t) = \alpha P(x-1,t) + \beta P(x+1,t) - (\alpha + \beta)P(x,t), \quad (4.30a)$$

$$\frac{d}{dt}P(1,t) = \beta P(2,t) - \alpha P(1,t), \quad (4.30b)$$

$$\frac{d}{dt}P(L,t) = \alpha P(L-1,t) - \beta P(L,t), \quad (4.30c)$$

where α and β is hopping rate of particle to left and right, respectively. See in the schematic Fig. 4.3 (a). $P(x,t)$ is the probability of a particle sitting on site x at time t , and x is confined to be the integer in the range of $x \in \{1, 2, \dots, L\}$. Eq. (4.30b) and (4.30c) are actually the special cases of master equation at the boundaries. It is much more convenient to rewrite Eq.

(4.30b) and (4.30c) as the following boundary conditions:

$$\alpha P(0, t) = \beta P(1, t), \quad (4.31a)$$

$$\alpha P(L, t) = \beta P(L + 1, t). \quad (4.31b)$$

The notation above might look confusing. Because $x = 0, L + 1$ are sites out of the domain and one would expect the corresponding $P(x, t) = 0$. However, this notation actually employs a technique called “ghost coordinate”, which is often used in the analysis of stochastic processes. To clarify the concept, we remark several points here:

- By writing down Eq. (4.31), we actually introduced an auxiliary space with infinite lattice sites where only the master equation Eq. (4.30a) is satisfied. So in the auxiliary space, $P(0, t)$ and $P(L + 1, t)$ are not necessarily vanished.
- Based on the auxiliary space, we then impose additional constraints. Eq. (4.31a) can be interpreted as the flux from site 0 going right to site 1 equals to the flux from site 1 going left to site 0. Similarly, the same interpretation can also be applied to Eq. (4.31b). So the boundary condition simply means the net flux at the boundaries are vanished. Namely, the reflecting boundary condition is imposed.
- Physically, the real PDF $P(x, t)$ is normalized in the domain $x \in \{1, 2, \dots, L\}$, and the probability outside the domain is zero.
- Mathematically, Eq. (4.31) can be derived simplicity by assuming Eq. (4.30a) is valid in the whole space and do a subtraction of Eq. (4.30a) to Eq. (4.30b) and Eq. (4.30a) to Eq. (4.30c), respectively.

Now, our governing equations are the master equation Eq. (4.30a) and boundary conditions Eq. (4.31). To solve these equations, let us take the ansatz of separation of variables $P(x, t) = \phi(x)e^{\lambda t}$ and plug into the master equation, obtaining

$$\beta\phi(x + 1) - (\alpha + \beta + \lambda)\phi(x) + \alpha\phi(x - 1) = 0. \quad (4.32)$$

Given that x is an integer number, Eq. (4.32) is essentially a set of liner difference equations. Substituting the ansatz of $P_x(t)$ into boundaries of Eq. (4.31), we obtain

$$\alpha\phi(0) = \beta\phi(1), \quad (4.33a)$$

$$\alpha\phi(L) = \beta\phi(L + 1). \quad (4.33b)$$

The standard method to find the solution is to take an ansatz $\phi(x) = Az^x$, where z is an arbitrary complex number. We arrive at the characteristic quadratic equation:

$$\beta z^2 - (\alpha + \beta + \lambda)z + \alpha = 0. \quad (4.34)$$

The two roots fulfill $z_+z_- = \frac{\alpha}{\beta}$. And the solution of (4.32) can be written as

$$\phi(x) = A_+z_+^x + A_-z_-^x \quad (4.35)$$

By applying the boundaries Eq. (4.33) to Eq. (4.35) we can find all the eigenvalues and corresponding eigenvectors. The results are summarised as following. The stationary eigenmode with zero eigenvalue is

$$\phi_s(x) = \text{const.} \left(\frac{\alpha}{\beta} \right)^x, \quad (4.36a)$$

$$\lambda_s = 0. \quad (4.36b)$$

There are $L - 1$ non-stationary eigenmodes and corresponding eigenvalues, which can be written as

$$\phi_k(x) = \text{const.} \left(\frac{\alpha}{\beta} \right)^{\frac{x}{2}} \left[\sin \left(\frac{k\pi}{L}x \right) - \sqrt{\frac{\beta}{\alpha}} \sin \left(\frac{k\pi}{L}(x-1) \right) \right], \quad (4.37a)$$

$$\lambda_k = -(\alpha + \beta) + 2\sqrt{\alpha\beta} \cos \left(\frac{k\pi}{L} \right); k = 1, 2, \dots, L-1. \quad (4.37b)$$

The eigenvalue $\lambda_s = 0$ and corresponding eigenvector represent the stationary mode $\phi_s(x)$. Define a scalar product between any two functions by

$$(\phi, \psi) = \sum_x \frac{\phi(x)\psi(x)}{\phi_s(x)} \quad (4.38)$$

Notice that definition Eq. (4.38) makes $\phi_s(x)$ identical to the stationary distribution $P^e(x)$, and remember here x is an integer. By properly choose the constant and when $L \rightarrow \infty$, one can check the orthogonality and completeness of the eigenfunctions.

$$\sum_{x=1}^L \phi_k(x)\phi_l(x) = \delta_{k,l}, \quad (4.39a)$$

$$\sum_{k=1}^L \phi_k(x)\phi_k(y) = \delta_{x,y}. \quad (4.39b)$$

So for an arbitrary initial distribution of $P(x, 0)$, we can always decompose it as

$$P(x, 0) = \sum_k c_k \phi_k(x), \quad (4.40)$$

where c_k can be calculated by

$$c_k = \sum_x \phi_k(x) P(x, 0). \quad (4.41)$$

Finally, the solution of single particle on reflecting lattice can be written as

$$P(x, t) = \sum_k \phi_k(x) e^{\lambda_k t} \sum_{x'} \phi_k(x') P(x', 0). \quad (4.42)$$

For the special case that $P(x, 0) = \delta_{x,y}$, solution (4.42) can be simplified to

$$P(x, t) = \sum_k \phi_k(x) \phi_k(y) e^{\lambda_k t} \quad (4.43)$$

With the complete solution of single particle, we can go further to systems of more than one particle. The idea is that the single particle solution works as building blocks for the N particle solutions. To start with that, we first illustrate the case $N = 2$ and the position of particles are denoted by x_1, x_2 with the constraint $x_1 < x_2$.

4.3.2 Solution of two particles

Denote $P(x_1, x_2; t)$ the probability of the two particles sitting at x_1 and x_2 respectively at time t . Firstly, we shall write down the master equation, which looks as following

$$\begin{aligned} \frac{dP(x_1, x_2; t)}{dt} = & \alpha P(x_1 - 1, x_2; t) + \beta P(x_1 + 1, x_2; t) \\ & + \alpha P(x_1, x_2 - 1; t) + \beta P(x_1, x_2 + 1; t) \\ & - 2(\alpha + \beta)P(x_1, x_2; t) \end{aligned} \quad (4.44)$$

We take the same eigenfunction expansion as for the single particle case:

$$P(x_1, x_2, t) = \sum_k \Psi_k(x_1, x_2) e^{\Lambda_k t} \quad (4.45)$$

Plug it into the master equation Eq. (4.44) we have

$$\begin{aligned}\Lambda\Psi(x_1, x_2) = & \alpha\Psi(x_1 - 1, x_2) + \beta\Psi(x_1 + 1, x_2) \\ & + \alpha\Psi(x_1, x_2 - 1) + \beta\Psi(x_1, x_2 + 1) \\ & - 2(\alpha + \beta)\Psi(x_1, x_2)\end{aligned}\quad (4.46)$$

And the reflecting boundaries write as

$$\alpha\Psi(0, x_2) = \beta\Psi(1, x_2) \quad (4.47a)$$

$$\alpha\Psi(x_1, L) = \beta\Psi(x_1, L + 1) \quad (4.47b)$$

For the case of more than one particle, we need to take into account the exclusion effect, i.e., one site can be occupied by at most one particle. This can be also written as a boundary condition as

$$\alpha\Psi(x, x) + \beta\Psi(x + 1, x + 1) = (\alpha + \beta)\Psi(x, x + 1) \quad (4.48)$$

Notice that the exclusive condition must hold for any x . The notation of $\Psi(x, x)$ may looks a little bit weird, but keep in mind that it is a boundary condition that denotes the limiting situation $x_1 = x_2$. And we can understand it in the same way of understanding the “ghost coordinate” in the single particle case. See in appendix ?? for a detailed derivation of Eq. (4.48).

Before delve into the Bethe Ansatz solution, let us release the fixed coefficients of eigenfunctions in Eq. (4.36) and Eq. (4.37), rewrite them as the following general form:

$$\psi_s(x) = A \left(\frac{\alpha}{\beta} \right)^x, \quad (4.49a)$$

$$\psi_{ns}(x) = \left(\frac{\alpha}{\beta} \right)^{\frac{x}{2}} (A_+ e^{ipx} + A_- e^{-ipx}), \quad (4.49b)$$

where ψ_s and ψ_{ns} represent stationary eigenfunction and non-stationary eigenfunctions respectively, A , A_+ , A_- are amplitude coefficients, p is the wave vector of excited eigenmodes. In case of single particle case above, these coefficients can be fixed by applying the boundary conditions Eq. (4.31). Here however, we will leave them free now and use the general form to construct the Bethe-ansatz solution. Boundary conditions will be imposed afterwards and all unfixed coefficients can be solved by then.

The idea to construct the N particle solution is inspired by the standard Coordinate Bethe Ansatz (CBA). However, instead of using the plain plane wave function as building blocks, we use the general form of single particle eigenfunctions with unfixed coefficients. The

example of ansatz for $\Psi(x_1, x_2)$ reads

$$\Psi(x_1, x_2) = \psi_1(x_1)\psi_2(x_2) + \tilde{\psi}_2(x_1)\tilde{\psi}_1(x_2). \quad (4.50)$$

Here $\psi_n(x)$ and $\tilde{\psi}_n(x)$ are functions drawn from Eq. (4.49), either stationary Eq. (4.49a) or non-stationary Eq. (4.49b). There are two particles in the system thus we have the index n in the range of $n = 1, 2$. We classify $\psi_1, \tilde{\psi}_1$ as one class and $\psi_2, \tilde{\psi}_2$ as the other class. Functions in the same class (e.g. ψ_1 and $\tilde{\psi}_1$) share the same wave vector ($p_1 = \tilde{p}_1$), but different amplitude coefficients ($A_{1\pm} \neq \tilde{A}_{1\pm}$). If this class is drawn from the stationary mode Eq. (4.49a), then simply the functions in the class (ψ_1 and $\tilde{\psi}_1$) are only differentiated by amplitude coefficient ($A_1 \neq \tilde{A}_1$). It is important that ψ_n and $\tilde{\psi}_n$ have different amplitude coefficients. The main idea is to tune these amplitude coefficients so that $\Psi(x_1, x_2)$ satisfies the reflecting boundaries Eq. (4.47) and exclusive condition Eq. (4.48).

With the constructed ansatz Eq. (4.50), our remaining task is to impose the constraints Eq. (4.47) and Eq. (F.4) and fix those amplitude coefficients as well as the wave vectors. There are three types of $\Psi(x_1, x_2)$ depending on the combination of the two constructed classes: both stationary, both non-stationary and the mixed type with one stationary and the other non-stationary. In the following subsections, we will discuss these cases separately.

Both stationary

Let us first check the case that $\Psi(x_1, x_2)$ are constructed all by stationary eigenmodes. Namely $\psi_1(x) = A_1 \left(\frac{\alpha}{\beta}\right)^x$, $\psi_2(x) = A_2 \left(\frac{\alpha}{\beta}\right)^x$, $\tilde{\psi}_1(x) = \tilde{A}_1 \left(\frac{\alpha}{\beta}\right)^x$, $\tilde{\psi}_2(x) = \tilde{A}_2 \left(\frac{\alpha}{\beta}\right)^x$. Plug in to (4.50) we obtain

$$P^e(x_1, x_2) = \Psi(x_1, x_2) = A \left(\frac{\alpha}{\beta}\right)^{x_1+x_2}, \quad (4.51)$$

where $A = A_1 \tilde{A}_1 + A_2 \tilde{A}_2$. One can readily check that Eq. (4.51) is exactly the stationary eigenfunction of the two particle system as expected. First, we can easily obtain the corresponding eigenvalue is $\Lambda_s = 0$ by simply plug it in to Eq. (4.46). And then one can check the reflecting boundaries Eq. (4.47) and the exclusive condition Eq. (4.48) are both fulfilled.

The prefactor A can be fixed by normalization. However, it is not a trivial work because of the constraint $x_1 < x_2$. We will discuss in detail in the general case of N particles later.

Mixed non-stationary

The mixed type is a non-stationary eigenmode. Without loss of generality, we choose $\{\psi_1(x), \tilde{\psi}_1(x)\}$ to be the stationary class characterized by Eq. (4.49a), then $\Psi(x_1, x_2)$ can be

written as

$$\begin{aligned}\Psi(x_1, x_2) = & A_1 \left(\frac{\alpha}{\beta} \right)^{x_1} \left(\frac{\alpha}{\beta} \right)^{\frac{x_2}{2}} (A_{2+} e^{ip_2 x_2} + A_{2-} e^{-ip_2 x_2}) \\ & + \tilde{A}_1 \left(\frac{\alpha}{\beta} \right)^{x_2} \left(\frac{\alpha}{\beta} \right)^{\frac{x_1}{2}} (\tilde{A}_{2+} e^{ip_2 x_1} + \tilde{A}_{2-} e^{-ip_2 x_1}).\end{aligned}\quad (4.52)$$

Plug Eq. (4.52) in to the master equation, we will find the corresponding eigenvalue. Plug it in to the reflecting boundaries and exclusive condition, A_1 , \tilde{A}_1 , $A_{2\pm}$ and $\tilde{A}_{2\pm}$ can be tuned to fulfill these conditions. Consistency condition will give us the Bethe equation about wave vector p_2 , we will show the details of this procedure in the following text.

We first insert the solution to the master equation Eq. (4.46), obtaining the corresponding eigenvalue:

$$\Lambda = -(\alpha + \beta) + 2\sqrt{\alpha\beta} \cos(p_2), \quad (4.53)$$

p_2 is the wave vector that will be determined later. Accordingly, the reflecting condition Eq. (4.47) gives us

$$\frac{A_{2+}}{A_{2-}} = -\frac{(\alpha - \sqrt{\alpha\beta}e^{-ip_2})e^{-ip_2 L}}{(\alpha - \sqrt{\alpha\beta}e^{ip_2})e^{ip_2 L}}, \quad (4.54a)$$

$$\frac{\tilde{A}_{2+}}{\tilde{A}_{2-}} = -\frac{\alpha - \sqrt{\alpha\beta}e^{-ip_2}}{\alpha - \sqrt{\alpha\beta}e^{ip_2}}. \quad (4.54b)$$

We now check the exclusive condition Eq. (4.48). Simply substitute Eq. (4.52) into the condition. In order to fulfill the exclusive condition, we find that

$$\frac{A_1 A_{2+}}{\tilde{A}_1 \tilde{A}_{2+}} = -\frac{\alpha e^{ip_2} - (\alpha + \beta)\sqrt{\frac{\alpha}{\beta}} + \sqrt{\alpha\beta}}{\alpha e^{ip_2} - (\alpha + \beta)e^{ip_2} + \sqrt{\alpha\beta}}, \quad (4.55a)$$

$$\frac{A_1 A_{2-}}{\tilde{A}_1 \tilde{A}_{2-}} = -\frac{\alpha e^{-ip_2} - (\alpha + \beta)\sqrt{\frac{\alpha}{\beta}} + \sqrt{\alpha\beta}}{\alpha e^{-ip_2} - (\alpha + \beta)e^{-ip_2} + \sqrt{\alpha\beta}}. \quad (4.55b)$$

Finally, use the consistency condition that

$$\frac{\tilde{A}_{2+} A_{2-}}{\tilde{A}_{2-} A_{2+}} = \frac{\tilde{A}_1 \tilde{A}_{2+}}{A_1 A_{2+}} \frac{A_1 A_{2-}}{\tilde{A}_1 \tilde{A}_{2-}}. \quad (4.56)$$

We obtain the Bethe equation

$$e^{i2p_2 L} = 1. \quad (4.57)$$

Solve the equation we get $p_2 = \frac{k\pi}{L}$. Notice that it is exactly the same as the spectrum of single particle case. With the solution of p_2 we can re-substitute it into Eq. (4.54) and Eq. (4.55) to get the corresponding eigenfunctions. The results of this type of non-stationary eigenvalues and corresponding eigenfunctions are summarized as following

$$\Lambda_k = -(\alpha + \beta) + 2\sqrt{\alpha\beta} \cos\left(\frac{k\pi}{L}\right), \quad k = 1, 2, \dots, L-1; \quad (4.58a)$$

$$\Psi_k(x_1, x_2) = A \left[\frac{\alpha}{\beta} \left(\frac{\alpha}{\beta} \right)^{x_1} \phi_k(x_2) + \left(\frac{\alpha}{\beta} \right)^{x_2} \phi_k(x_1) \right]. \quad (4.58b)$$

Here $\phi_k(x)$ is exactly single particle non-stationary eigenfunction and A is a constant normalization coefficient.

Both non-stationary

We now turn to non-stationary eigenmodes constructed by both non-stationary class of single particle modes. Notice that, the number of remaining unknown eigenfunctions and eigenvalues is in principle $L(L-1)/2 - L$. We will show that there are all contained in this class. Let us first write down the Ansatz:

$$\begin{aligned} \Psi(x_1, x_2) = & \left(\frac{\alpha}{\beta} \right)^{\frac{x_1+x_2}{2}} \left[(A_{1+} e^{ip_1 x_1} + A_{1-} e^{-ip_1 x_1}) (A_{2+} e^{ip_2 x_2} + A_{2-} e^{-ip_2 x_2}) \right. \\ & \left. + (\tilde{A}_{1+} e^{ip_1 x_2} + \tilde{A}_{1-} e^{-ip_1 x_2}) (\tilde{A}_{2+} e^{ip_2 x_1} + \tilde{A}_{2-} e^{-ip_2 x_1}) \right]. \end{aligned} \quad (4.59)$$

Plug it in to the master equation, we get the corresponding eigenvalues

$$\Lambda = \sum_{n=1}^2 \left[-(\alpha + \beta) + 2\sqrt{\alpha\beta} \cos(p_n) \right]. \quad (4.60)$$

And plug it in to the reflecting boundaries, we obtain

$$\frac{A_{1+}}{A_{1-}} = -\frac{\alpha - \sqrt{\alpha\beta}e^{-ip_1}}{\alpha - \sqrt{\alpha\beta}e^{ip_1}}; \quad (4.61a)$$

$$\frac{\tilde{A}_{1+}}{\tilde{A}_{1-}} = -\frac{(\alpha - \sqrt{\alpha\beta}e^{-ip_1})e^{-ip_1L}}{(\alpha - \sqrt{\alpha\beta}e^{ip_1})e^{ip_1L}}; \quad (4.61b)$$

$$\frac{\tilde{A}_{2+}}{\tilde{A}_{2-}} = -\frac{\alpha - \sqrt{\alpha\beta}e^{-ip_2}}{\alpha - \sqrt{\alpha\beta}e^{ip_2}}; \quad (4.61c)$$

$$\frac{A_{2+}}{A_{2-}} = -\frac{(\alpha - \sqrt{\alpha\beta}e^{-ip_2})e^{-ip_2L}}{(\alpha - \sqrt{\alpha\beta}e^{ip_2})e^{ip_2L}}. \quad (4.61d)$$

To ease the notation, let us define the function $a(p, p') = \sqrt{\alpha\beta}e^{i(p+p')} - (\alpha + \beta)e^{ip} + \sqrt{\alpha\beta}$. Then the exclusive condition gives

$$\frac{A_{1+}A_{2+}}{\tilde{A}_{1+}\tilde{A}_{2+}} = -\frac{a(p_1, p_2)}{a(p_2, p_1)}; \quad (4.62a)$$

$$\frac{A_{1+}A_{2-}}{\tilde{A}_{1+}\tilde{A}_{2-}} = -\frac{a(p_1, -p_2)}{a(-p_2, p_1)}; \quad (4.62b)$$

$$\frac{A_{1-}A_{2+}}{\tilde{A}_{1-}\tilde{A}_{2+}} = -\frac{a(-p_1, p_2)}{a(p_2, -p_1)}; \quad (4.62c)$$

$$\frac{A_{1-}A_{2-}}{\tilde{A}_{1-}\tilde{A}_{2-}} = -\frac{a(-p_1, -p_2)}{a(-p_2, -p_1)}. \quad (4.62d)$$

The similar consistency condition of Eq. (4.56) gives the following Bethe equation:

$$e^{i2p_1L} = \frac{a(p_1, p_2)}{a(p_2, p_1)} \frac{a(p_2, -p_1)}{a(-p_1, p_2)}; \quad (4.63a)$$

$$e^{i2p_2L} = \frac{a(p_2, p_1)}{a(p_1, p_2)} \frac{a(p_1, -p_2)}{a(-p_2, p_1)}. \quad (4.63b)$$

Now it would be interesting to interpret the Bethe Equation and compare with the well known Bethe Equation of periodic boundary case. And we will show later this interpretation is useful to derive N particles Bethe Equation. We can consider Eq. (4.54) as a reflector that reflects the particle and change the direction of wave vector, i.e., $p_n \leftrightarrow -p_n$. On the other hand, Eq. (4.55) can be interpreted as a permutator that permutes two neighboring particles $n \leftrightarrow (n + 1)$. Let us say particle 1 starts from the left side of the lattice and then permutes with all the particle at right side until reaches the right boundary (of course in case of two

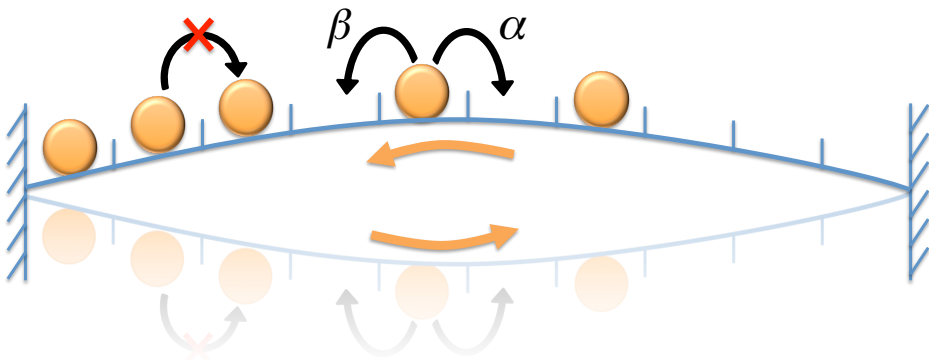


Fig. 4.7 The interpretation for the Bethe Equations of the reflecting ASEP as if it is a periodic ASEP system.

particles, there are only one particle at the right side), and then reflects by the boundary, become a particle traveling in the opposite direction, and then permutes with all the left side particles until reaches the left side boundary, and then reflects again, which recovers the initial state. A schematic of this process is shown in Fig. 4.7. In this sense, the particle works as if it is on a lattice with periodic boundary. Use this interpretation and the well known result of periodic Bethe Equation, one can easily recover exactly Eq. (4.63).

By solving the Bethe equation, one can get p_1 and p_2 and thus all amplitude coefficients up to a constant normalization factor. Then Eq. (4.60) gives the eigenvalues and Eq. (4.59) gives the eigenfunctions.

Unfortunately, it might not be possible to solve the Bethe equation analytically. So we resort to numerical solutions. We have verified the resulting eigenvalues and eigenfunctions by benchmark with the results from brute force diagonalizing of the transition matrix for small system size $L \leq 10$. Notice that those roots that $p_n = 0$ or $p_n = \pi$ have to be filtered out because they correspond to the first type of non-stationary eigenmodes which is not compatible by Eq. (4.59)

To summarize, the complete solution of two particle hopping system with reflecting boundaries was found. The solution is shown in the form of eigenfunction expansion, i.e. Eq. (4.46). The stationary eigenfunction with eigenvalue $\Lambda_0 = 0$ is listed as Eq. (4.51), while the two types of non-stationary eigenvalues and corresponding eigenfunctions are listed in Eq. (4.53), (4.60) and Eq. (4.52), (4.59), respectively. They can be fully determined by solving the Bethe Equation Eq. (4.57) and Eq. (4.63). Part of them are analytically shown in Eq. (4.58).

Finally, there are several remarks we want to make here. Firstly, as one can see from Eq. (4.58) that the eigenvalues of two particle system always contain the eigenvalues of single particle system. We will show later this can be generalised that the eigenvalues of $N + 1$

particle system always contain the eigenvalues of N particle system for $N < L/2$. Secondly, the relaxation time of the system is related to the largest non-zero eigenvalue Λ_1 . Eq. (4.58) hints $\Lambda_1 = -(\alpha + \beta) + 2\sqrt{\alpha\beta} \cos\left(\frac{\pi}{L}\right)$. However, since there is no analytical solution for eigenvalues of the second kind, it will be difficult to rigorously prove that. Numerical evidences will be provided to verify this is indeed true.

In next subsection, we will generalise the solution to the N particles system. It is actually quite straight forward after we have done the two particles case.

4.3.3 Solution of General N particles

Now we consider the system with N particles. Notice that, $N = L/2$ has to be set considering the mapping to polymer loop. However, our method of finding solution works for arbitrary N . As before, we first write down the master equation of a N particles system.

$$\frac{dP(x_1, \dots, x_N; t)}{dt} = \sum_{j=1}^N [\alpha P(\dots, x_j - 1, \dots; t) + \beta P(\dots, x_j + 1, \dots; t) - (\alpha + \beta)P(\dots, x_j, \dots; t)] \quad (4.64)$$

Similarly, after the eigenfunction expansion the reflecting boundaries write as

$$\alpha\Psi(0, x_2, \dots, x_N) = \beta\Psi(1, x_2, \dots, x_N) \quad (4.65a)$$

$$\alpha\Psi(x_1, \dots, x_{N-1}, L) = \beta\Psi(x_1, \dots, x_{N-1}, L+1) \quad (4.65b)$$

The exclusive condition for N particles case is more tricky. In principle, one has to consider to the case of three body collision and four body collision and so on. Luckily, in the simple model of ASEP, one can prove that these more than two body exclusive conditions are not new but just linear recombination of two body exclusive condition. So we can write the exclusive condition of a N particles system as

$$\alpha\Psi(\dots, x, x, \dots) + \beta\Psi(\dots, x+1, x+1, \dots) = (\alpha + \beta)\Psi(\dots, x, x+1, \dots) \quad (4.66)$$

The reason that the exclusive condition can be written in such a simple way is rooting from the Yang-Baxter Equation, which encodes the integrability of the ASEP system.

Stationary mode

Intuitively, we construct the N particles stationary solution as

$$P^e(x_1, x_2, \dots, x_N) = \Psi(x_1, x_2, \dots, x_N) = A \prod_{j=1}^N \left(\frac{\alpha}{\beta} \right)^{x_j}. \quad (4.67)$$

One can plug in the master equation check that the corresponding eigenvalue $\Lambda_s = 0$, and also verify the exclusive condition as well as the reflecting boundaries are fulfilled by insert the solution in to Eq. (4.66) and Eq. (4.65) separately.

We now try to fix the parameter A by normalization. Let us denote $q := \frac{\alpha}{\beta}$, then we can write A as following

$$A^{-1} = \sum_{\Omega} q^{\sum_j x_j} = \sum_{x_1 < x_2 < \dots < x_N} q^{\sum_j x_j}. \quad (4.68)$$

Let us do a variable change so that

$$E = \sum_j x_j - E_0,$$

where $E_0 = 1 + 2 + \dots + N = N(N+1)/2$. It is easy to see that E is a integer in the range of $0, 1, \dots, N(L-N)$. So Eq. (4.68) can be rewrite as

$$A^{-1} = q^{E_0} \sum_{E=0}^{N(L-N)} g(E) q^E, \quad (4.69)$$

where $g(E)$ is the number of partitions of positive integer E to N parts with each of size at most $L-N$. From the number partition theory, we identify

$$\sum_{E=0}^{N(L-N)} g(E) q^E = \binom{L}{N}_q = \frac{[L]_q!}{[L-N]_q! [N]_q!}, \quad (4.70)$$

where $[N]_q = 1 + q + q^2 + \dots + q^{N-1}$ is called a q number, and Eq. (4.70) is called the q binomial coefficient [119]. So we finally arrive at

$$P^e(x_1, x_2, \dots, x_N) = q^{-\frac{N(N+1)}{2}} \binom{L}{N}_q^{-1} \prod_{j=1}^N q^{x_j}. \quad (4.71)$$

The above equation is exactly the same as the Eq. (3.28) in previous chapter, where a different approach is used to reach it. Also, in [135], G. M. Schütz use a quantum group formalism obtained the same result with a different notation. We emphasize here that our method is

much more easily to understand and no prerequisite knowledge of quantum mechanics and group theory is needed.

Non-stationary modes

Inspired by the calculation of two particles case, we try to find the Bethe solution of the N particles system by taking the following Ansatz:

$$\Psi(x_1, x_2, \dots, x_N) = \sum_{\sigma \in S_N} \prod_{n=1}^N \psi_n^\sigma(x_{\sigma(n)}), \quad (4.72)$$

where S_N is the group of permutations of N elements and ψ_n^σ is the building block function draw from Eq. (4.49), either stationary or non-stationary. The subscript n denotes the index of class in which all functions share the same wave vector p_n . For example, in the notation of our previous two particle case, $\{\psi_1, \tilde{\psi}_1\}$ is the class with index $n = 1$. Notice that $n \in \{1, 2, \dots, N\}$ and N is the total number of particles in the system. The superscript σ is the N -element index arrangement used to distinguish different functions in one class. These functions are different by the amplitude coefficients A_n^σ or $A_{n\pm}^\sigma$ depending on whether it is a stationary or a non-stationary class. For example, in the two particle case, the class $n = 1$ contains two functions with coefficients $\{A_1^{12}, A_1^{21}\}$ or $\{A_{1\pm}^{12}, A_{1\pm}^{21}\}$. However, for simplicity, we just use the tilde symbol to denote the functions in our previous calculation.

Now, let us assume Eq. (4.72) is constructed by N_s stationary classes of ψ and $N - N_s$ non-stationary classes of ψ . Notice that $N_s = 0$ corresponds to the both non-stationary type in our previous discussion of the two particle system. And $1 < N_s < N$ corresponds to the mixed non-stationary type in the previous discussion. We will also discuss them separately here.

Firstly, let us insert the solution in to the master equation Eq. (4.64), notice that the amplitude coefficients are irrelevant with the eigenvalues. So we obtain the simple form of corresponding eigenvalue

$$\Lambda = \sum_{n=1}^{N-N_s} \lambda_n, \quad (4.73)$$

where $\lambda_n = -(\alpha + \beta) + 2\sqrt{\alpha\beta} \cos(p_n)$. Notice that, as in the two particles example, the Bethe Equations stated later will give the value of p_n and determine the eigenvalues. In general, they are more than one solution because Bethe Equations are nonlinear, and different solution can lead to different eigenvalues. Now we can discuss the Bethe equations of the two types of non-stationary eigenmodes.

For the case of $N_s = 0$, plug Eq. (4.72) in to the reflecting boundaries Eq. (4.65) we can obtain

$$\frac{A_{n+}^{\sigma|\sigma(1)=n}}{A_{n-}^{\sigma|\sigma(1)=n}} = -\frac{\alpha - \sqrt{\alpha\beta}e^{-ip_n}}{\alpha - \sqrt{\alpha\beta}e^{ip_n}}, \quad (4.74a)$$

$$\frac{A_{n+}^{\sigma|\sigma(N)=n}}{A_{n-}^{\sigma|\sigma(N)=n}} = -\frac{(\alpha - \sqrt{\alpha\beta}e^{-ip_n})e^{-ip_nL}}{(\alpha - \sqrt{\alpha\beta}e^{ip_n})e^{ip_nL}}. \quad (4.74b)$$

And substitute the Ansatz in to the Exclusive condition Eq. (4.66) we get

$$\frac{A_{n\pm}^{\sigma} A_{(n+1)\pm}^{\sigma}}{A_{n\pm}^{\sigma|n\leftrightarrow n+1} A_{(n+1)\pm}^{\sigma|n\leftrightarrow n+1}} = -\frac{a(\pm p_n, \pm p_{n+1})}{a(\pm p_{n+1}, \pm p_n)}, \quad (4.75)$$

with $a(p, p') = \sqrt{\alpha\beta}e^{i(p+p')} - (\alpha + \beta)e^{ip} + \sqrt{\alpha\beta}$. Then one can either use the consistency condition or the interpretation we discussed in the two particles case and the well know periodic Bethe Equation, easily find the following set of Bethe Equations for the N particles system:

$$e^{i2p_nL} = \prod_{m \neq n}^N \frac{a(p_n, p_m)}{a(p_m, p_n)} \frac{a(p_m, -p_n)}{a(-p_n, p_m)}. \quad (4.76)$$

By solving Eq. (4.76) we get all the p_n and then one can plug back in Eq. (4.73) and Eq. (4.72) for the corresponding eigenvalues and eigenfunctions.

Now let us discuss the case that $0 < N_s < N$. The calculation of the two particles system is a good illustration. We can easily find out there is nothing different except we will have only $N - N_s$ wave vectors and $2N - N_s$ amplitude coefficients. So one just have to use the relation similar to Eq. (4.55) together with Eq. (4.74) to build the Bethe Equation. Moreover, Eq. (4.57) tells us that the Bethe Equations we can obtain will be exact the same as the Bethe Equations of the second type $N - N_s$ particles system. So according to Eq. (4.73) for the eigenvalues, we can conclude that the eigenvalues of $N - N_s$ particles system are always contained in the eigenvalue set of N particle system. Notice that this is only true for $N < L/2$. For $N > L/2$, one can easily use the particle-hole duality which shows that the eigenvalue of N particles system should be the same as $L - N$ particles system. This important structure of the solution explains our simulation results stated in section 4.2.3.

This kind of embedding structure is verified by our simulations. In Fig. 4.8, we show in the left panel that eigenvalues of case $N = 1$ are contained in the set of eigenvalues $N = 2$, and all eigenvalues of case $N = 2$ are contained in the set of $N = 3$. In the right panel, the eigenvalues obtained from the brute force diagonalize of Markovian matrix and from the

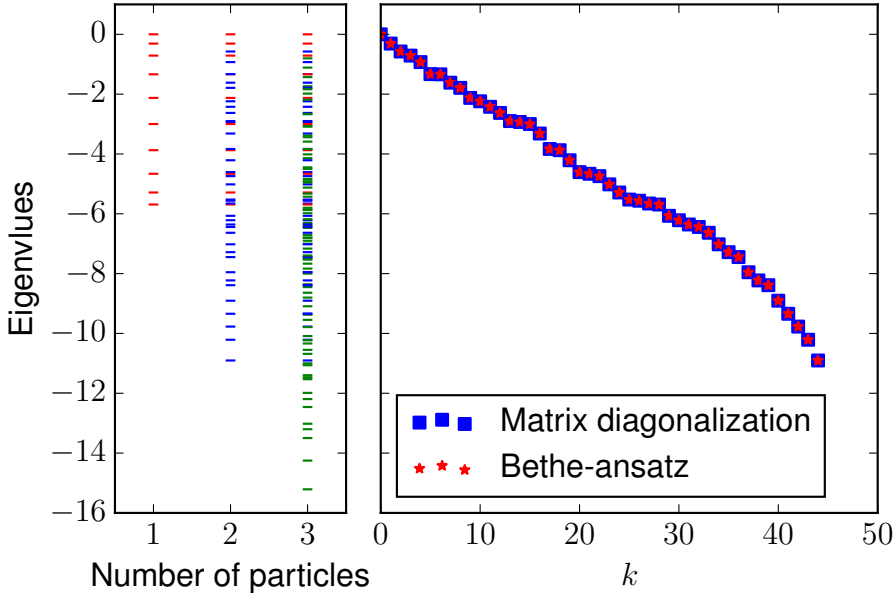


Fig. 4.8 The left panel: the embedding structure of eigenvalues illustrated by a system of $L = 10$ with one, two and three particles. $\alpha = 2, \beta = 1$. The right panel: eigenvalue obtained from brute force digitalization of Markovian matrix and from the Bethe equations. $\alpha = 2, \beta = 1, L = 10, N = 2$.

solution of the Bethe equations Eq. (4.76) are compared. We can see that they are identical to each other.

Finally, we remark that the Bethe Equations have to be solved numerically in most cases. However, there is a small set of non-stationary eigenvalue and eigenvectors we can obtain analytically, which correspond to the case with just one excitation mode. The results are summarized as following:

$$\Lambda_k = -(\alpha + \beta) + 2\sqrt{\alpha\beta} \cos\left(\frac{k\pi}{L}\right), \quad k = 1, 2, \dots, L-1; \quad (4.77a)$$

$$\Psi_k(x_1, x_2, \dots, x_N) = A \sum_{n=1}^N \left(\frac{\alpha}{\beta}\right)^{n-1} \phi_k(x_n) \prod_{m \neq n} \left(\frac{\alpha}{\beta}\right)^{x_m}. \quad (4.77b)$$

Notice that the set of eigenvalue is exactly the single particle spectrum, and again $\phi_k(x)$ is exactly the single particle eigenfunction. Fortunately, the numerical evidence shows that the most interesting eigenmode, i.e. the slowest relaxation mode, is contained in this set. We will discuss it in next section.

4.3.4 Relaxation time

The largest non-zero eigenvalue we found and verified by numerical results is

$$\Lambda_1 = -(\alpha + \beta) + 2\sqrt{\alpha\beta} \cos\left(\frac{\pi}{L}\right) \quad (4.78)$$

Let us assume $L \gg 1$, then we can expand the cosine term, obtain

$$\Lambda_1 = -(\sqrt{\beta} - \sqrt{\alpha})^2 - \frac{\sqrt{\alpha\beta}\pi^2}{L^2} \quad (4.79)$$

And the relaxation time can be calculated as $\tau = -\frac{1}{\Lambda_1}$.

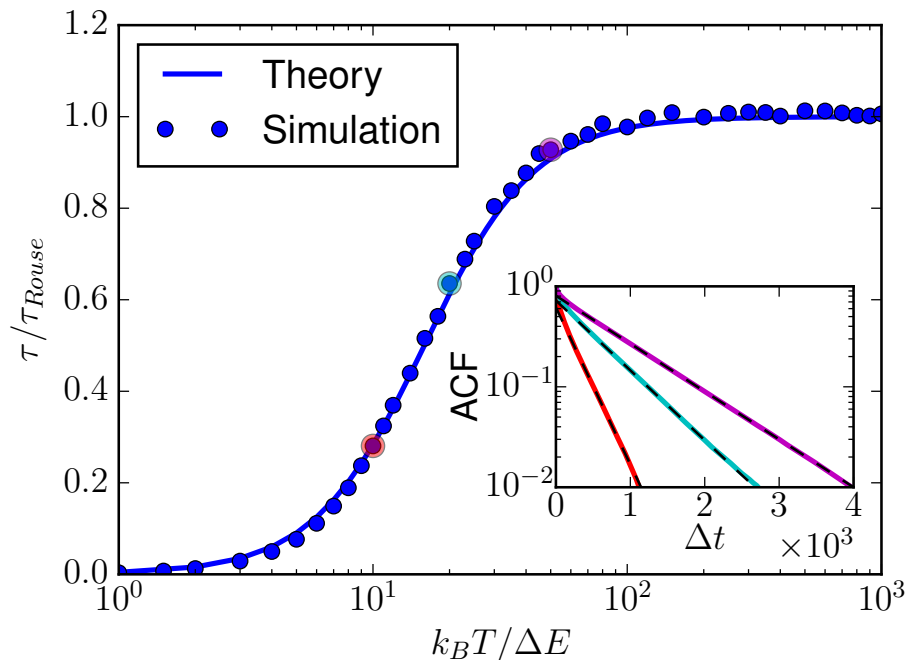


Fig. 4.9 Relaxation time of 1D model varies with the dimensionless temperature $\tilde{T} := k_B T / \Delta E$. The y axis is normalized with the Rouse relaxation time. The ACF curves for several typical cases are shown in the inset. The corresponding relaxation time is fitted and show with dashed black lines, which are also marked with the same color in the simulation dots.

There are several information we can read form Eq. (4.79). Let us discuss the strong and weak external force regime separately. In the strong external force regime, the bias of hopping rate is large. Without loss of generality, we can assume $\beta \gg \alpha$. Then $\Lambda_1 \rightarrow -\beta$ and the relaxation time $\tau \rightarrow 1/\beta$. So the relaxation time of the system tends to be a constant which is independent of the system size. Moreover, the relaxation time $\tau \rightarrow 0$ as $\beta \rightarrow \infty$. In

in the weak external force regime, we have $\alpha \approx \beta$. Thus we obtain $\tau \approx \frac{L^2}{\sqrt{\alpha\beta\pi^2}}$. We can see the scaling $\tau \sim L^2$, which means the dynamical exponent of the system is 2.

Now, we can re-map the ASEP model back to the picture of polymer dynamics to discuss to the relaxation time of 1D polymer model. Utilize Eq. (4.25) and Eq. (4.24) and plug them into Eq. (4.78), the relaxation time can be calculated analytically. Moreover, in the weak external force limit, we have

$$\tau = \frac{\xi a^2 L^2}{\pi^2 k_B T}. \quad (4.80)$$

The result above can be compared with the prediction of one dimensional Rouse theory. According to our calculation in section 4.1, the one dimensional relaxation time of a pinned polymer loop is 3 times of the three dimensional model. We found it is exactly the same with our results here, even the pre-factor is the same. Also notice that the Rouse scaling with exponent 2 is recovered.

In Rouse theory, the relaxation time does not depend on external force. In contrast, we have here an obvious force dependence of the relaxation time. This point highlight the fundamental difference between the infinite extensible bead spring model and the rigid bead rod model which is of course finite extensible. In Fig. 4.9, we show how the relaxation time varies with the dimensionless temperature, which is defined as $\tilde{T} = \frac{k_B T}{2Fa}$. Notice $\tilde{T} \propto \frac{1}{F}$ when other parameters are fixed. As we can see from the figure, the relaxation time tends to zero in the strong force limit (left side) and approaches to the Rouse relaxation time in the weak force limit (right side). The theory matches with the simulation results perfectly. Moreover, the ACF of several cases are shown in the inset.

In this section, we use the generalized Bethe Ansatz methods solve the ASEP model with reflecting boundaries exactly. The stationary distribution obtained here is compared with our previous results. And the analytical relaxation time, which is verified by the simulation results, is analyzed in different cases. We also re-map it back to the polymer system to analyze the polymer dynamics in 1D. However, the 1D polymer is of course a idealized model only exists in our imagination. In next section, we will try to use the results obtained here to further analyze the real three dimensional polymer system.

4.4 Dynamics of 3D bead-rod polymer loop

Unlike the 1D model discussed in previous section, the 3D bead-rod model can be studied precisely by the BD simulations. So we will discuss the BD simulation results in this section and apply the theory obtained in 1D ASEP to quantitatively rationalize our observations.

Moreover, we will compare our results with previous study on the pinned polymer model. Specifically, the blob theory from Pincus and Brochard-Wyart [4] will be discussed.

4.4.1 Relaxation time of 3D pinned Bead-rod Loop

Similar to the 1D model, our main interest of the polymer dynamics is the relaxation time. To measure the relaxation time of 3D pinned bead-rod polymer loop, we perform the BD simulation for different external force. The autocorrelation function of diameter vector, which is defined as $\mathbf{r}_d = \mathbf{r}_{\frac{L}{2}} - \mathbf{r}_0$ is measured to extract the relaxation time.

In fig. ?? we show some examples of the autocorrelation functions (ACF). We can see clearly in the figure, the slop of ACF is steeper as the external force increased, which results a smaller relaxation time.

Notice that \mathbf{r}_d is a three dimensional vector, thus we can obtain the ACF in three directions. By symmetric reason, the two directions perpendicular to the force direction will be the same. So in Fig. ?? we measure the relaxation time of the system varies with the dimensionless temperature, in both parallel and perpendicular directions of the external force field. We immediately find that the curve of $\tau_{\parallel}(\tilde{T})$ looks very similar to the 1D relaxation behavior. This is easy to understand as the 3D model projected to the force direction is somehow like a 1D model. So we try to use our 1D theory to fit the relaxation behavior of τ_{\parallel} .

In order to match the theory to the simulations, let us first discuss the case without external force field. In this case, the relaxation time is correctly predicted by the Rouse theory, we have

$$\tau_{Rouse} = \frac{\xi a^2 L^2}{3\pi^2 k_B T} \quad (4.81)$$

Moreover, the symmetry holds in all direction in this case. So we have both $\tau_{\parallel} = \tau_{\perp} = \tau_{Rouse}$ in this case. This is verified by the simulations as shown in Fig. ???. Compare Eq. (4.81) with Eq. (4.80) we can find that the only difference is the factor 3 in the denominator, which is easy to understand because the dimensionality of the system.

Now let us discuss the relaxation time varies with the external force. In the simulation, recall that the dimensionless temperature $\tilde{T} = \frac{k_B T}{Fa} \propto \frac{1}{F}$ when other parameters are fixed. It is reasonable to calibrate the relaxation from the Eq. (4.78) with the 3D Rouse time and then we can obtain

$$\tau = \frac{\xi a^2 L^2}{3\pi^2 k_B T} - \frac{\xi L^4 a^2 \left(e^{\frac{Fa}{k_B T}} - 1 \right)^2}{3\pi^2 k_B T \left(L^2 \left(e^{\frac{Fa}{k_B T}} - 1 \right)^2 + \pi^2 \left(e^{\frac{Fa}{k_B T}} + 1 \right)^2 \right)}. \quad (4.82)$$

We write it this form so that we can see a factor of Rouse time in it. Eq. (4.82) is compared with the simulation results in Fig. ??, we can see the excellent agreement with τ_{\parallel} . However, τ_{\perp} is not well described by the theory as we can see in the inset of Fig. ???. This is also easy to understand given that it is the relaxation perpendicular to the force field direction.

To further test our theory, we also do the simulation by changing other parameters such as the temperature T and the system size L . Let us discuss this two cases separately.

Interestingly, according to the prediction of Eq. (4.82), if we fixed other parameters except the temperature T under certain external force field, we will get a non-monotonic curve of $\tau(T)$, see in Fig. ???. Physically, it means that the relaxation of a bead-rod system will be slower if we increase the level of noise under certain force field. It is a counter-intuitive result. However, the results of from the BD simulation verifies this prediction, show in Fig. ??.

The relaxation time varies with the system size is show in Fig. ???. The simulation results are again correctly predicted by the theory. We will discuss more about this size scaling in next subsection when compare with the previous blob theory.

4.4.2 Comparison to the blob theory

4.5 Summary

Chapter 5

Characterize the Nuclear Oscillation

5.1 Oscillation of the Pinned Polymer Loop

5.1.1 The Rouse Theory

5.1.2 Simulation Results

5.2 Characterize the Shape of Chromosomes

5.2.1 The Gyration Tensor

5.2.2 Asphericity and the Nature of Asphericity

5.3 Extract Shape Information From Experimental Data

5.3.1 Shape from Experimental Data

5.3.2 Compare to Theory and Simulation Results

5.4 Summary

Chapter 6

Conclusions and Outlook

6.1 Conclusions

6.2 Outlook

Appendix A

**An efficient algorithm to compute *pseudo*
force of bead-rod loop**

Appendix B

Monte-Carlo simulation of 1D particle-lattice model

Appendix C

The Bethe-ansatz Solution of Periodic ASEP

Appendix D

The Toeplitz Matrix

The Toeplitz M

Appendix E

Derivation of the Exclusion Condition

To derivate the exclusion condition, which is a little bit confusing at a first sight, we use the two particles example and then generalise to N particle case. First, let us rewrite the master equation of this two particle system:

$$\begin{aligned} \frac{dP(x_1, x_2; t)}{dt} = & \alpha P(x_1 - 1, x_2; t) + \beta P(x_1 + 1, x_2; t) \\ & + \alpha P(x_1, x_2 - 1; t) + \beta P(x_1, x_2 + 1; t) \\ & - 2(\alpha + \beta)P(x_1, x_2; t) \end{aligned} \quad (\text{E.1})$$

We assume the above equation is valid for the whole space. However, this is actually not true when the two particles are sitting on the neighboring sites. Let us now consider this special case separately, remember that $x_2 = x_1 + 1$. The master equation of this special case can be written as

$$\begin{aligned} \frac{dP(x_1, x_2; t)}{dt} = & \alpha P(x_1 - 1, x_2; t) + \beta P(x_1, x_2 + 1; t) \\ & - (\alpha + \beta)P(x_1, x_2; t) \end{aligned} \quad (\text{E.2})$$

Now, let us do a subtraction, i.e. (E.1) – (E.2), obtain

$$\alpha P(x_1, x_2 - 1; t) + \beta P(x_1 + 1, x_2; t) = (\alpha + \beta)P(x_1, x_2; t) \quad (\text{E.3})$$

Let us then denote $x := x_1$ and plug in $x_2 = x_1 + 1 = x + 1$ in the above equation. We finally arrive at

$$\alpha P(x, x; t) + \beta P(x + 1, x + 1; t) = (\alpha + \beta)P(x, x + 1; t) \quad (\text{E.4})$$

In summary, the sole master equation Eq. (E.1) does not take into account the exclusion cases. In order to represent the exclusive setting, we assume Eq. (E.1) is valid for the whole space, and then apply an additional condition on this equation like Eq. (E.4). This condition

is similar to the partial derivative of the PDF is the same at the collision boundary $x_1 = x_2$ in the continuous space case.

Finally, in the similar way we can derive the exclusion condition for the cases $N > 2$. However, it is not difficult to check that in cases of more than two particles, the three body collision or four body collision cases do not give out new conditions, just the linear combination of the two body collision conditions like Eq. (F.4). This is fundamentally a result of Yang-Baxter Equation is satisfied for the ASEP model.

Appendix F

Single-file Diffusion with Reflecting Boundaries

To derive the exclusion condition, which is a little bit confusing at a first sight, we use the two particles example and then generalise to N particle case. First, let us rewrite the master equation of this two particle system:

$$\begin{aligned} \frac{dP(x_1, x_2; t)}{dt} = & \alpha P(x_1 - 1, x_2; t) + \beta P(x_1 + 1, x_2; t) \\ & + \alpha P(x_1, x_2 - 1; t) + \beta P(x_1, x_2 + 1; t) \\ & - 2(\alpha + \beta)P(x_1, x_2; t) \end{aligned} \quad (\text{F.1})$$

We assume the above equation is valid for the whole space. However, this is actually not true when the two particles are sitting on the neighboring sites. Let us now consider this special case separately, remember that $x_2 = x_1 + 1$. The master equation of this special case can be written as

$$\begin{aligned} \frac{dP(x_1, x_2; t)}{dt} = & \alpha P(x_1 - 1, x_2; t) + \beta P(x_1, x_2 + 1; t) \\ & - (\alpha + \beta)P(x_1, x_2; t) \end{aligned} \quad (\text{F.2})$$

Now, let us do a subtraction, i.e. (F.1) – (F.2), obtain

$$\alpha P(x_1, x_2 - 1; t) + \beta P(x_1 + 1, x_2; t) = (\alpha + \beta)P(x_1, x_2; t) \quad (\text{F.3})$$

Let us then denote $x := x_1$ and plug in $x_2 = x_1 + 1 = x + 1$ in the above equation. We finally arrive at

$$\alpha P(x, x; t) + \beta P(x + 1, x + 1; t) = (\alpha + \beta)P(x, x + 1; t) \quad (\text{F.4})$$

In summary, the sole master equation Eq. (F.1) does not take into account the exclusion cases. In order to represent the exclusive setting, we assume Eq. (F.1) is valid for the whole space, and then apply an additional condition on this equation like Eq. (F.4). This condition is similar to the partial derivative of the PDF is the same at the collision boundary $x_1 = x_2$ in the continuous space case.

Finally, in the similar way we can derive the exclusion condition for the cases $N > 2$. However, it is not difficult to check that in cases of more than two particles, the three body collision or four body collision cases do not give out new conditions, just the linear combination of the two body collision conditions like Eq. (F.4). This is fundamentally a result of Yang-Baxter Equation is satisfied for the ASEP model.

References

- [1] D O Morgan. *The Cell Cycle: Principles of Control*. Primers in Biology. OUP/New Science Press, 2007.
- [2] Haruhiko Asakawa, Tokuko Haraguchi, and Yasushi Hiraoka. Reconstruction of the kinetochore: a prelude to meiosis. *Cell Div.*, 2(1):17, 2007.
- [3] Mariola R. Chacón, Petrina Delivani, and Iva M. Tolić. Meiotic Nuclear Oscillations Are Necessary to Avoid Excessive Chromosome Associations. *Cell Rep.*, 17(6):1632–1645, nov 2016.
- [4] F. Brochard-Wyart. Polymer Chains Under Strong Flows: Stems and Flowers. *Europhys. Lett.*, 30(7):387–392, jun 1995.
- [5] Sven K Vogel, Nenad Pavin, Nicola Maghelli, Frank Jülicher, and Iva M Tolić-Nørrelykke. Self-Organization of Dynein Motors Generates Meiotic Nuclear Oscillations. *PLoS Biol.*, 7(4):e1000087, apr 2009.
- [6] Carolyn T. MacDonald, Julian H. Gibbs, and Allen C. Pipkin. Kinetics of Biopolymerization. *Biopolymers*, 6:1–25, 1968.
- [7] Paul C. Bressloff, Jay M. Newby, and B. Derrida. Stochastic models of intracellular transport. *Rev. Mod. Phys.*, 301(1-3):135–196, 2013.
- [8] T Chou, K Mallick, and R K P Zia. Non-equilibrium statistical mechanics: from a paradigmatic model to biological transport. *Reports Prog. Phys.*, 74(11):116601, nov 2011.
- [9] Alan A Berryman. The Origins and Evolution of Predator-Prey Theory. *Ecology*, 73(5):1530–1535, oct 1992.
- [10] Thomas Butler and Nigel Goldenfeld. Robust ecological pattern formation induced by demographic noise. *Phys. Rev. E*, 80(3):030902, sep 2009.
- [11] G. Sugihara, R. May, H. Ye, C.-h. Hsieh, E. Deyle, M. Fogarty, and S. Munch. Detecting Causality in Complex Ecosystems. *Science (80-.).*, 338(6106):496–500, oct 2012.
- [12] Jennifer L Williams, Bruce E Kendall, and Jonathan M Levine. Rapid evolution accelerates plant population spread in fragmented experimental landscapes. *Science (80-.).*, 353(6298):482–485, jul 2016.

- [13] Y Chikashige, D. Ding, H Funabiki, T Haraguchi, S Mashiko, M Yanagida, and Y Hiraoka. Telomere-led premeiotic chromosome movement in fission yeast. *Science*, (80-.), 264(5156):270–273, apr 1994.
- [14] Hiroki Shibuya, Akihiro Morimoto, and Yoshinori Watanabe. The Dissection of Meiotic Chromosome Movement in Mice Using an In Vivo Electroporation Technique. *PLoS Genet.*, 10(12):e1004821, 2014.
- [15] A Yamamoto, C Tsutsumi, H Kojima, K Oiwa, and Y Hiraoka. Dynamic Behavior of Microtubules during Dynein-dependent Nuclear Migrations of Meiotic Prophase in Fission Yeast. *Mol. Biol. Cell*, 12(12):3933–3946, dec 2001.
- [16] Da-Qiao Ding, Ayumu Yamamoto, Tokuko Haraguchi, and Yasushi Hiraoka. Dynamics of Homologous Chromosome Pairing during Meiotic Prophase in Fission Yeast. *Dev. Cell*, 6(3):329–341, mar 2004.
- [17] Jennifer L Gerton and R Scott Hawley. Homologous chromosome interactions in meiosis: diversity amidst conservation. *Nat. Rev. Genet.*, 6(6):477–487, jun 2005.
- [18] Pierre-Gilles G de Gennes. *Scaling Concepts in Polymer Physics*. Cornell University Press, 1979.
- [19] M. Doi and S. F. Edwards. *The theory of polymer dynamics*. Oxford University Press, 1988.
- [20] Yen Ting Lin, Daniela Frömberg, Wenwen Huang, Petrina Delivani, Mariola Chacón, Iva M. Tolić, Frank Jülicher, and Vasily Zaburdaev. Pulled Polymer Loops as a Model for the Alignment of Meiotic Chromosomes. *Phys. Rev. Lett.*, 115(20):208102, nov 2015.
- [21] Susan L Forsburg. Overview of *Schizosaccharomyces pombe*. In *Curr. Protoc. Mol. Biol.*, volume Chapter 13, page Unit 13.14. 2003.
- [22] Peter A. Fantes and Charles S. Hoffman. A Brief History of *Schizosaccharomyces pombe* Research: A Perspective Over the Past 70 Years. *Genetics*, 203(2):621–629, jun 2016.
- [23] Charles S. Hoffman, Valerie Wood, and Peter A. Fantes. An Ancient Yeast for Young Geneticists: A Primer on the *Schizosaccharomyces pombe* Model System. *Genetics*, 201(2):403–423, oct 2015.
- [24] V. Wood, R. Gwilliam, M.-A. Rajandream, M. Lyne, R. Lyne, A. Stewart, J. Sgouros, N. Peat, J. Hayles, S. Baker, D. Basham, S. Bowman, K. Brooks, D. Brown, S. Brown, T. Chillingworth, C. Churcher, M. Collins, R. Connor, A. Cronin, P. Davis, T. Feltwell, A. Fraser, S. Gentles, A. Goble, N. Hamlin, D. Harris, J. Hidalgo, G. Hodgson, S. Holroyd, T. Hornsby, S. Howarth, E. J. Huckle, S. Hunt, K. Jagels, K. James, L. Jones, M. Jones, S. Leather, S. McDonald, J. McLean, P. Mooney, S. Moule, K. Mungall, L. Murphy, D. Niblett, C. Odell, K. Oliver, S. O’Neil, D. Pearson, M. A. Quail, E. Rabinowitzsch, K. Rutherford, S. Rutter, D. Saunders, K. Seeger, S. Sharp, J. Skelton, M. Simmonds, R. Squares, S. Squares, K. Stevens, K. Taylor,

- R. G. Taylor, A. Tivey, S. Walsh, T. Warren, S. Whitehead, J. Woodward, G. Volckaert, R. Aert, J. Robben, B. Grymonprez, I. Weltjens, E. Vanstreels, M. Rieger, M. Schäfer, S. Müller-Auer, C. Gabel, M. Fuchs, C. Fritz, E. Holzer, D. Moestl, H. Hilbert, K. Borzym, I. Langer, A. Beck, H. Lehrach, R. Reinhardt, T. M. Pohl, P. Eger, W. Zimmermann, H. Wedler, R. Wambutt, B. Purnelle, A. Goffeau, E. Cadieu, S. Dréano, S. Gloux, V. Lelaure, S. Mottier, F. Galibert, S. J. Aves, Z. Xiang, C. Hunt, K. Moore, S. M. Hurst, M. Lucas, M. Rochet, C. Gaillardin, V. A. Tallada, A. Garzon, G. Thode, R. R. Daga, L. Cruzado, J. Jimenez, M. Sánchez, F. del Rey, J. Benito, A. Domínguez, J. L. Revuelta, S. Moreno, J. Armstrong, S. L. Forsburg, L. Cerrutti, T. Lowe, W. R. McCombie, I. Paulsen, J. Potashkin, G. V. Shpakovski, D. Ussery, B. G. Barrell, and P. Nurse. The genome sequence of *Schizosaccharomyces pombe*. *Nature*, 415(6874):871–880, feb 2002.
- [25] Miguel Coelho, Aygül Dereli, Anett Haese, Sebastian Kühn, Liliana Malinovska, Morgan E. DeSantis, James Shorter, Simon Alberti, Thilo Gross, and Iva M. Tolić-Nørrelykke. Fission Yeast Does Not Age under Favorable Conditions, but Does So after Stress. *Curr. Biol.*, 23(19):1844–1852, oct 2013.
- [26] S Freeman. *Biological Science*. Pearson/Benjamin Cummings, 2008.
- [27] a M Villeneuve and K J Hillers. Whence meiosis? *Cell*, 106(6):647–650, 2001.
- [28] David M. Richards, Emma Greer, Azahara C. Martin, Graham Moore, Peter J. Shaw, and Martin Howard. Quantitative Dynamics of Telomere Bouquet Formation. *PLoS Comput. Biol.*, 8(12):e1002812, dec 2012.
- [29] L Davis and G R Smith. Meiotic recombination and chromosome segregation in *Schizosaccharomyces pombe*. *Proc. Natl. Acad. Sci.*, 98(15):8395–8402, jul 2001.
- [30] Osami Niwa, Mizuki Shimanuki, and Futaba Miki. Telomere-led bouquet formation facilitates homologous chromosome pairing and restricts ectopic interaction in fission yeast meiosis. *EMBO J.*, 19(14):3831–3840, jul 2000.
- [31] D Q Ding, Y Chikashige, T Haraguchi, and Y Hiraoka. Oscillatory nuclear movement in fission yeast meiotic prophase is driven by astral microtubules, as revealed by continuous observation of chromosomes and microtubules in living cells. *J. Cell Sci.*, 111 (Pt 6):701–12, mar 1998.
- [32] Jennifer L. Wells, David W. Pryce, and Ramsay J. McFarlane. Homologous chromosome pairing in *Schizosaccharomyces pombe*. *Yeast*, 23(13):977–989, oct 2006.
- [33] Romain Koszul and Nancy Kleckner. Dynamic chromosome movements during meiosis: a way to eliminate unwanted connections? *Trends Cell Biol.*, 19(12):716–724, 2009.
- [34] Hua Wong, Jean-michel Arbona, and Christophe Zimmer. How to build a yeast nucleus. *Nucleus*, 4(5):361–366, sep 2013.
- [35] Douglas R. Tree, Abhiram Muralidhar, Patrick S. Doyle, and Kevin D. Dorfman. Is DNA a Good Model Polymer. *Macromolecules*, 46(20):8369–8382, oct 2013.

- [36] Jonathan D Halverson, Jan Smrek, Kurt Kremer, and Alexander Y Grosberg. From a melt of rings to chromosome territories: the role of topological constraints in genome folding. *Reports Prog. Phys.*, 77(2):022601, feb 2014.
- [37] Suckjoon Jun and Andrew Wright. Entropy as the driver of chromosome segregation. *Nat. Rev. Microbiol.*, 8(8):600–607, 2010.
- [38] D. Richter, S. Gooßen, and A. Wischnewski. Celebrating Soft Matter’s 10th Anniversary: Topology matters: structure and dynamics of ring polymers. *Soft Matter*, 11(44):8535–8549, 2015.
- [39] H. A. Kramers. The Behavior of Macromolecules in Inhomogeneous Flow. *J. Chem. Phys.*, 14(7):415–424, jul 1946.
- [40] Bruno H. Zimm and Walter H. Stockmayer. The Dimensions of Chain Molecules Containing Branches and Rings. *J. Chem. Phys.*, 17(12):1301–1314, 1949.
- [41] Edward F. Casassa. Some statistical properties of flexible ring polymers. *J. Polym. Sci. Part A Gen. Pap.*, 3(2):605–614, feb 1965.
- [42] W BURCHARD and M SCHMIDT. Static and dynamic structure factors calculated for flexible ring macromolecules. *Polymer (Guildf.)*, 21(7):745–749, jul 1980.
- [43] A. Baumg\{"o\}rtner. Statistics of self-avoiding ring polymers. *J. Chem. Phys.*, 76(8):4275, nov 1982.
- [44] M.E. Cates and J.M. Deutsch. Conjectures on the statistics of ring polymers. *J. Phys.*, 47(12):2121–2128, 1986.
- [45] Sergei P. Obukhov, Michael Rubinstein, and Thomas Duke. Dynamics of a Ring Polymer in a Gel. *Phys. Rev. Lett.*, 73(9):1263–1266, aug 1994.
- [46] Wilfried Carl. Configurational and rheological properties of cyclic polymers. *J. Chem. Soc. Faraday Trans.*, 91(16):2525–2530, 1995.
- [47] W. Carl. Some aspects of theory and simulations of polymers in steady flows. *Macromol. Theory Simulations*, 5(1):1–27, 1996.
- [48] Sergey Panyukov and Yitzhak Rabin. Fluctuating elastic rings: Statics and dynamics. *Phys. Rev. E*, 64(1):011909, jun 2001.
- [49] Debashish Mukherji, Guido Bartels, and Martin H. Müser. Scaling laws of single polymer dynamics near attractive surfaces. *Phys. Rev. Lett.*, 100(February):1–4, 2008.
- [50] Takahiro Sakaue. Ring polymers in melts and solutions: Scaling and crossover. *Phys. Rev. Lett.*, 106(April):1–4, 2011.
- [51] Takahiro Sakaue. Statistics and geometrical picture of ring polymer melts and solutions. *Phys. Rev. E*, 85(2):021806, feb 2012.
- [52] Jaeup U. Kim, Yong-Biao Yang, and Won Bo Lee. Self-Consistent Field Theory of Gaussian Ring Polymers. *Macromolecules*, 45(7):3263–3269, apr 2012.

- [53] Shang Yik Reigh and Do Y. Yoon. Concentration Dependence of Ring Polymer Conformations from Monte Carlo Simulations. *ACS Macro Lett.*, 2(4):296–300, apr 2013.
- [54] Philipp S. Lang, Benedikt Obermayer, and Erwin Frey. Dynamics of a semiflexible polymer or polymer ring in shear flow. *Phys. Rev. E*, 89(2):022606, feb 2014.
- [55] Angelo Rosa and Ralf Everaers. Structure and Dynamics of Interphase Chromosomes. *PLoS Comput. Biol.*, 4(8):e1000153, aug 2008.
- [56] Angelo Rosa and Ralf Everaers. Ring Polymers in the Melt State: The Physics of Crumpling. *Phys. Rev. Lett.*, 112(11):118302, mar 2014.
- [57] Julien Dorier and Andrzej Stasiak. Topological origins of chromosomal territories. *Nucleic Acids Res.*, 37(19):6316–6322, oct 2009.
- [58] R K Sachs, G van den Engh, B Trask, H Yokota, and J E Hearst. A random-walk/giant-loop model for interphase chromosomes. *Proc. Natl. Acad. Sci.*, 92(7):2710–2714, mar 1995.
- [59] John F Marko. Linking topology of tethered polymer rings with applications to chromosome segregation and estimation of the knotting length. *Phys. Rev. E*, 79(5):051905, may 2009.
- [60] Angelo Rosa, Nils B Becker, and Ralf Everaers. Looping probabilities in model interphase chromosomes. *Biophys. J.*, 98(11):2410–9, jun 2010.
- [61] Yang Zhang and Dieter W. Heermann. Loops determine the mechanical properties of mitotic chromosomes. *PLoS One*, 6(12):e29225, dec 2011.
- [62] Hua Wong, Hervé Marie-Nelly, Sébastien Herbert, Pascal Carrivain, Hervé Blanc, Romain Koszul, Emmanuelle Fabre, and Christophe Zimmer. A Predictive Computational Model of the Dynamic 3D Interphase Yeast Nucleus. *Curr. Biol.*, 22(20):1881–1890, oct 2012.
- [63] Job Dekker, Marc a Marti-Renom, and Leonid a Mirny. Exploring the three-dimensional organization of genomes: interpreting chromatin interaction data. *Nat. Rev. Genet.*, 14(6):390–403, may 2013.
- [64] Luca Giorgietti, Rafael Galupa, Elphège P Nora, Tristan Piolot, France Lam, Job Dekker, Guido Tiana, and Edith Heard. Predictive polymer modeling reveals coupled fluctuations in chromosome conformation and transcription. *Cell*, 157(4):950–63, may 2014.
- [65] Brenda Youngren, Henrik Jörk Nielsen, Suckjoon Jun, and Stuart Austin. The multi-fork Escherichia coli chromosome is a self-duplicating and self-segregating thermodynamic ring polymer. *Genes Dev.*, 28:71–84, 2014.
- [66] Miriam Fritzsche and Dieter W. Heermann. Confinement driven spatial organization of semiflexible ring polymers: Implications for biopolymer packaging. *Soft Matter*, 7(15):6906, 2011.

- [67] Bae-Yeon Ha and Youngkyun Jung. Polymers under confinement: single polymers, how they interact, and as model chromosomes. *Soft Matter*, 11(12):2333–2352, 2015.
- [68] S. F. Tead, E. J. Kramer, G. Hadzioannou, M. Antonietti, H. Sillescu, P. Lutz, and C. Strazielle. Polymer topology and diffusion: a comparison of diffusion in linear and cyclic macromolecules. *Macromolecules*, 25(15):3942–3947, jul 1992.
- [69] M Kapnistos, M Lang, D Vlassopoulos, W Pyckhout-Hintzen, D Richter, D Cho, T Chang, and M Rubinstein. Unexpected power-law stress relaxation of entangled ring polymers. *Nat. Mater.*, 7(12):997–1002, dec 2008.
- [70] Guillaume Witz, Kristian Rechendorff, Jozef Adamcik, and Giovanni Dietler. Conformation of circular DNA in two dimensions. *Phys. Rev. Lett.*, 101(14):3–6, 2008.
- [71] G. Witz, K. Rechendorff, J. Adamcik, and G. Dietler. Conformation of ring polymers in 2D constrained environments. *Phys. Rev. Lett.*, 106(June):2–5, 2011.
- [72] S Gooßen, ARE Brás, M Krutyeva, M Sharp, P Falus, A Feoktystov, U Gasser, W. Pyckhout-Hintzen, A Wischnewski, and D Richter. Molecular Scale Dynamics of Large Ring Polymers. *Phys. Rev. Lett.*, 113(16):168302, oct 2014.
- [73] Sebastian Gooßen, Margarita Krutyeva, Melissa Sharp, Artem Feoktystov, Jürgen Allgaier, Wim Pyckhout-Hintzen, Andreas Wischnewski, and Dieter Richter. Sensing Polymer Chain Dynamics through Ring Topology: A Neutron Spin Echo Study. *Phys. Rev. Lett.*, 115(14):148302, 2015.
- [74] Marvin Bishop and J. P. J. Michels. The shape of ring polymers. *J. Chem. Phys.*, 82(2):1059–1061, jan 1985.
- [75] O. Jagodzinski, E. Eisenriegler, and K. Kremer. Universal shape properties of open and closed polymer chains: renormalization group analysis and Monte Carlo experiments. *J. Phys. I Fr.*, 2:2243–2279, 1992.
- [76] Karen Alim and Erwin Frey. Shapes of semiflexible polymer rings. *Phys. Rev. Lett.*, 99(November):1–4, 2007.
- [77] Pascal Reiss, Miriam Fritzsche, and Dieter W. Heermann. Looped star polymers show conformational transition from spherical to flat toroidal shapes. *Phys. Rev. E*, 84(5):051910, nov 2011.
- [78] J.P.J. Michels and F.W. Wiegel. Probability of knots in a polymer ring. *Phys. Lett. A*, 90(7):381–384, 1982.
- [79] Kleanthes Koniaris and M. Muthukumar. Knottedness in ring polymers. *Phys. Rev. Lett.*, 66(17):2211–2214, 1991.
- [80] Kleanthes Koniaris and M. Muthukumar. Self-entanglement in ring polymers. *J. Chem. Phys.*, 95(4):2873, 1991.
- [81] Alexander Grosberg, Alexander Feigel, and Yitzhak Rabin. Flory-type theory of a knotted ring polymer. *Phys. Rev. E*, 54(6):6618–6622, 1996.

- [82] Miyuki K Shimamura and Tetsuo Deguchi. Gyration radius of a circular polymer under a topological constraint with excluded volume. *Phys. Rev. E*, 64(2):020801, jul 2001.
- [83] E Orlandini, a L Stella, and C Vanderzande. Polymer θ -point as a knot delocalization transition. *Phys. Rev. E*, 68(3):031804, sep 2003.
- [84] Luca Tubiana, Enzo Orlandini, and Cristian Micheletti. Multiscale entanglement in ring polymers under spherical confinement. *Phys. Rev. Lett.*, 107(October):1–4, 2011.
- [85] Erica Uehara and Tetsuo Deguchi. Statistical and hydrodynamic properties of double-ring polymers with a fixed linking number between twin rings. *J. Chem. Phys.*, 140(4), 2014.
- [86] Bing Li, Zhao-Yan Yan Sun, and Li-Jia Jia An. Effects of topology on the adsorption of singly tethered ring polymers to attractive surfaces. *J. Chem. Phys.*, 143(2):024908, 2015.
- [87] P. G. De Gennes. Coil-stretch transition of dilute flexible polymers under ultrahigh velocity gradients. *J. Chem. Phys.*, 60(12):5030–5042, jun 1974.
- [88] P Pincus. Excluded Volume Effects and Stretched Polymer Chains. *Macromolecules*, 9(3):386–388, may 1976.
- [89] P. Pincus. Dynamics of Stretched Polymer Chains. *Macromolecules*, 10(1):210–213, jan 1977.
- [90] F Brochard-Wyart. Deformations of One Tethered Chain in Strong Flows. *Europhys. Lett.*, 23(2):105–111, jul 1993.
- [91] F Brochard-Wyart, H Hervet, and P Pincus. Unwinding of Polymer Chains under Forces or Flows. *Europhys. Lett.*, 26(7):511–516, jun 1994.
- [92] A Adjarei, F Brochardt-Wyart, and P G de Gennes. Drag on a Tethered Chain in a Polymer Melt. *J. Phys. II Fr.*, 5:491, 1995.
- [93] Thomas Perkins, Douglas Smith, Ronald Larson, and Steven Chu. Stretching of a single tethered polymer in a uniform flow. *Science (80-.).*, 268(5207):83–87, apr 1995.
- [94] T. Perkins, D. Smith, and S Chu. Direct observation of tube-like motion of a single polymer chain. *Science (80-.).*, 264(5160):819–822, may 1994.
- [95] T. Perkins, Quake, D. Smith, and S Chu. Relaxation of a single DNA molecule observed by optical microscopy. *Science (80-.).*, 264(5160):822–826, may 1994.
- [96] D Wirtz. Direct Measurement of the Transport-Properties of a Single DNA Molecule. *Phys. Rev. Lett.*, 75(12):2436–2439, 1995.
- [97] R Rzehak, D Kienle, T Kawakatsu, and W Zimmermann. Partial draining of a tethered polymer in flow. *Europhys. Lett.*, 46(6):821–826, jun 1999.

- [98] R. G. Larson, Hua Hu, D. E. Smith, and S. Chu. Brownian dynamics simulations of a DNA molecule in an extensional flow field. *J. Rheol. (N. Y. N. Y.)*, 43(2):267, 1999.
- [99] P S Doyle, B Ladoux, and J L Viovy. Dynamics of a tethered polymer in shear flow. *Phys. Rev. Lett.*, 84(20):4769–4772, 2000.
- [100] B Ladoux and P S Doyle. Stretching tethered DNA chains in shear flow. *Europhys. Lett.*, 52(5):511–517, dec 2000.
- [101] K L Sebastian. Pulling a polymer out of a potential well and the mechanical unzipping of DNA. *Phys. Rev. E*, 62(1):1128–1132, jul 2000.
- [102] Y Cui and C Bustamante. Pulling a single chromatin fiber reveals the forces that maintain its higher-order structure. *Proc. Natl. Acad. Sci.*, 97(1):127–132, jan 2000.
- [103] R Rzehak. Conformational fluctuations of a tethered polymer in uniform flow. *Eur. Phys. J. E - Soft Matter*, 11(4):335–348, aug 2003.
- [104] Aruna Mohan and Patrick S Doyle. Unraveling of a Tethered Polymer Chain in Uniform Solvent Flow. *Macromolecules*, 40(12):4301–4312, jun 2007.
- [105] Charles E. Sing and Alfredo Alexander-Katz. Theory of tethered polymers in shear flow: The strong stretching limit. *Macromolecules*, 44(22):9020–9028, 2011.
- [106] Takahiro Sakaue, Takuya Saito, and Hirofumi Wada. Dragging a polymer in a viscous fluid: Steady state and transient. *Phys. Rev. E*, 86(1):011804, jul 2012.
- [107] Anoop Varghese, Satyavani Vemparala, and R. Rajesh. Force fluctuations in stretching a tethered polymer. *Phys. Rev. E*, 88(2):022134, 2013.
- [108] Liang Dai and Patrick S. Doyle. Comparisons of a polymer in confinement versus applied force. *Macromolecules*, 46(15):6336–6344, 2013.
- [109] David Patterson. Molecular genetic analysis of Down syndrome. *Hum. Genet.*, 126(1):195–214, jul 2009.
- [110] Madan Somasi, Bamin Khomami, Nathanael J. Woo, Joe S. Hur, and Eric S.G. Shaqfeh. Brownian dynamics simulations of bead-rod and bead-spring chains: numerical algorithms and coarse-graining issues. *J. Nonnewton. Fluid Mech.*, 108(1-3):227–255, dec 2002.
- [111] C. Cruz, F. Chinesta, and G. Régnier. Review on the Brownian Dynamics Simulation of Bead-Rod-Spring Models Encountered in Computational Rheology. *Arch. Comput. Methods Eng.*, 19(2):227–259, jun 2012.
- [112] M. Fixman. Classical Statistical Mechanics of Constraints: A Theorem and Application to Polymers. *Proc. Natl. Acad. Sci.*, 71(8):3050–3053, 1974.
- [113] Matteo Pasquali and David C. Morse. An efficient algorithm for metric correction forces in simulations of linear polymers with constrained bond lengths. *J. Chem. Phys.*, 116(5):1834, 2002.

- [114] Tony W. Liu. Flexible polymer chain dynamics and rheological properties in steady flows. *J. Chem. Phys.*, 90(10):5826, 1989.
- [115] Rebecca L. Honeycutt. Stochastic Runge-Kutta algorithms. I. White noise. *Phys. Rev. A*, 45(2):600–603, jan 1992.
- [116] Kurt Binder. *Monte Carlo and Molecular Dynamics Simulations in Polymers Science*. Oxford University Press, 1995.
- [117] William Feller. *An Introduction to Probability Theory and Its Applications*. Wiley India Pvt. Limited, 2 edition, 2008.
- [118] Krishna B. Athreya and Soumendra N. Lahiri. *Measure Theory and Probability Theory*. Springer, 2006.
- [119] G E Andrews. *The Theory of Partitions*. Cambridge mathematical library. Cambridge University Press, 1998.
- [120] Shiori Toba, Tomonobu M Watanabe, Lisa Yamaguchi-Okimoto, Yoko Yano Toyoshima, and Hideo Higuchi. Overlapping hand-over-hand mechanism of single molecular motility of cytoplasmic dynein. *Proc. Natl. Acad. Sci.*, 103(15):5741–5745, apr 2006.
- [121] Arne Gennerich, Andrew P Carter, Samara L Reck-Peterson, and Ronald D Vale. Force-Induced Bidirectional Stepping of Cytoplasmic Dynein. *Cell*, 131(5):952–965, nov 2007.
- [122] Vaishnavi Ananthanarayanan, Martin Schattat, Sven K. Vogel, Alexander Krull, Nenad Pavin, and Iva M. Tolić-Nørrelykke. Dynein Motion Switches from Diffusive to Directed upon Cortical Anchoring. *Cell*, 153(7):1526–1536, jun 2013.
- [123] J.-H. Tsai and Bruce D. McKee. Homologous pairing and the role of pairing centers in meiosis. *J. Cell Sci.*, 124(12):1955–1963, jun 2011.
- [124] C D Meyer. *Matrix Analysis and Applied Linear Algebra*. Matrix Analysis and Applied Linear Algebra. Society for Industrial and Applied Mathematics, 2000.
- [125] B. Derrida. An exactly soluble non-equilibrium system: The asymmetric simple exclusion process. *Phys. Rep.*, 301(1-3):65–83, 1998.
- [126] Kirone Mallick. Some exact results for the exclusion process. *J. Stat. Mech. Theor. Exp.*, 2011:P01024, 2011.
- [127] Frank Spitzer. Interaction of Markov processes. *Adv. Math. (N. Y.)*, 5(2):246–290, oct 1970.
- [128] E P Hsu and S R S Varadhan. *Probability Theory and Applications*. IAS/Park City mathematics series. American Mathematical Soc., 1999.
- [129] A Schadschneider, D Chowdhury, and K Nishinari. *Stochastic Transport in Complex Systems: From Molecules to Vehicles*. Elsevier Science, 2010.

- [130] Murray T. Batchelor. The Bethe ansatz after 75 years. *Phys. Today*, 60(1):36–40, 2007.
- [131] David G. Levitt. Dynamics of a Single-File Pore: Non-Fickian Behavior. *Phys. Rev. A*, 8(6):3050–3054, dec 1973.
- [132] E. Barkai and R. Silbey. Diffusion of tagged particle in an exclusion process. *Phys. Rev. E*, 81(4):041129, apr 2010.
- [133] N Crampe, E Ragoucy, and M Vanicat. Integrable approach to simple exclusion processes with boundaries. Review and progress. *J. Stat. Mech. Theory Exp.*, 2014(11):P11032, 2014.
- [134] Joachim Krug. Boundary-induced phase transitions in driven diffusive systems. *Phys. Rev. Lett.*, 67(14):1882–1885, sep 1991.
- [135] S. Sandow and G Schütz. On U q [SU (2)]-Symmetric Driven Diffusion. *Europhys. Lett.*, 26(1):7–12, apr 1994.
- [136] Jan de Gier and Fabian H. L. Essler. Bethe Ansatz Solution of the Asymmetric Exclusion Process with Open Boundaries. *Phys. Rev. Lett.*, 95(24):240601, dec 2005.
- [137] Tomohiro Sasamoto and Herbert Spohn. One-Dimensional Kardar-Parisi-Zhang Equation: An Exact Solution and its Universality. *Phys. Rev. Lett.*, 104(23):230602, jun 2010.
- [138] H. Bethe. Zur Theorie der Metalle. *Zeitschrift für Phys.*, 71(3-4):205–226, mar 1931.
- [139] Elliott H Lieb. Exact Analysis of an Interacting Bose Gas. II. The Excitation Spectrum. *Phys. Rev.*, 130(4):1616–1624, may 1963.
- [140] Elliott H Lieb and Werner Liniger. Exact Analysis of an Interacting Bose Gas. I. The General Solution and the Ground State. *Phys. Rev.*, 130(4):1605–1616, may 1963.
- [141] C. N. Yang. Some Exact Results for the Many-Body Problem in one Dimension with Repulsive Delta-Function Interaction. *Phys. Rev. Lett.*, 19(23):1312–1315, dec 1967.
- [142] Rodney J Baxter. Partition function of the Eight-Vertex lattice model. *Ann. Phys. (N. Y.)*, 70(1):193–228, mar 1972.
- [143] Thomas M. Liggett. *Stochastic Interacting Systems: Contact, Voter and Exclusion Processes*, volume 324 of *Grundlehren der mathematischen Wissenschaften*. Springer Berlin Heidelberg, Berlin, Heidelberg, 1999.
- [144] G.M. Schütz. Exactly Solvable Models for Many-Body Systems Far from Equilibrium. In *Phase Transitions Crit. Phenom.*, volume 19, pages 1–251. Academic Press, 2001.
- [145] Olivier Golinelli and Kirone Mallick. The asymmetric simple exclusion process: an integrable model for non-equilibrium statistical mechanics. *J. Phys. A. Math. Gen.*, 39(41):12679–12705, oct 2006.